Large scale structure and dark energy

Ph.D Thesis in Physics
Universitat de Barcelona
Departament d'Astronomia i Meteorologia

(Programa de doctorat bienni 2003-2005)

Anna Cabré Albós
Supervisor: Enrique Gaztañaga Balbás

Tutor: Eduard Salvador Solé

Barcelona 2008

Part II

Redshift space distortions

Chapter 8

Theory of redshift space distortions

In this part of the thesis we present a different approach to measure the evolution in the growth of structure, based on redshift distortions. Galaxies, that trace the matter density in the universe, move differently depending on the cosmology. These peculiar velocities are added to the Hubble flow and this affects the distance that we obtain from redshifts in the direction of line-of-sight. The 2-point correlation function becomes anisotropic in redshift space, and gives us important information depending on the degree of anisotropy. We work with luminous red galaxies from the Sloan Digital Sky Survey, which occupy a big volume and are assumed to live in the centers of the halos. While in the previous part of this Thesis we use the photometric sample of SDSS (with angular positions) here we will focus in the spectroscopic sample, which contains information from peculiar velocities. In this chapter, we study the theory involved in our calculations.

8.1 Introduction to redshift space distortions

Peculiar velocities v are defined as deviations away from the Hubble flow due to local inhomogeneities:

$$\dot{r} = a\dot{x} = \dot{a}x + a\dot{x} = Hr + v \tag{8.1}$$

where a is the scale factor, $r = ax$ is the proper distance and x is the comoving distance.

The peculiar velocities of galaxies cause them to appear displaced along the line-of-sight in redshift space, since redshift is a measure of velocity as well as of distance. Then, the redshift distance s of a galaxy differs from the true distance r by its peculiar velocity along the line-of-sight. These displacements lead to redshift distortions, with two important contributions. The first, from large over densities that lead to a coherent bulk motion. We see walls denser and voids bigger and emptier, with a squashing effect in the 2-point redshift correlation function along the line-of-sight (Kaiser 1987). At small scales, random velocities inside clusters of galaxies produce a radial stretching pointed at the observer, known as fingers of God (FOG).

Although such distortions complicate the interpretation of redshift maps as positional maps, they have the advantage of bearing information about the dynamics of galaxies. In particular, the amplitude of distortions on large scales yields a measure of the linear redshift distortion parameter β, which is related to the cosmological matter density.

Kaiser (1987) pointed out that, in the large-scale linear regime, and in the plane-parallel approximation (where galaxies are taken to be sufficiently far away from the observer that the displacements induced by peculiar velocities are effectively parallel), the distortion caused by coherent infall velocities takes a particularly simple form in Fourier space:

$$P_s(k) = (1 + \beta\mu_k^2)^2 P(k). \tag{8.2}$$

where $P(k)$ is the power spectrum of density fluctuations δ defined in Eq.(2.11), μ is the cosine of the angle between k and the line-of-sight, the subscript s indicates redshift space, and β is the growth rate of growing modes in linear theory, the dimensionless quantity which solves the linearized continuity equation $\vec{\nabla}.\vec{v} + \beta\delta = 0$ in units where the Hubble constant is one. If the galaxy overdensity δ is linearly biased by a factor b relative to the underlying matter density δ_m of the Universe, $\delta = b\delta_m$ (see Eq.(2.14)), but velocities are unbiased, then the observed value of β is

$$\beta \approx \frac{\Omega^{0.55}}{b} \tag{8.3}$$

for standard gravity. See Hamilton (1992) for an extensive review.

8.2 Model for the anisotropic 2-point correlation function in redshift space

The 2-point correlation function, $\xi(\vec{r})$, is defined by the joint probability that two galaxies are found in the two volume elements dV_1 and dV_2 placed at separation $\vec{r}$ (see Peebles 1980)

$$dP_{12} = n^2[1 + \xi(r)]dV_1 dV_2 \tag{8.4}$$

We can split the distance $\vec{r}$ into its component along the line-of-sight (LOS) π and perpendicular to the LOS, σ, as shown in Fig.10.6, so that $\xi(\vec{r})$ is in fact a function $\xi(\pi, \sigma)$. These are the right variables to study redshift space distortions. In real space we usually have isotropy so that $\xi(\sigma, \pi) = \xi(r)$ with $r = \sqrt{\sigma^2 + \pi^2}$.

The correlation $\xi(\vec{r})$ in real space is related to the power spectrum by a Fourier transform:

$$\xi(\vec{r}) = \int P(k) e^{-i\vec{k}\vec{r}} \frac{d^3k}{(2\pi)^3} \tag{8.5}$$

and with isotropy,

$$\xi(r) = 4\pi \int_0^\infty P(k) \frac{sin(kr)}{kr} \frac{k^2 dk}{(2\pi)^3} \tag{8.6}$$

As mentioned above, Kaiser (1987) pointed out that the coherent infall velocities take a simple form in Fourier space given by Eq.(8.2). Hamilton (1992) translated these results into real space,

$$\xi'(\sigma, \pi) = [1 + \beta(\partial/\partial z)^2(\nabla^2)^{-1}]^2 \xi(r), \tag{8.7}$$

which reduces to

$$\xi'(\sigma, \pi) = \xi_0(s)P_0(\mu) + \xi_2(s)P_2(\mu) + \xi_4(s)P_4(\mu), \tag{8.8}$$

where in general (see also Eq.(8.16)),

$$\xi_0(s) = \left(1 + \frac{2\beta}{3} + \frac{\beta^2}{5}\right) \xi(r), \tag{8.9}$$

$$\xi_2(s) = \left(\frac{4\beta}{3} + \frac{4\beta^2}{7}\right) [\xi(r) - \overline{\xi}(r)], \tag{8.10}$$

$$\xi_4(s) = \frac{8\beta^2}{35} \left[\xi(r) + \frac{5}{2}\overline{\xi}(r) - \frac{7}{2}\overline{\overline{\xi}}(r)\right], \tag{8.11}$$

and

$$\overline{\xi}(r) = \frac{3}{r^3}\int_0^r \xi(r')r'^2 dr', \tag{8.12}$$

$$\overline{\overline{\xi}}(r) = \frac{5}{r^5}\int_0^r \xi(r')r'^4 dr'. \tag{8.13}$$

We use these relations to create a model $\xi'(\sigma,\pi)$ which we then convolve with the distribution function of random pairwise motions, $f(v)$, to give the final model $\xi(\sigma,\pi)$ (Peebles 1980):

$$\xi(\sigma,\pi) = \int_{-\infty}^{\infty} \xi'(\sigma,\pi - v/H(z)/a(z))f(v)dv \tag{8.14}$$

where we divide peculiar velocities by $a(z)$ to translate to comoving distances, since velocities are defined in physical coordinates.

We represent the random motions by an exponential form,

$$f(v) = \frac{1}{\sigma_v\sqrt{2}}\exp\left(-\frac{\sqrt{2}|v|}{\sigma_v}\right) \tag{8.15}$$

where σ_v is the pairwise peculiar velocity dispersion. An exponential form for the random motions has been found to fit the observed data better than other functional forms (Ratcliffe et al. 1998; Landy 2002).

Sometimes there is a confusion in the dispersion of the pairwise velocity distribution, which in the case of coming entirely from random peculiar velocities, should follow $\sigma_v^{1D} = \frac{1}{\sqrt{3}}\sigma_v^{3D}$, defined using the absolute values of the pairwise velocities. But in this work, σ_v refers to the dispersion taking into account the sign of the pairwise velocity in the LOS, being negative when galaxies are approaching each other and positive when they are moving further away. We can only do this distinction in one dimension. This dispersion σ_v used here is larger than the 1 dimensional σ_v^{1D}.

When we add non-linear bias to the real-space correlation function, the corresponding $\xi(\pi,\sigma)$ is altered at different distances, not only for small redshift scales, basically around the zone FOG.

Matsubara (2004) and Scoccimarro (2004) have presented different models for the 2-point correlation function in redshift space. Tinker et al. (2006) and Tinker (2007) do a modeling of redshift space distortions in the context of halo occupation distribution model (HOD). These models are complementary to the one studied here. In most situations the differences are small and we will show that our modeling gives good agreement with simulations and real data.

8.3 Multipoles of $\xi(\pi,\sigma)$

We can define the multipoles of $\xi(\pi,\sigma)$ as

$$\xi_\ell(s) = \frac{2\ell+1}{2}\int_{-1}^{+1} \xi(\pi,\sigma)P_\ell(\mu)d\mu. \tag{8.16}$$

where μ is cosine of the angle to the line-of-sight π.

The normalized quadrupole (Hamilton 1992) is defined as

$$Q(s) = \frac{\xi_2(s)}{\xi_0(s) - (3/s^2)\int_0^s \xi_0(s')s'^2 ds'} \tag{8.17}$$

Linear bias cancels in the quadrupole, and $Q(s)$ is slightly dependent on the shape of the correlation function, such as changes of Ω_m in large scales or scale dependent non-linear bias for small scales.

In the Kaiser approximation, large scales, the quadrupole is directly related to β

$$Q(s) = \frac{\frac{4}{3}\beta + \frac{4}{7}\beta^2}{1 + \frac{2}{3}\beta + \frac{1}{5}\beta^2} \tag{8.18}$$

In small scales, the quadrupole depends strongly on the random pairwise velocities, represented by σ_v, but it does not depend much on non-linear bias, as we will show.

8.4 The projected correlation function $\Xi(\sigma)$

As we will show, the redshift-space correlation function differs significantly from the real-space correlation function because of the distortions originated in the direction LOS. We can estimate the real-space correlation function by calculating the projected correlation function, $\Xi(\sigma)$, integrating the redshift distorted $\xi(\pi, \sigma)$ along the line-of-sight π.

$$\Xi(\sigma) = 2\int_0^\infty \xi(\sigma, \pi)\ d\pi \tag{8.19}$$

However, with data, we can not integrate until infinite. We set the upper limit in this integral to $\pi_{\max} = 80 Mpc/h$. The result does not change when we move the upper limit of the integral for $\pi_{\max} > 60 Mpc/h$ in the data.

Davis & Peebles (1983) show that $\Xi(\sigma)$ is directly related to the real-space correlation function.

$$\Xi(\sigma) = 2\int_\sigma^\infty \frac{r\xi(r)dr}{(r^2 - \sigma^2)^{\frac{1}{2}}}. \tag{8.20}$$

If we assume that the real space correlation function is a power law $\xi(r) = (r/r_0)^{-\gamma_0}$, then we can do this integral numerically, obtaining:

$$\frac{\Xi(\sigma)}{\sigma} = \left(\frac{r_0}{\sigma}\right)^{\gamma_0} \frac{\Gamma(\frac{1}{2})\Gamma(\frac{\gamma_0 - 1}{2})}{\Gamma(\frac{\gamma_0}{2})} = \left(\frac{r_0}{\sigma}\right)^{\gamma_0} A(\gamma_0). \tag{8.21}$$

The parameters γ_0 and r_0 can then be estimated from the measured $\Xi(\sigma)$, giving a value of the real-space clustering independent of any peculiar motions (see also, Fry & Gaztanaga 1994).

8.5 The real space correlation function $\xi(r)$

It is possible to estimate $\xi(r)$ by directly inverting $\Xi(\sigma)$ (Saunders et al. 1992). They recast Eq.(8.20) into the form,

$$\xi(r) = -\frac{1}{\pi}\int_r^\infty \frac{(d\Xi(\sigma)/d\sigma)}{(\sigma^2 - r^2)^{\frac{1}{2}}} d\sigma. \tag{8.22}$$

Assuming a step function for $\Xi(\sigma) = \Xi_i$ in bins centered on σ_i, and interpolating between values,

$$\xi(\sigma_i) = -\frac{1}{\pi} \sum_{j \geq i} \frac{\Xi_{j+1} - \Xi_j}{\sigma_{j+1} - \sigma_j} \ln \left(\frac{\sigma_{j+1} + \sqrt{\sigma_{j+1}^2 - \sigma_i^2}}{\sigma_j + \sqrt{\sigma_j^2 - \sigma_i^2}} \right) \tag{8.23}$$

for $r = \sigma_i$.

We take the redshift space anisotropic model $\xi(\pi, \sigma)$ in Eq.(8.14), with a fixed $\beta = 0.35$ and $\sigma_v = 400 km/s$, and we use Eq.(8.19) to obtain the projected correlation function $\Xi(\sigma)$ as if it was data. We fix the upper limit in the integral: 60Mpc/h, 80Mpc/h, 100Mpc/h and 200Mpc/h (dotted lines in top panel of Fig.8.1), and compare the result to the one obtained theoretically from Eq.(8.20) (solid line in top panel of Fig.8.1). As we increase the upper limit in the integral, we approach the real result, but we can not integrate until 200Mpc/h in real data, because as we will see in future sections, data is quite noisy for $\pi > 60 Mpc/h$. The conclusion is that we will not be able to recover the projected correlation function completely free of redshift distortions for large scales in real data (at least with available data), just where we would like to evaluate the shape of the real correlation function, but we can use it at small scales.

In the bottom panel of Fig.8.1 we see the real space correlation function recovered from the previously calculated projected correlation function with different upper limit fixed, Eq.(8.22). We obtain a good estimation of the $\xi(r)$ until 30Mpc/h, we will use this inversion to see the non-linear bias at small scales.

This analysis can be done for different values of β and σ_v and we find very similar conclusions. We have shown in the plots the values that are in concordance with real LRG SDSS data.

Once we recover the real-space correlation function, we can also estimate the ratio of the redshift-space correlation function, $\xi(s)$, to the real-space correlation function, $\xi(r)$, which gives an estimate of the redshift distortion parameter, β, on large scales:

$$\frac{\xi(s)}{\xi(r)} = 1 + \frac{2\beta}{3} + \frac{\beta^2}{5}. \tag{8.24}$$

As we have shown in Fig.(8.1), $\xi(r)$ will be in general slightly overestimated at large scales when we estimate it from the projected correlation function $\Xi(\sigma)$, so the expression $\frac{\xi(s)}{\xi(r)}$ will in general be slightly lower than expected on large scales.

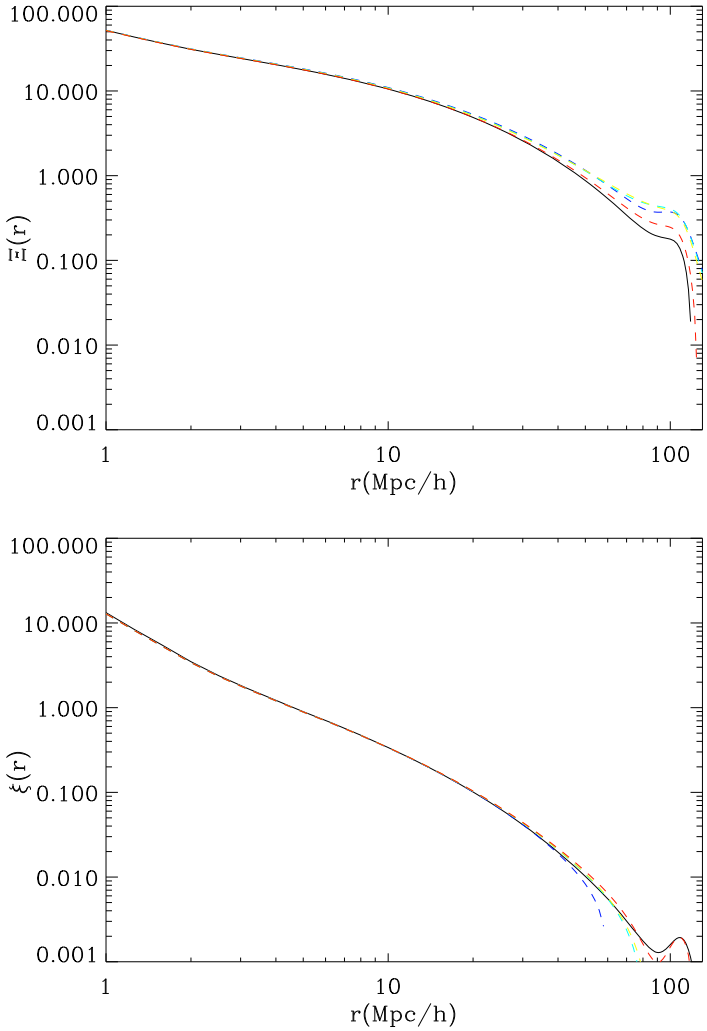

Figure 8.1: Top: We compare here the projected perpendicular correlation function calculated theoretically from $\xi(r)$ (solid line) compared to integral of $\pi - \sigma$ to rf=60.(cyan), 80.(blue), 100.(yellow), 200.(red) for $\beta = 0.35$ and $\sigma_v = 400 km/s$. Bottom: Estimation of the real space correlation function by deprojecting the dotted color lines $\Xi(r)$ in the top panel

8.6 Growth history

According to general relativity, the equations that determine the evolution of the density contrast δ in a flat background consisting of matter with density ρ_m and dark energy with $\rho_{DE} = \frac{p_{DE}}{w}$ are of the form

$$\ddot{\delta} + 2\frac{\dot{a}}{a}\dot{\delta} = 4\pi G\rho_m\delta \tag{8.25}$$

$$\left(\frac{\dot{a}}{a}\right)^2 = \frac{8\pi G}{3}\left(\rho_m + \rho_{DE}\right) \tag{8.26}$$

$$2\frac{\ddot{a}}{a} + \left(\frac{\dot{a}}{a}\right)^2 = -8\pi G w\rho_{DE} \tag{8.27}$$

where $\Omega_m(a)$ is the matter density at a redshift z where $a = 1/(1+z)$

$$\Omega_m(a) = \frac{H_0^2\Omega_{0m}a^{-3}}{H^2(a)} \tag{8.28}$$

and

$$H(a) = H_0\sqrt{\Omega_{0m}a^{-3} + (1-\Omega_{0m})a^{-3(1+w)}} \tag{8.29}$$

so the linear theory growth $D(a) = \delta/\delta(0)$ factor depends purely on the expansion history $H(a)$, $w(a)$, $\Omega_m(a)$. Any discrepancy found between the observed growth and the predicted based on expansion history test the gravity.

Considering the gravitational growth index formalism of Linder (2005),

$$f = \frac{d\ ln\ D}{d\ ln\ a} = \Omega_m(a)^\gamma \tag{8.30}$$

where γ is the gravitational growth index. Note that, as it was designed for, the growth index formalism separates out the two physical effects on the growth of structure and the redshift distortion: $\Omega(a)$ involves the expansion history and γ focuses on the gravity theory.

$$D(a) = e^{\int_0^a d\ln a\,[\Omega(a)^\gamma - 1]}. \tag{8.31}$$

$$\gamma = \frac{3(w_0 - 1)}{6w_0 - 5} \tag{8.32}$$

which reduces to $\gamma = 6/11 = 0.55$ for ΛCDM ($w = -1$), and it is accurate to less than 0.1%.

Zhang et al. (2007) propose a test to discriminate gravity at cosmological scales based on lensing. Nesseris & Perivolaropoulos (2008) have compiled a data set of various data points at a redshift range that can be used to constrain the linear perturbation growth rate f through redshift distortions or indirectly through the rms mass fluctuation $\sigma_8(z)$ inferred from $Ly-\alpha$. Wang (2007) do a prediction of the characteristics that a survey must accomplish to be able to rule out the DGP gravity model (an extra-dimensional modification of gravity), where the idea is to calculate H(z) from the baryon acoustic peak and f(z) from redshift distortions. Guzzo et al. (2008) test the nature of cosmic acceleration using galaxy redshift distortions at z=0.8, obtaining f, but errors are still too high to distinguish between different theories. Acquaviva et al. (2008) has recently done a new compilation of results. See Bertschinger & Zukin (2008) for a theoretical approach to modified gravity.

8.6.1 Growth history in redshift distortions

The redshift distortion parameter observed through the anisotropic pattern of galaxy redshifts on cluster scales is (Kaiser 1987)

$$\beta = \frac{1}{b}\frac{d\ln D}{d\ln a} = f/b, \tag{8.33}$$

where b is the bias between galaxies and the total matter, D is the linear theory growth factor at expansion scale factor a, and f is called growth rate of fluctuations.

See Linder (2007) for a detailed study of the impact of β to variations in the cosmological parameters. The gravitational growth index has substantial impact on the redshift distortion, with β more sensitive to the growth index γ and Ω_m than to the equation of state variables w_0, w_a, especially at low redshifts. (where the effective w(a) is parametrized as $w(a) = w_0 + w_a(1-a)$) This is furthermore where measurements can be made most precisely, so this suggests that redshift distortions offer a promising tool for investigating gravity.

In this work, we will use redshift distortions to see changes in modified gravity, assuming that w is slightly dependent on γ so that the observations are explained by exclusively the growth history, with the same expansion history.

8.6.2 Growth history in ISW effect

As seen in the first part of the thesis, the angular auto-correlation function is proportional to

$$w_{GG} \propto \sigma_8^2 \phi_G(z)^2 b(z)^2 D(z)^2 \tag{8.34}$$

and the cross-correlation between galaxies and CMB w_{TG} (ISW effect)

$$w_{TG} \propto \sigma_8^2 \phi_G(z) b(z) D(z) \frac{d[D(z)/a]}{dz} \tag{8.35}$$

where after some calculations

$$\frac{d[D(z)/a]}{dz} = D(z)(1-f) \tag{8.36}$$

We can learn about the growth rate of fluctuations f using the ISW effect. This method is independent to the one explained before with redshift distortions.

8.7 Baryon acoustic peak

Before the recombination, the universe was filled by a plasma with coupled photons and baryons. Sound speed was relativistic then, due to the pressure of photons, and the sound horizon had a comoving radius of 150Mpc. The cosmological fluctuations produced sound waves in this plasma, when the recombination occurred, 380,000 years after the Big Bang. Temperature dropped down to 3000 K and photons and baryons recombined to form neutral gas. At this stage of the evolution of the Universe, the sound speed dropped off abruptly and acoustic oscillations became frozen until now. The signature they imprinted can be found both in CMB and LSS, so the baryon acoustic peak can be used as a cosmic ruler.

The distance that a sound wave has traveled at the age of the universe at that time is the comoving length of the sound horizon, which depends on the speed of sound in the plasma,

related to the density of the fluid.

$$s(a) = \int_0^t \frac{c_s(t')}{a(t')} dt' = \int_0^a \frac{c_s(a')}{a'^2 H(a')} da' \tag{8.37}$$

where the sound of speed $c_s(s)$ is

$$c_s(s) = \frac{\partial p}{\partial \rho} = \frac{c^2}{3} \left(1 + \frac{3\rho_b}{4\rho_\gamma}\right)^{-1} \tag{8.38}$$

and $H(a)$ before at the epoch of recombination is

$$H(a) = H_0 \sqrt{\Omega_m (1+z)^3 + \Omega_r (1+z)^4} \tag{8.39}$$

In harmonic space, the baryonic feature is seen as a series of small-amplitude oscillations, while in the 2-point correlation function is seen as a single wide peak, around 100Mpc/h. We can use the position of the baryonic peak in the 2-point correlation function as a measure of H(z) and $D_A(z)$. If we measure the peak at the radial direction, we find directly information about $H(z)$, since $dr = dz/H(z)$. In principle, w can be estimated from both the radial and transverse parts of the power spectrum. Transforming redshifts to comoving distances requires the Hubble parameter $H(z)$ while transforming angular separations involves the angular-diameter distance $D_A(z)$. Both $H(z)$ and $D_A(z)$ depend on w as well as other cosmological parameters. Thus, the radial and tangential components provide independent routes to w. In real data, recent surveys use the averaged power spectrum or the monopole to do predictions, but in future surveys, the anisotropy of BAO in redshift space can be used to constrain better w and Ω_m.

The comoving sound horizon is calculated with WMAP5, $s(a) = 146.8 \pm 1.8 Mpc$. The idea is to compare the well known measure of the baryonic peak calculated by WMAP5, with the peak obtained from LSS using a fiducial cosmology.

A number of effects can alter the form of the two-point correlation function from the linear perturbation theory predictions presented in the last section: the non-linear growth of perturbations, redshift space distortions and bias.

It turns out that bias, general non-linear evolution and redshift-space distortions are much simpler to deal with in the case of the correlation function than they are for the power spectrum. On the scales we consider ($60 < (rMpc/h) < 180$), these effects primarily result in a change in the amplitude of the measured correlation function and do not alter its shape (Sanchez et al. 2008).

See Blake & Glazebrook (2003), Eisenstein et al. (2007b), Eisenstein et al. (2007a), Smith et al. (2008), Crocce & Scoccimarro (2008) and Sanchez et al. (2008) for discussion about all these effects on the BAO peak in the 2-point correlation function, and Eisenstein et al. (2005b), Percival et al. (2007a) and Percival et al. (2007b) for examples of estimation of cosmological parameters using BAO's.

8.8 Magnification bias in the baryon acoustic peak

Magnification bias is given by the lensing effect caused by the dark matter which is located between the observed galaxies and us (in the line-of-sight). This lensing creates an enhance of

number of galaxies per pixel due to the magnification that allows us to see dimmer galaxies, and a suppression of the number of galaxies due to the growth of the area, which excludes some galaxies. The final net lensing is controlled by the slope in the number counts. (see Hui et al. 2007)

The slope s is defined as

$$s = \frac{d \log_{10} N(< m)}{dm} \tag{8.40}$$

where $N(< m)$ refers to the number of galaxies in the survey with apparent magnitude $< m$

Magnification can be important in the direction LOS, and particularly at large scales, where it is located the baryon acoustic peak, so we will calculate the slope and see the effects in our real LRG data. When noise is shot-noise dominated, as in the case of galaxies LRG in the direction LOS, bias increases only the signal (not the noise), so we can gain S/N easily.

The 2-point correlation function, with redshift distortions and the new terms due to magnification, is:

$$\xi_{obs} = \xi_{gg} + \xi_{gv} + \xi_{vg} + \xi_{vv} + \xi_{g\mu} + \xi_{\mu g} + \xi_{\mu\mu} \tag{8.41}$$

where the cross-terms velocity-magnification vanish due to Limber approximation. The first four terms are due to redshift distortions and they are explained in §8.2. The cross-term μg is the only one that can alter significantly the signal at large scales. The auto-magnification term is too low compared to the cross-term, it can be more than 5 orders of magnitude lower. The cross-term galaxy-magnification is:

$$\begin{aligned} \xi_{g\mu}(\chi_1, \boldsymbol{\theta}_1; \chi_2, \boldsymbol{\theta}_2) = \frac{3}{2} H_0^2 \Omega_m (5s - 2) \\ (1 + z_1) \frac{(\chi_2 - \chi_1)\chi_1}{\chi_2} \Theta(\chi_1 < \chi_2) \\ \int \frac{d^2 k_\perp}{(2\pi)^2} P_{gm}(z_1, k_\perp) e^{i \mathbf{k}_\perp \cdot \chi_1 (\boldsymbol{\theta}_1 - \boldsymbol{\theta}_2)} \end{aligned} \tag{8.42}$$

where $\Theta(\chi_1 < \chi_2)$ is a step function which equals 1 if $\chi_1 < \chi_2$ and vanishes otherwise, H_0 is the Hubble constant today, Ω_m is the matter density today (normalized by the critical density), z_1 is the redshift corresponding to the comoving distance χ_1, and P_{gm} is the (3D) galaxy-mass power spectrum, and $\mathbf{k}_\perp$ is the transverse Fourier wave vector. We have used the Poisson equation to relate the gravitational potential ϕ to the mass overdensity δ:

$$\nabla^2 \phi = 3 H_0^2 \Omega_m (1 + z) \delta / 2 \tag{8.43}$$

Note that the speed of light is set to 1 throughout.

Further, suppose one has a galaxy survey, or a subsample thereof, that spans some finite redshift range such that the radial separation $\chi_1 - \chi_2$ is always small compared to χ_1 or χ_2. This is a sensible assumption since at sufficiently large separations, galaxy evolution becomes important and complicates one's analysis. Let $\bar{\chi}$ be the mean radial comoving distance to these galaxies, and $\bar{z}$ be the associated mean redshift. The galaxy-magnification cross-correlation

and the magnification auto-correlation can be simplified as follows:

$$\xi_{g\mu}(\chi_1, \boldsymbol{\theta}_1; \chi_2, \boldsymbol{\theta}_2) + \xi_{g\mu}(\chi_2, \boldsymbol{\theta}_2; \chi_1, \boldsymbol{\theta}_1) = \frac{3}{2} H_0^2 \Omega_m (5s - 2)(1 + \bar{z}) |\chi_2 - \chi_1| \int \frac{d^2 k_\perp}{(2\pi)^2} P_{gm}(\bar{z}, k_\perp) e^{i \mathbf{k}_\perp \cdot \bar{\chi} (\boldsymbol{\theta}_1 - \boldsymbol{\theta}_2)} \tag{8.44}$$

We can use this simplified model to have an idea of the magnification we will have in LRG. These galaxies are far, at redshift=0.35, so we can consider that the distance to the survey is big compared to the distances between galaxies inside the survey. The galaxy-magnification term is important at the LOS direction and vanish quickly when moving to bigger angles to the LOS. Moreover, it is proportional to the LOS distance between galaxies, the reason why we can see the magnification only at large scales, where there is the BAO peak. No linear bias can increase considerably the magnification.

See Matsubara (2000b), Hui et al. (2007) and Hui et al. (2008) for a more detailed account.

Chapter 9

Testing the errors and models with simulations

In this chapter we perform an analysis of simulations in order to test the models used and the errors. We can see through the simulations how to use the analytical models to extract cosmological information optimally. We also study the pairwise velocities in both real and redshift space. Finally we calculate Monte Carlo errors, we compare them with jackknife errors and we obtain an analytical form for the error in $\xi(\pi, \sigma)$ when the density of objects is low, as in the LRG case.

9.1 Description of the simulations

We have used a comoving output at redshift 0.3 of a MICE simulation, run in the super computer Mare Nostrum in Barcelona by MICE consortium (www.ice.cat/mice)

The simulation contains 2048^3 dark matter particles, in a cube of side 7689Mpc/h, $\Omega_M = 0.25$, $\Omega_b = 0.044$, $\sigma_8 = 0.8$, $n_s = 0.95$ and $h = 0.7$.

We have divided this big cube in 3^3 cubes of side 2 x 1275Mpc/h, and taking the center of these secondary cubes as the observation point (as if we were at z=0), we apply the selection function of LRG, which arrives until z=0.47 (r=1275Mpc/h). We can obtain 8 octanes from the secondary sphere included in the cube, so at the end we have 8 mock LRG catalogs from each secondary cube, which have the same density per pixel as LRG in order to have the same level of shot noise, and the area is slightly smaller (LRG occupies 1/7 of the sky with a different shape). The final number of M independent mock catalogs is 216 (27x8).

There is no bias in these simulations, because there is only dark matter, so $\beta = \frac{\Omega_m(z)^{0.55}}{b} = 0.62$ (where $\Omega_m(z) = \Omega_m(1+z)^3/(\Omega_m(1+z)^3 + 1 - \Omega_m)$ and bias=1)

We have also used a MICE simulation with 2048^3 dark matter particles, in a cube of side 3072Mpc/h, at z=0 to study pairwise velocities in dark matter particles and halos.

9.1.1 How to generate redshift distortions in the simulations

Redshift distortions are generated in the line-of-sight direction, where the expansion of the universe (intrinsic redshift) and peculiar velocities can not be separated, and we take the sum

as if it was all due to the expansion, an indicator of the distance to the galaxy. Then the distance in redshift space s is:

$$s = r + v_{LOS}/H(z)/a(z) \tag{9.1}$$

where we divide by a(z) because we work in comoving distances.

9.2 Halo simulations

We have also used 50 low resolution halo simulations from the Institute for Computational Cosmology in Durham, labeled L-BASICC (see Angulo et al. 2008). Here, the cosmological parameters are: $\Omega_M = 0.25$, $\Omega_b = 0.045$, $\sigma_8 = 0.9$, $n_s = 1$ and $h = 0.73$. We use these simulations to test the errors in the case of high bias ($\backsim 2$), but they have low resolution and 50 is a reduced number to study errors. The simulations are comoving outputs at a z=0, of side 1340Mpc/h and 448^3 particles. The halos contain 10 or more particles (corresponding to a mass of 1.8 $10^{13} h^{-1} M_{\odot}$).

9.3 Description of errors Monte Carlo, jackknife and analytical

The description of the different approaches to errors is explained in detail in the first part of the thesis. Here we do a brief summary. We obtain the Monte Carlo error from the dispersion of M independent realizations of our universe. Typically, we need 100 independent simulations for the diagonal error, and more for the covariance matrix, depending on the case. The Monte Carlo is considered the true error, but it spends more computational time than other kinds of errors, and it also requires simulations with the same particularities of the data analyzed.

For M realizations, the Monte Carlo covariance is

$$C_{ij} = \frac{1}{M} \sum_{k=1}^{M} (\xi(i)^k - \widehat{\xi}(i))(\xi(j)^k - \widehat{\xi}(j)) \tag{9.2}$$

where $\xi(i)^k$ is the measure in the k-th simulation (k=1,...M) and $\widehat{\xi}(i)$ is the mean over M realizations. The case i=j gives the diagonal error (variance).

For the jackknife error, we obtain the different realizations that we need to compute the error from the data, dividing the catalog in M zones, and we consider that each simulation is all the catalog except from one of these JK zones. In this case, as the realizations are clearly not independent, we correct for a factor $(M-1)$ the previous covariance to account for this effect.

We use the dark matter simulations to probe the limit in JK errors, which we want to use in LRG data, because we do not have precise simulations of LRG galaxies to obtain reliable Monte Carlo errors. We study the errors in the redshift space correlation function $\xi(\pi, \sigma)$, the monopole $\xi(s)$, the quadrupole $Q(s)$, the perpendicular projected function $\Xi(r)$, and finally the obtained real-space correlation function $\xi(r)$.

In the $\xi(\pi, \sigma)$ case, we use different binning in the data to obtain the 2 dimensional $\pi - \sigma$ information, squares of 5Mpc/h, 1Mpc/h or 0.2Mpc/h. The errors JK and MC seem to agree

at small scales until $\sigma = 20Mpc/h$ but we see that there is a well motivated phenomenological form that match perfectly the MC errors at even large scales. This analytical error is proportional to a noise part, as $1/\sqrt{number\ of\ pairs}$ and a part proportional to the signal. It works well in this case because LRG is a low density catalog, and we are able to separate both parts, as if we were in a diagonal space. In general, the analytical derivation of the error is more complicated. The idea is to fit the phenomenological form to the MC errors and from there we can use the formula as an estimation of the error in LRG.

The error has the following form, when we add the noise and signal parts linearly (it fits better than quadratically)

$$err(\xi) = err(\xi)_{noise} + err(\xi)_{signal} = err(\xi)_{noise} + \xi/r_{fit} \tag{9.3}$$

We can associate r_{fit} to the number of independent nodes in the catalog.

The correlation function is calculated as

$$\xi(\pi,\sigma) = \frac{DD}{RR} - 2\frac{DR}{RR} + 1. \tag{9.4}$$

The error that comes from having a limited number of pairs is, for data-data: $err(DD) = 1/\sqrt{RR/N_R^2}$, and for DR: $err(DR) = 2/\sqrt{RR/N_R}$. We suppose that the error in random-random is insignificant, because we are using a denser random catalog. We add the errors quadratically

$$err(\xi)_{noise} = \sqrt{\frac{N_R^2 + 4N_R}{RR}} \tag{9.5}$$

where the random catalog is N_R denser than the data catalog. We can reduce the error in $\xi(\pi,\sigma)$ by increasing the number of particles in the random catalog, modifying the error coming from DR, which is inversely proportional to the square root of the pairs data-random. The first part of the error is always the same, because it depends on the data.

For $N_R = 10$, as in the simulations, $err\xi_{noise} = \sqrt{140./RR}$, so the DR part is a 40% of the DD part. For $N_R = 20$, as in the LRG, $err\xi_{noise} = \sqrt{480./RR}$, so the DR part is now a 20% of the DD part.

We have tried to add the error due to the signal quadratically or linearly, and it fits better for the linear adjust. However, we want to use this approach at large σ, where the signal part is not significant. For small σ scales, JK and MC coincide so we can just use JK error in LRG.

For a binning of 5Mpc/h, $r_{fit} = 95$ and for 1Mpc/h, $r_{fit} = 25$.

We fit different parameters that we can extract from the $\xi(\pi,\sigma)$ in the simulations using MC errors or the analytical form and we obtain the same constraints. In the next section, we will see the differences between errors.

9.4 Study of the errors

In this section we see the differences between the different errors, and covariances.
First, we can see the octant catalog used for the mock divided in 63 jackknifes zones, with the same area and approximate shape; and the SDSS DR6 catalog divided in 73 jackknife zones (see Fig.9.1).

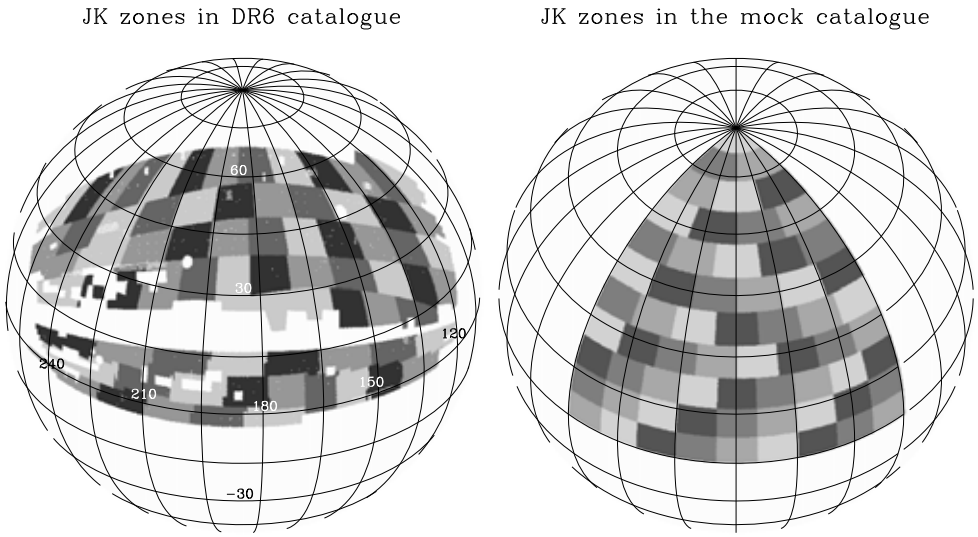

Figure 9.1: Left panel: JK zones for the LRG catalog (equatorial coordinates). Right panel: the mock catalog with its JK zones

9.4.1 Errors in $\xi(\pi, \sigma)$

In Fig.9.2 we show the differences in the diagonal error between MC, JK and the analytical form, when binning the correlation function with 5Mpc/h. MC error is calculated using MICE simulation and JK is the mean over all the JK that we have calculated in each mock. JK works well for small σ but it becomes higher than MC when going to large σ. The analytical form agrees at all scales with MC error. We have done the same analysis with the halo simulations from Durham, which have bias as LRG, and the conclusions are exactly the same, see Fig.9.3. After these plots from simulations, we see in Fig.9.4 and 9.5 the error JK obtained from the real LRG data using a random catalog 10 and 20 times denser than the data, and the analytical form. Again, the JK error is bigger than the analytical one, which is representative of the true error. Note the similarity between the errors in the data and in the simulations. If we use a random catalog 20 times denser, as we do for the analysis of the data, the error is clearly lower, as we see in Fig.9.5.

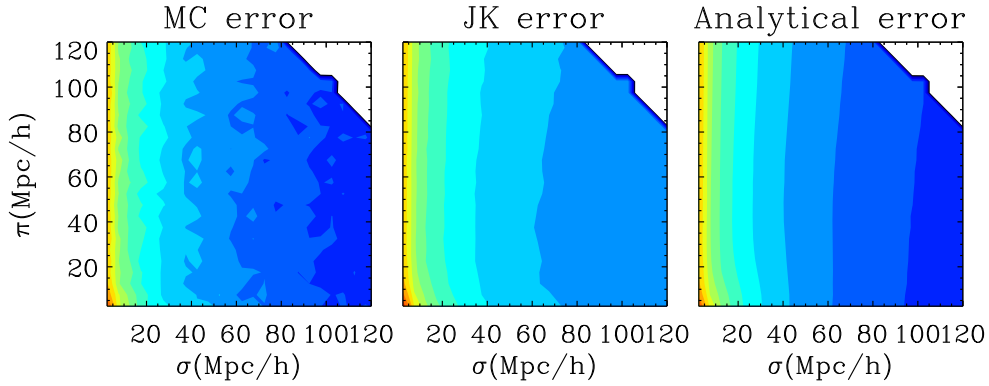

Figure 9.2: Diagonal error in $\xi(\pi, \sigma)$ in redshift space for MICE simulations and binning 5Mpc, with contours $\xi = 0.002 - 0.1$ (log increment=0.2)

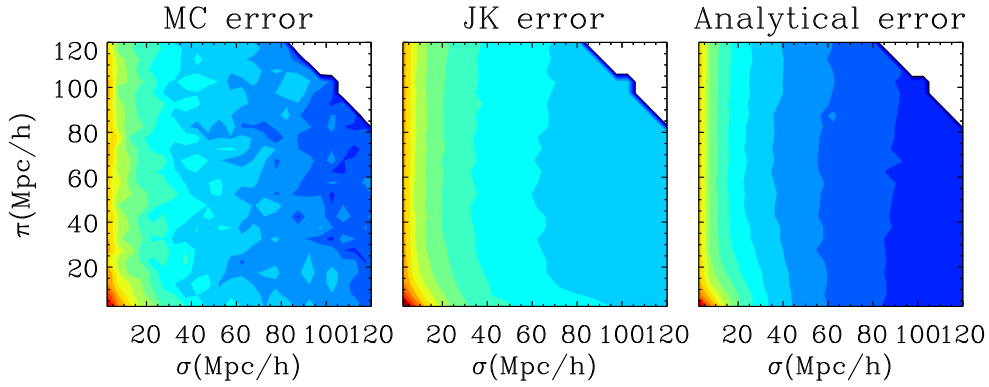

Figure 9.3: Diagonal error in $\xi(\pi, \sigma)$ in redshift space for Durham simulations (contours as Fig.9.2)

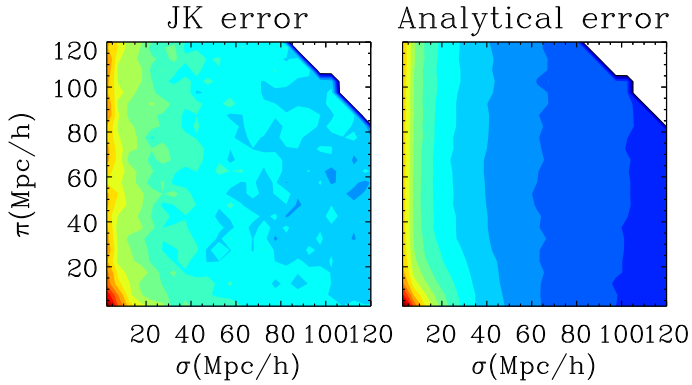

Figure 9.4: Diagonal error in $\xi(\pi, \sigma)$ in redshift space for LRG data and random catalog 10 times the data (contours as Fig.9.2)

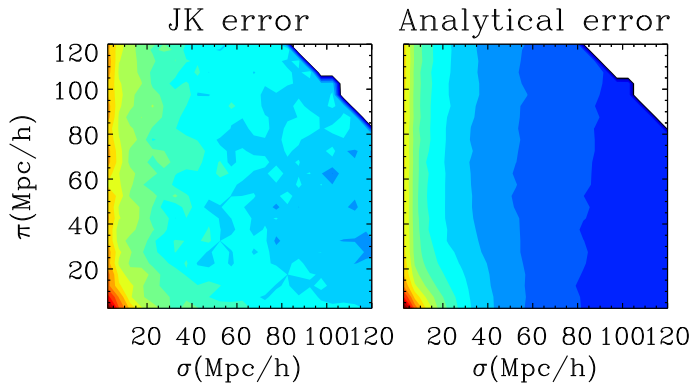

Figure 9.5: Diagonal error in $\xi(\pi, \sigma)$ in redshift space for LRG data and random catalog 20 times the data (contours as Fig.9.2). As we can see, error is reduced increasing the number of particles in the random catalog

We next show similar plots, but for a binning of 1Mpc/h, which we use on small scales (for r<40 Mpc/h). In this case there is no covariance between points, but the error increases, a way to compensate the lack of covariance. In Fig.9.6 we see the comparison between errors in MICE simulations, Fig.9.7 shows the same in Durham simulations with bias, where we see that JK works well at small π and σ, while the analytical form is optimal for the rest of scales. After that, a comparison between JK and the analytical form in LRG with random catalog 10 times denser (Fig.9.8), and 20 times denser (Fig.9.9). Finally, we see this comparison for a slice in redshift from z=0.15-0.34, where there are fewer particles, and consequently the error increases (Fig.9.10).

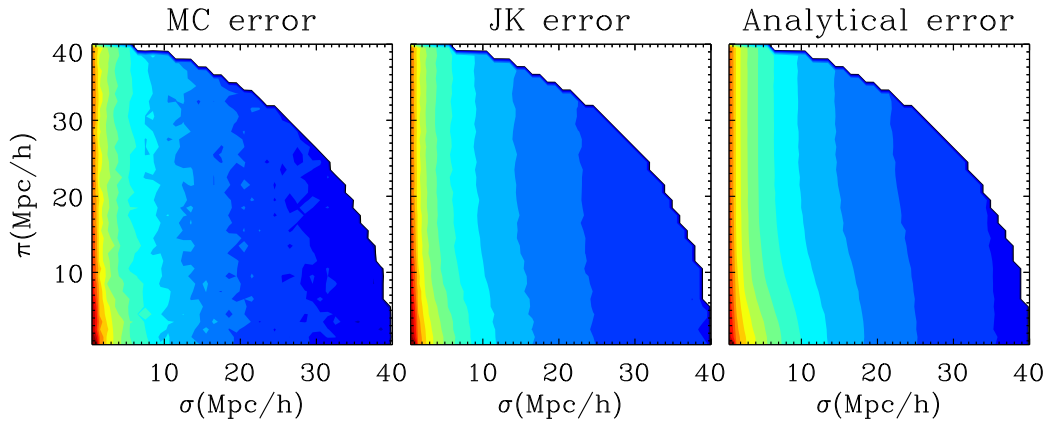

Figure 9.6: Diagonal error in $\xi(\pi, \sigma)$ in redshift space for MICE simulations and binning 1Mpc, with contours $\xi = 0.02 - 0.6$ (log increment=0.2). When decreasing the bin in our calculation, the error increases, but there is not covariance in this case.

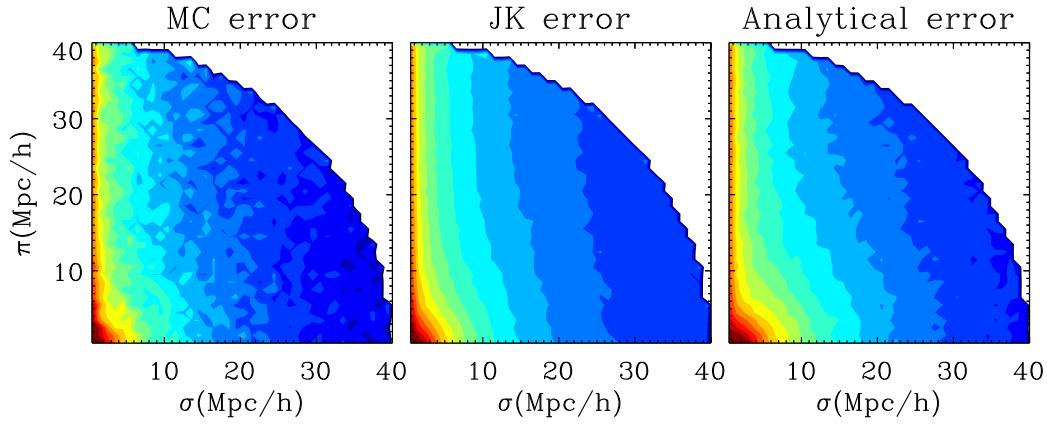

Figure 9.7: Diagonal error in $\xi(\pi, \sigma)$ in redshift space for Durham simulations (contours as Fig.9.6)

In the real LRG data, we use the JK error obtained from the same data for small scales σ, the analytical approach for large scales σ and π , and if needed (for the binning=5Mpc/h), the covariance from MICE simulations, which does not depend on the signal, but in the distance between points.

So far we have shown diagonal errors. The covariance is in fact small, this can be seen

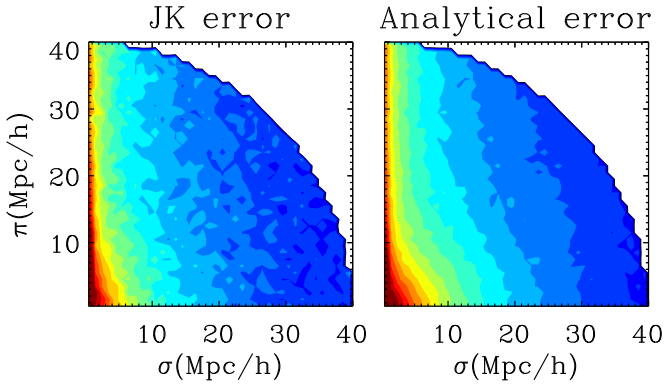

Figure 9.8: Diagonal error in $\xi(\pi, \sigma)$ in redshift space for LRG data and random catalog 10 times the data (contours as Fig.9.6)

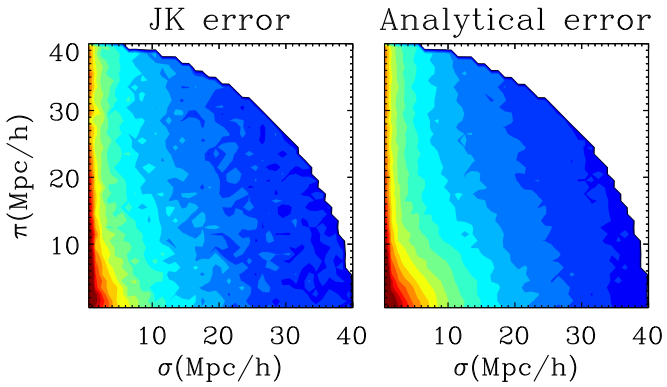

Figure 9.9: Diagonal error in $\xi(\pi, \sigma)$ in redshift space for LRG data and random catalog 20 times the data (contours as Fig.9.6). As we can see, error is reduced increasing the number of particles in the random catalog

in Figure 9.11 where we show the MC covariance. It has the same approximate shape and amplitude for all the points.

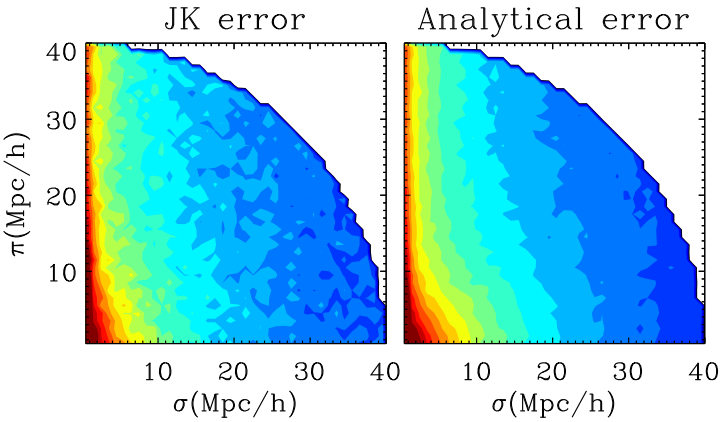

Figure 9.10: Diagonal error in $\xi(\pi, \sigma)$ in redshift space for LRG data from redshift 0.15 to 0.34 and random catalog 20 times the data (contours as Fig.9.6). The error is bigger than in the catalog of all LRG

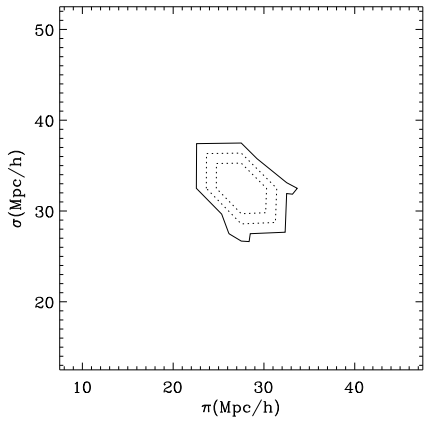

Figure 9.11: Covariance of $\xi(\pi, \sigma)$ at the position $\sigma = 30Mpc/h$, $\pi = 30Mpc/h$, with contours 0.1 (solid), 0.3 and 0.5

9.4.2 Error in the monopole $\xi_0(s)$

The error in the monopole is not easy to predict theoretically, but in this case JK error works well. We plot in the left panel of Fig.9.12 the monopole when we bin the data with a separation 5Mpc/h (black for the simulations, red for LRG data). At the right panel, we see the difference between the mean JK error and its dispersion (solid line with errors) and the MC error (dashed line), and over-plotted the JK error for the LRG (color). The covariance for the monopole is plotted in Fig.9.13, not completely smooth for the MC case, because we would need probably more than 216 simulations, but we see that it has the same shape than JK covariance, which we will use to fit our LRG data. JK covariance is smoother than the MC because we have taken the mean over 216 x 63 realizations (216 mocks x 63 JK zones), which seems enough to converge. The next two plots show the same comparison but with a bin of 1Mpc/h (Fig.9.14 and Fig.9.15). JK error also works in this case, and we see that the error is higher here than in the 5Mpc/h bin, while the covariance is smaller, practically equal to zero. As we can see, the error for LRG is larger than the one in simulations, since the signal is also higher due to bias. The distinction between blue and red line is the number of the particles in the random catalog (N_R), which does not change the estimation of the error.

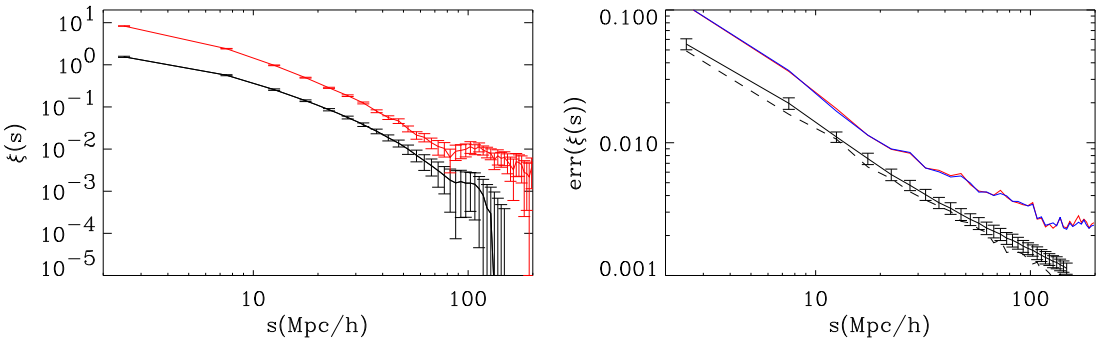

Figure 9.12: Left: Monopole $\xi(s)$ with errors for MICE simulations (black lower signal) and for LRG (red higher signal) using a bin=5Mpc/h. Right: Diagonal error for MICE simulations (JK with dispersion solid black line, MC dotted black line) and for LRG data (red for $N_R = 10$ and blue for $N_R = 20$)

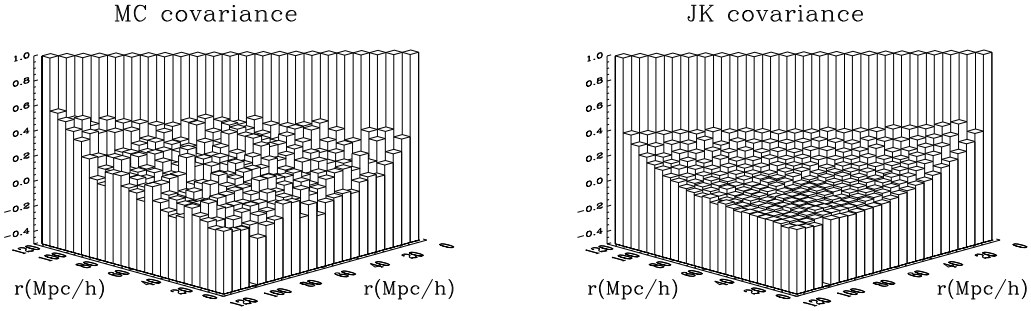

Figure 9.13: Covariance MC and JK for the monopole of $\xi(s)$ for MICE simulations and binning=5Mpc/h

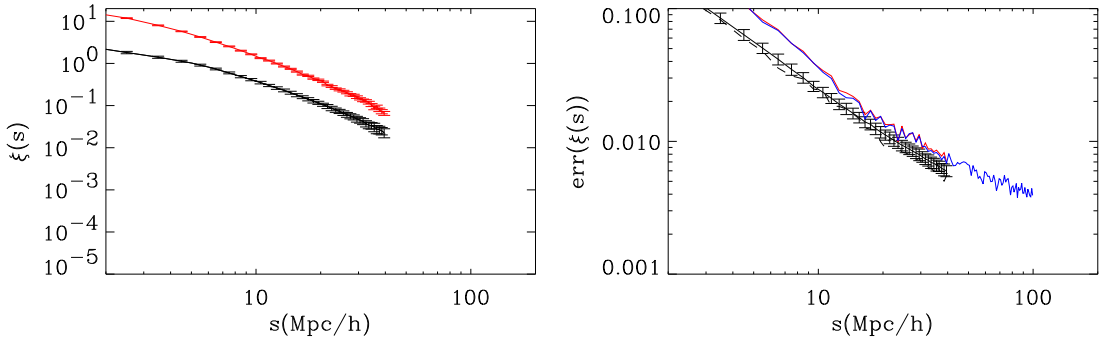

Figure 9.14: Same as Fig.9.12 but bin=1Mpc/h

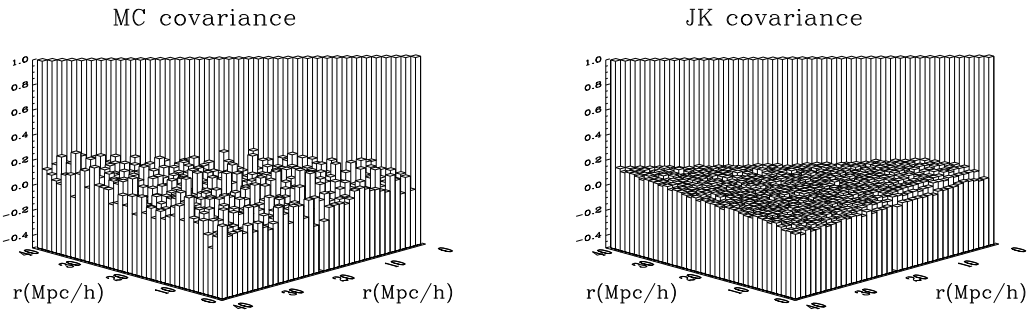

Figure 9.15: Covariance MC and JK for the monopole of $\xi(s)$ for MICE simulations and binning=1Mpc/h

9.4.3 Error in the quadrupole $Q(s)$

In the quadrupole, the JK error also works well, as we can see in Fig.9.16 and Fig.9.17 for 5Mpc/h and 1Mpc/h binning. The solid line with errors shows the JK error and its dispersion, the dotted line is the MC error, and the color and lower line is the JK error in LRG data. The error for LRG data, in the quadrupole, is lower than the simulations one, again because it is proportional to the signal, and in this case, LRG signal is lower (since Q(s) depends on β which depends inversely on bias).

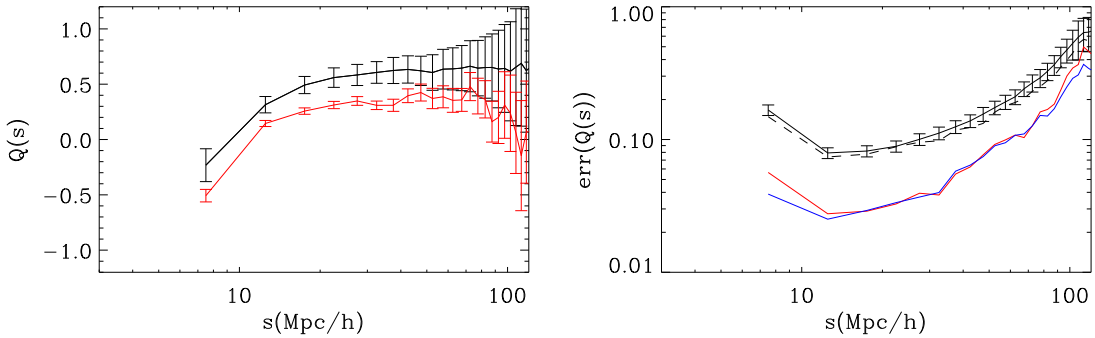

Figure 9.16: Left: Q(s) with errors for MICE simulations (black higher signal) and for LRG (red lower signal) using a bin=5Mpc/h. Right: Diagonal error for MICE simulations (JK with dispersion solid black line, MC dotted black line) and for LRG data (red and blue for $N_R = 10$ and $N_R = 20$)

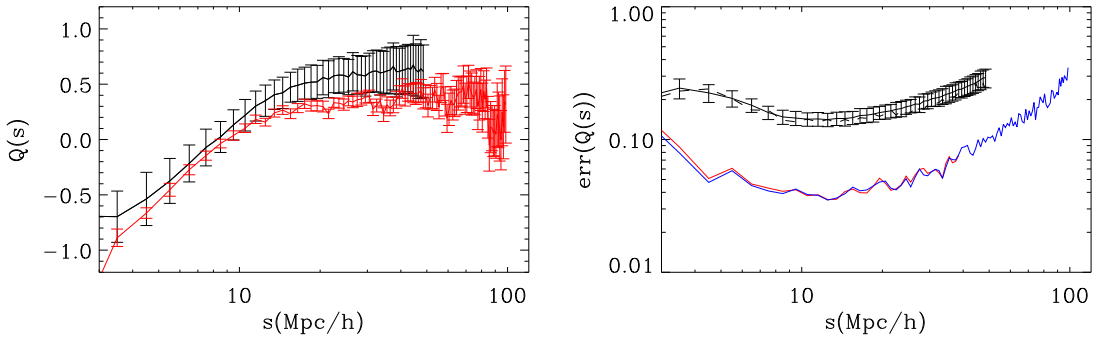

Figure 9.17: The same as Fig.9.16 for bin=1Mpc/h

9.4.4 Errors in the projected correlation function $\Xi(\sigma)$

9.5 Gaussianity in the errors

In this section we study the assumption of Gaussianity when we use the chi-squared test χ^2 in $\xi(\pi,\sigma)$. We could in principle use the test χ^2 despite non-Gaussianity, but then the interpretation requires some changes. We evaluate if the expression $\Delta\xi(\pi,\sigma) = (\xi(\pi,\sigma) - \widehat{\xi}(\pi,\sigma))/\sigma_\xi$ used in the estimation of χ^2 is Gaussian, where $\xi(\pi,\sigma)$ is the value for each MC simulation, $\widehat{\xi}(\pi,\sigma)$ the mean over all the simulations, and σ_ξ the error calculated using the analytical form (to normalize the expression). Fig.9.18 shows the histogram for all the MC simulations, and we see that the expression is Gaussian for different values of π and σ and also for the mean over all the values of $\pi - \sigma$. Now, we know that a reduced chi-squared of 1 is a good fit ($\chi^2_r = \chi^2/(N-1)$) because the statistics χ^2 follows a Gaussian, so we can discard the models that have bigger values.

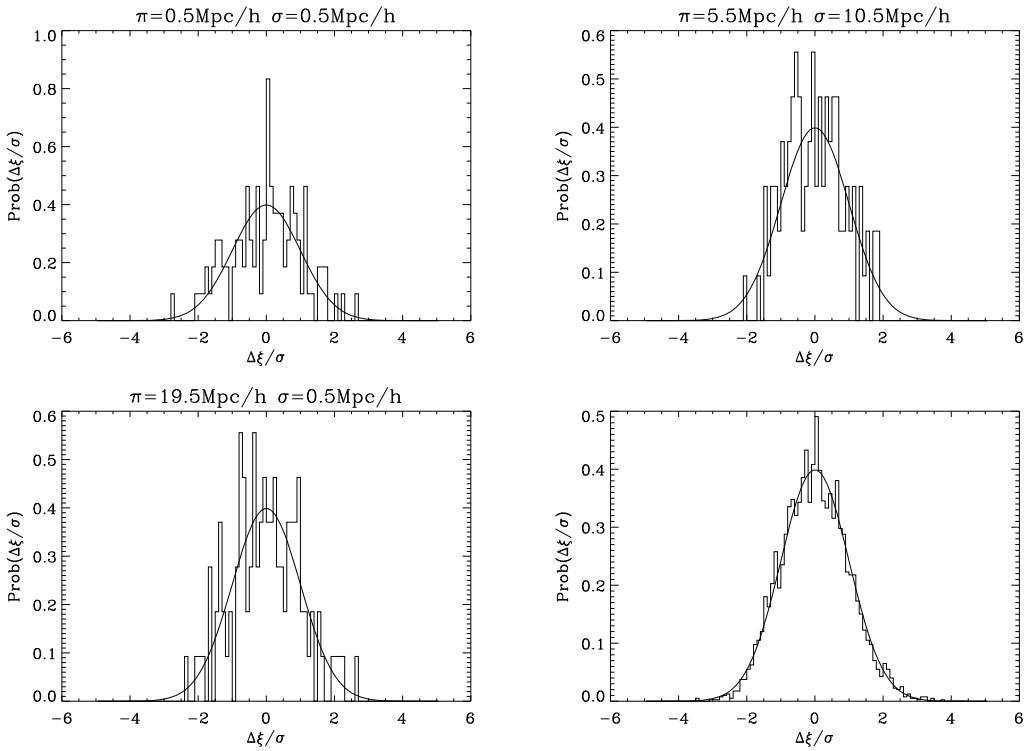

Figure 9.18: Histogram for the relation $\Delta\xi(\pi,\sigma) = (\xi(\pi,\sigma) - \widehat{\xi}(\pi,\sigma))/\sigma_\xi$ for different π and σ as indicated in the top of the figures and also the mean over all the range $\pi - \sigma$ (bottom right)

9.6 Peculiar velocities

We have also used the simulations to see how the particles move, and specially we study the change of the pairwise velocity distribution with distance. We have used MICE simulations at the comoving output z=0.3, where we have done all the study of errors. We also study the difference between a comoving output at z=0. and a catalog of halos extracted from the same redshift, z=0.

First, we show the differences for the velocity distribution: 3D (Fig.9.19), LOS (Fig.9.20) and perpendicular (Fig.9.21). We see no significant differences between the three outputs, as we expected. Now we move to the pairwise velocity distribution. In Fig.9.22, 9.23 and 9.24 we can see the LOS pairwise velocity distribution for different separations in real space. The dispersion is wider for lower distances, but it follows always a quasi exponential form. Its dispersion is represented in the bottom plot versus distance of separation. We can say that σ_v is almost constant for $r > 5Mpc/h$. For redshift 0. we have the same tendencies, but the dispersion is slightly higher, and for the halos at redshift=0. compared to particles at the same redshift, we see clearly an exclusion for small scales, due to the method used to identify halos, friends of friends. At large scales, the dispersion is slightly lower.

The pairwise velocity is similar if we work with particles of dark matter or halos, although the bias in the clustering is clearly different. This means that at large scales, the velocity is not biased. And at small scales, the pairwise velocity in halos does not give us information since there is an exclusion. In real data, the pairwise velocities at smaller scales will depend on the combination halo-halo, halo-satellite and satellite-satellite (explained in §10.1).

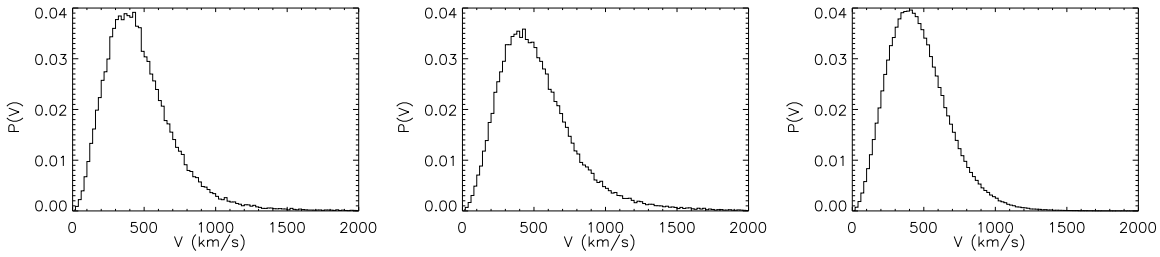

Figure 9.19: Distribution of velocities in MICE simulation at z=0.3, z=0. and halos in z=0.

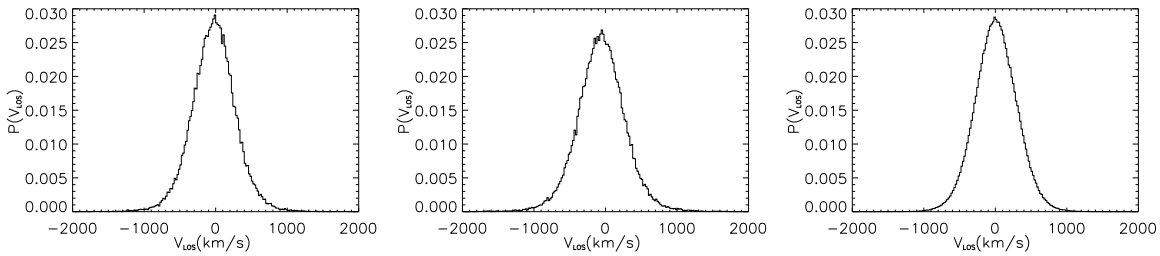

Figure 9.20: Distribution of line-of-sight velocities in MICE simulation at z=0.3, z=0. and halos in z=0.

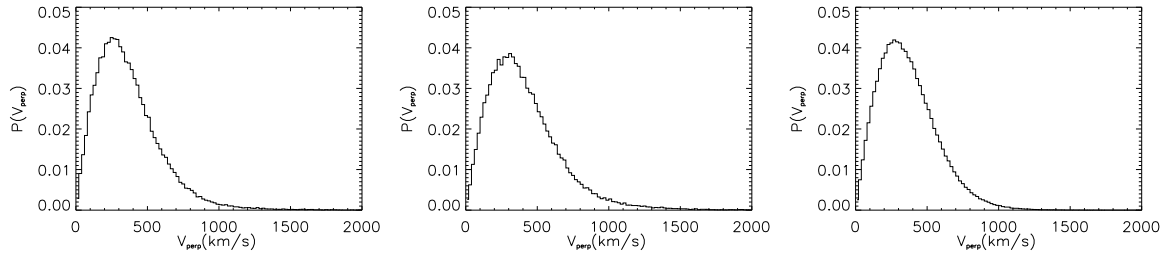

Figure 9.21: Distribution of perpendicular velocities in MICE simulation at z=0.3, z=0. and halos in z=0.

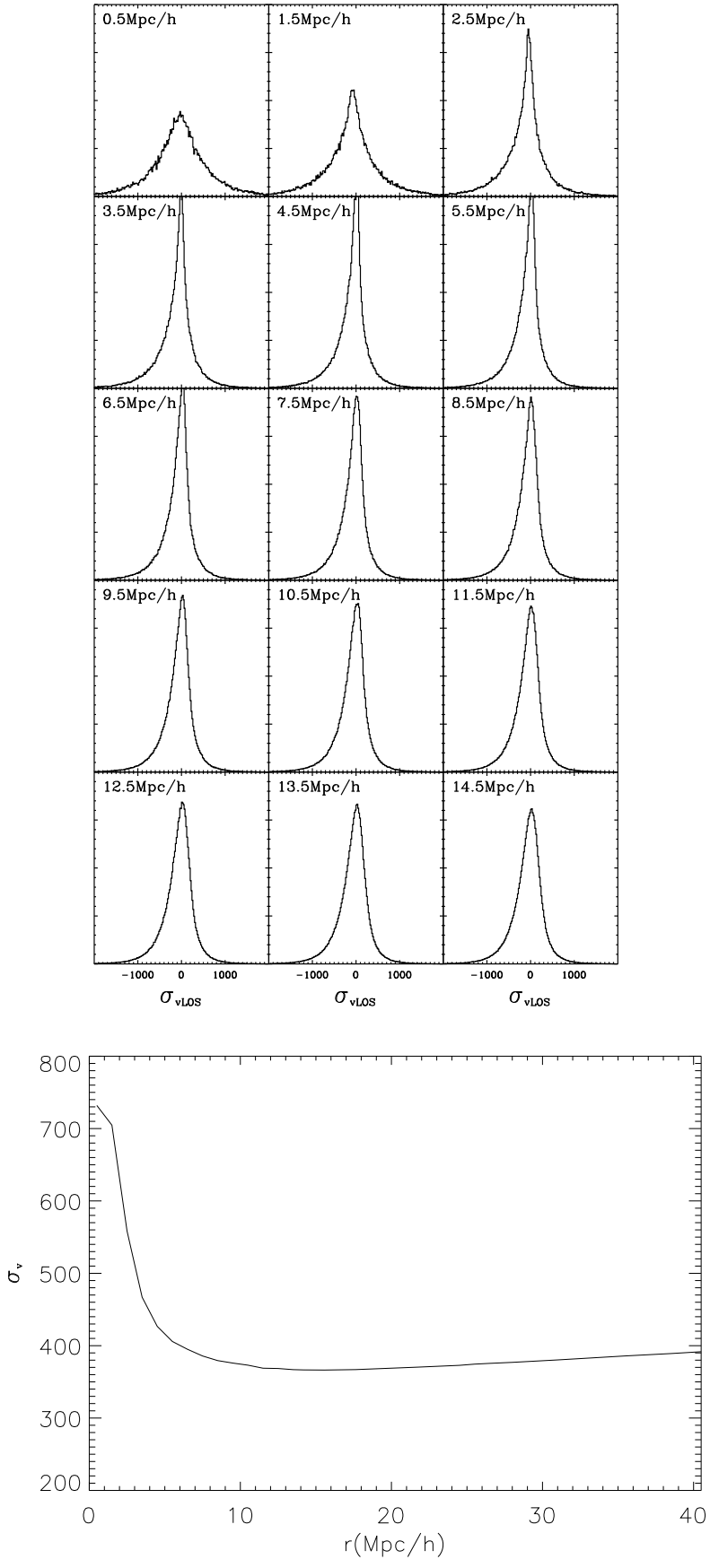

Figure 9.22: Top: Pairwise LOS velocity distribution for the comoving output at z=0.3, for different separations in real space, as indicated in the figure. Pairwise velocities < 0 mean that particles are falling to each other in LOS direction , > 0 mean that they are going away from each other. Bottom: Dispersion in the velocity distribution when we change the distance between particles

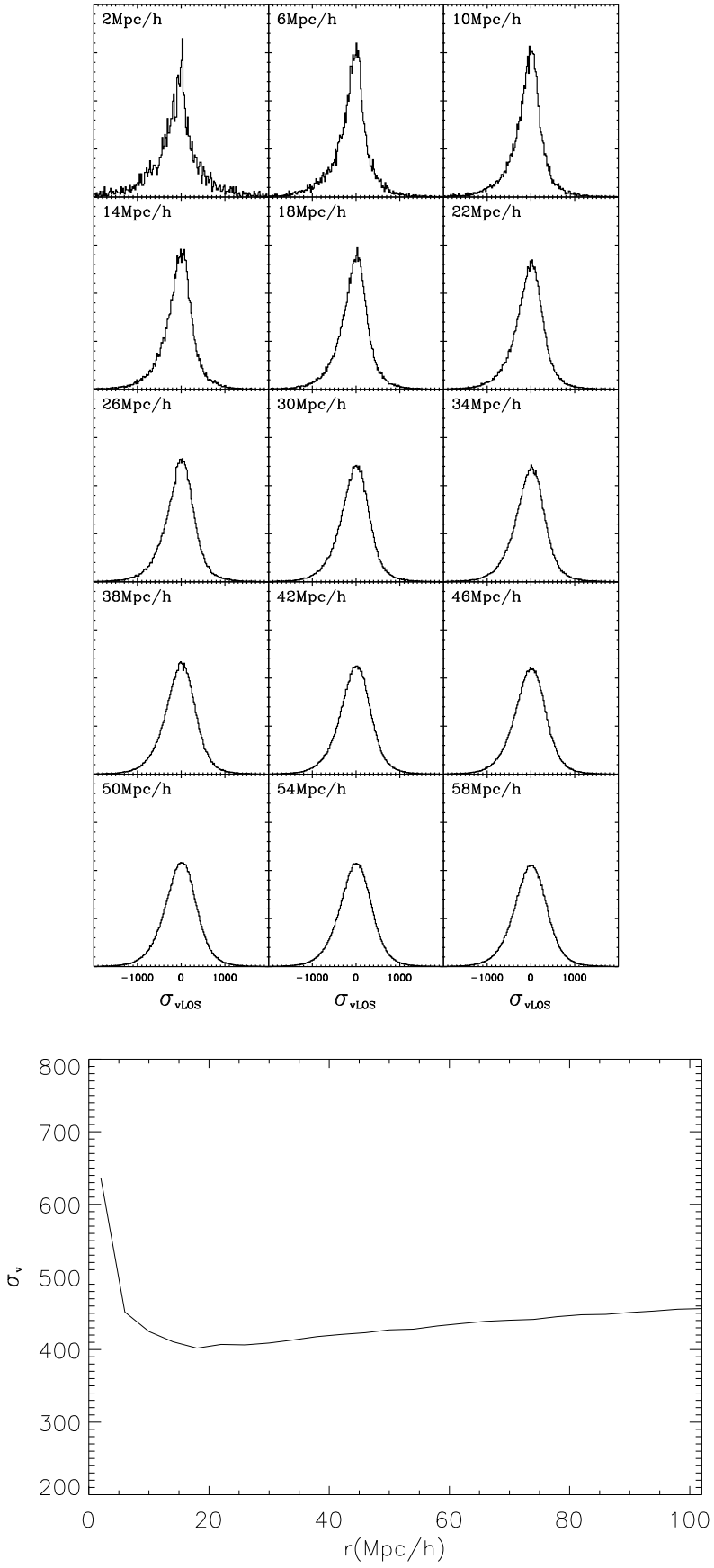

Figure 9.23: Pairwise LOS velocity distribution for the comoving output at z=0., as in Fig.9.22

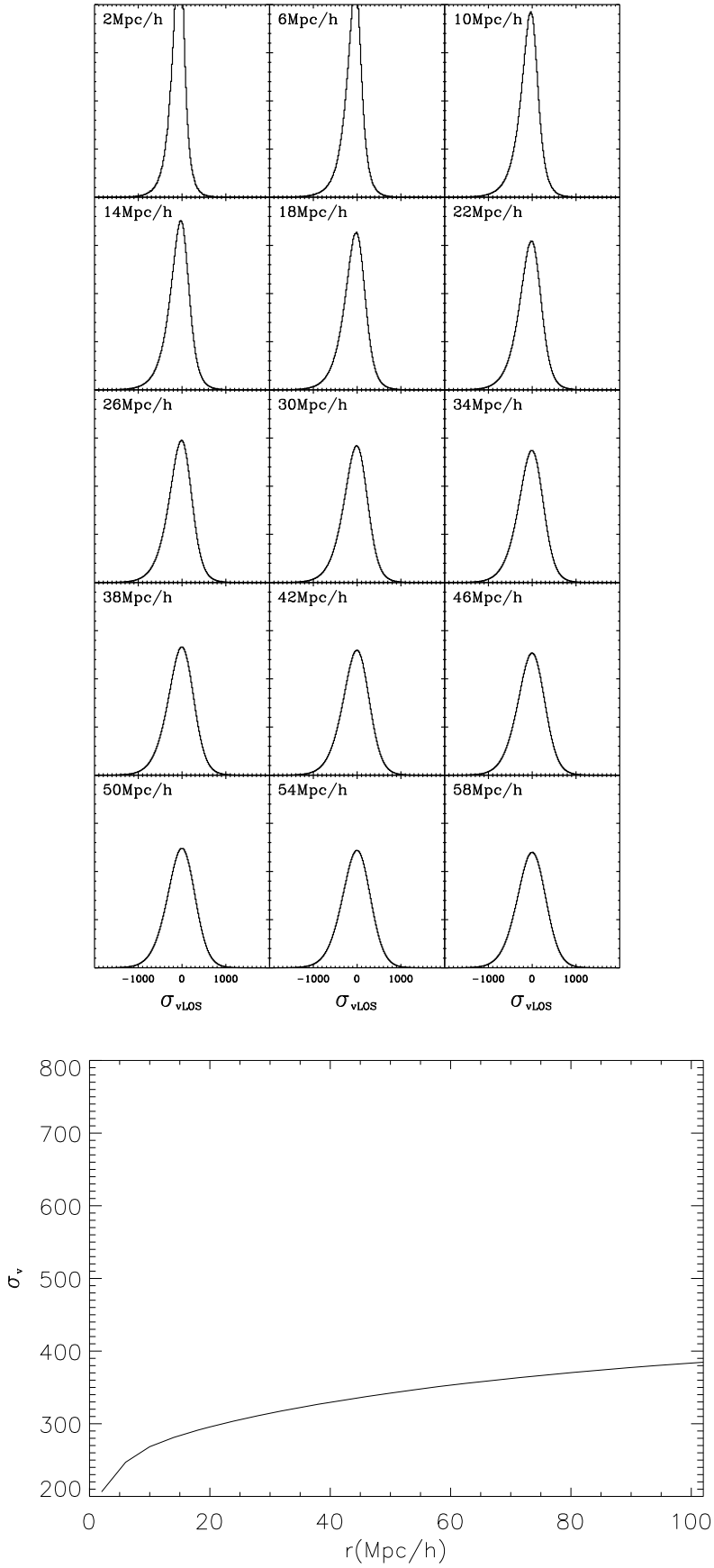

Figure 9.24: Pairwise LOS velocity distribution for the halo comoving output at z=0., as in Fig.9.22

9.7 Validity of the models

Apart from studying the errors, we use the simulations to test the methods that we will apply to real data (LRG) in the following chapter. We want to study if we recover the input parameters.

We first calculate the 2-point real-space correlation function and compare it to the input model that describes the simulation. We recover it perfectly. After that, we look to the ratio $\xi(s)/\xi(r)$ between the redshift space and real space, which should be a function of the distortion parameter β for large scales and for the distant observer approximation, as in Eq.(8.24). In Fig.9.25 we have plotted the mean ratio over the simulated mocks, with its error, and over-plotted in red the expected value for the ratio at $\beta = 0.62$ as in the input model (see §9.1). It seems to converge below 10Mpc/h, which is in agreement with other analysis (see Fig.13 in Hawkins et al. 2003). We could obtain β from the ratio $\xi(s)/\xi(r)$, but it is difficult in real data since we do not have direct information of the real-space, only through integration of the anisotropic $\xi(\pi, \sigma)$ through the line-of-sight (see §8.5).

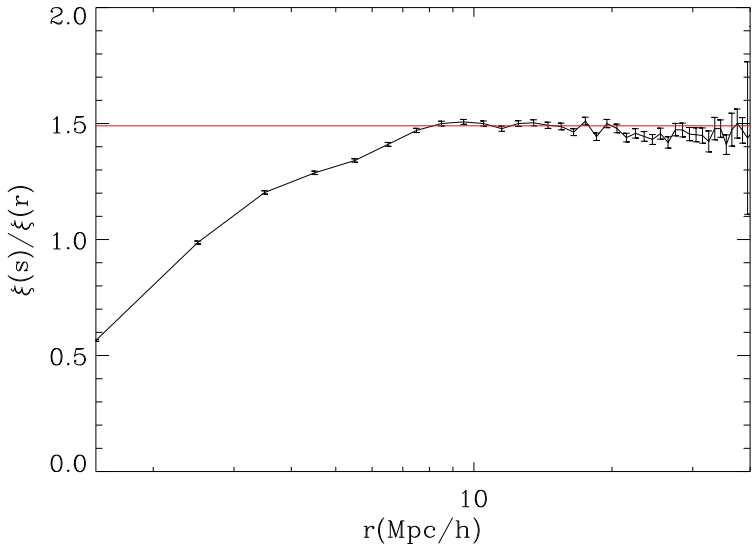

Figure 9.25: Mean $\xi(r)/\xi(s)$ over MICE mocks with errors (of the mean, scaled as $1/\sqrt{nsim}$), and Kaiser prediction for large scales for $\beta = 0.62$, corresponding to the input model (red)

As we will explain later (§10.5), we prefer to obtain β and σ_v contours from the quadrupole Q(s) defined in Eq.(8.17). For the simulations, $\beta = 0.62$ (see §9.1) and σ_v is near 400km/s at large scales (see Fig.9.22). If we fit the quadrupole obtained to all the mocks, we obtain the correct value for β and a little biased σ_v to higher values, probably because we are obtaining an effective σ_v which also accounts for the values at lower scales, although at $1 - \sigma$ is consistent. At the top panel in Fig.9.26, we show the mean contour $\beta - \sigma_v$ which is the average over the individual contours in each simulation, obtained from $Q(s)$; at the bottom panel, we see the best fit over-plotted over the mean Q(s) with the MC errors.

MC errors correspond to a single mock, while errors in the mean value are $\sqrt{N}$ times smaller (N=216 in our simulations). In the bottom panel of Fig.9.26, we plot the errors cor-

responding to a single mock.

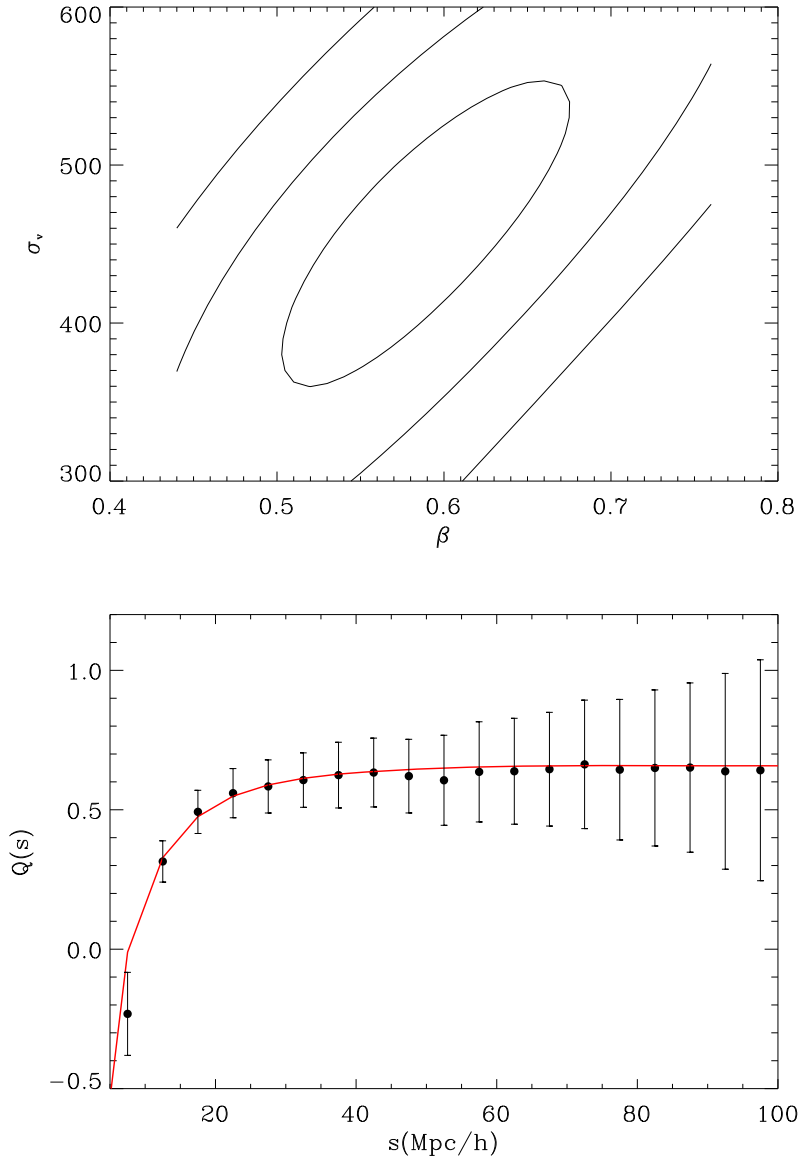

Figure 9.26: Top panel: Mean best fit $\beta - \sigma_v$ to MICE quadrupole Q(s). Bottom panel: Q(s) with MC errors (points), and best model (red)

From large scales, we obtain the shape of the correlation function, defined by Ω_m and the amplitude, as explained in §10.6. As we have seen in chapter 8 we can not rely on the projected correlation function at large scales, or the recovered real space correlation function, so the only way to extract information about the shape of the real space correlation function using the same data is from $\xi(\pi, \sigma)$. We try to recover Ω_m and the amplitude (bias=1 in this case) for each mock once marginalized with σ_v and β. We arrive to the conclusion that small scales are not useful to determine Ω_m, as expected, since it is at large scales where Ω_m changes mostly the shape. Moreover, fingers of God and also the non-linear bias affect small scales. If we use large scales until around 100Mpc/h, the obtained Ω_m is biased to lower values, prob-

ably because we introduce the BAO peak which is not well modeled by the simplest halofit model, or because of the wide angle approximation, that can bias the parameters for large σ (perpendicular direction). The best place to fit Ω_m and a linear amplitude independent on scale is then for intermediate scales from 20Mpc/h to 60Mpc/h to be safe from non-linear bias and extracting an angle of 30-40 deg from the line-of-sight, where fingers of God can alter the information.

For small scales, we calculate the projected correlation function $\Xi(\sigma)$ and the recovered real-space correlation function $\xi(r)$. In our simulations we can calculate directly the real-space correlation function, which is the one expected for dark matter, and we can also calculate $\xi(\pi, \sigma)$ with the redshift distorted simulations, and through the integration of $\xi(\pi, \sigma)$ to π direction, obtain indirectly $\Xi(\sigma)$ and $\xi(r)$. In real data, we only have the second option, so we use the simulations to see if the recovered $\xi(r)$ is the same as the one directly calculated. We recover it with high precision almost completely apart from large scales (see Fig.**??**), as expected (see Ch.8). However, the errors are higher when we recover the real-space correlation function than when we obtain it directly, as seen in Fig.**??**.

Finally, we plot $\xi(\pi, \sigma)$ at small scales and large scales for the mean over MICE mocks in Fig.9.27, and over-plot in solid lines the best model (using Eq.(8.14)). For σ larger than 5Mpc/h we use the effective $\sigma_v = 400km/s$ while for σ lower than 5Mpc/h we use a different σ_v (as seen in Fig.9.22) for each σ constant along the LOS π. With this simple approximation, we get to reproduce the observed FOG. When dealing with real data, we explain a method, proved with simulations, to calculate this σ_v at small scales (see §10.7.1). The model works incredibly well even at small scales, except from large scales in σ direction where there are some changes probably due to wide angle approximation, and the model does not explain the peak at LOS direction, since our model does not include non-linearities that can be important in the BAO peak, although in Fig.9.28 it seems that this difference can be explained by noise, where we have used the MC errors. We also plot the monopole in the BAO and the linear model (dashed black and color lines), and we see that the monopole is modified by redshift distortions and non-linear effects. We will see this later on.

As we have said, in the bottom panel of Fig.9.27 we see the $\xi(\pi, \sigma)$ for the mocks, which have the same selection function, although a more compact area, than real LRG data (see Fig.9.1 for a plot of the difference in area). We see that the obtained correlation (colored) differs from the distant observer approximation theory (lines) at large σ and $\pi \backsim 0$. The redshift space correlation in real surveys, which are not located at infinite, depends on π and σ, but also on the angle between galaxies θ and the angle γ_z between the direction LOS (at $\theta/2$) and the vector which goes from galaxy 1 to galaxy 2 (following the notation used in Matsubara 2000a). In distant observer approximation we assign to the angle between galaxies the value $\theta = 0$. Matsubara (2000a) studies the differences between the real correlation and the approximated correlation for distant observers. In general, the approximation is good for angles θ below 10 deg, which include all the zone we are using for our analysis in LRG data (the worst case comes from the closest galaxies at z=0.15, where $\sigma \backsim 80Mpc/h$ for $\theta = 10deg$). The correlation also depends on γ_z. We can see in Fig.9 of Matsubara (2000a) a comparison between the real correlation, which depends on the distance between galaxies and both angles described above, and the distant observer correlation function, used in this work, which depends only on π and σ. Each position in the 2 dimensional $\pi - \sigma$ is a mixing of different θ and γ_z, because there is a range in redshift, but we can explain qualitatively the lack of power of the observed correlation respect to the distant observer approximation

theory at large σ and $\pi \backsim 0$.

We conclude that all the methods that we use from now to obtain parameters from LRG are validated by simulations.

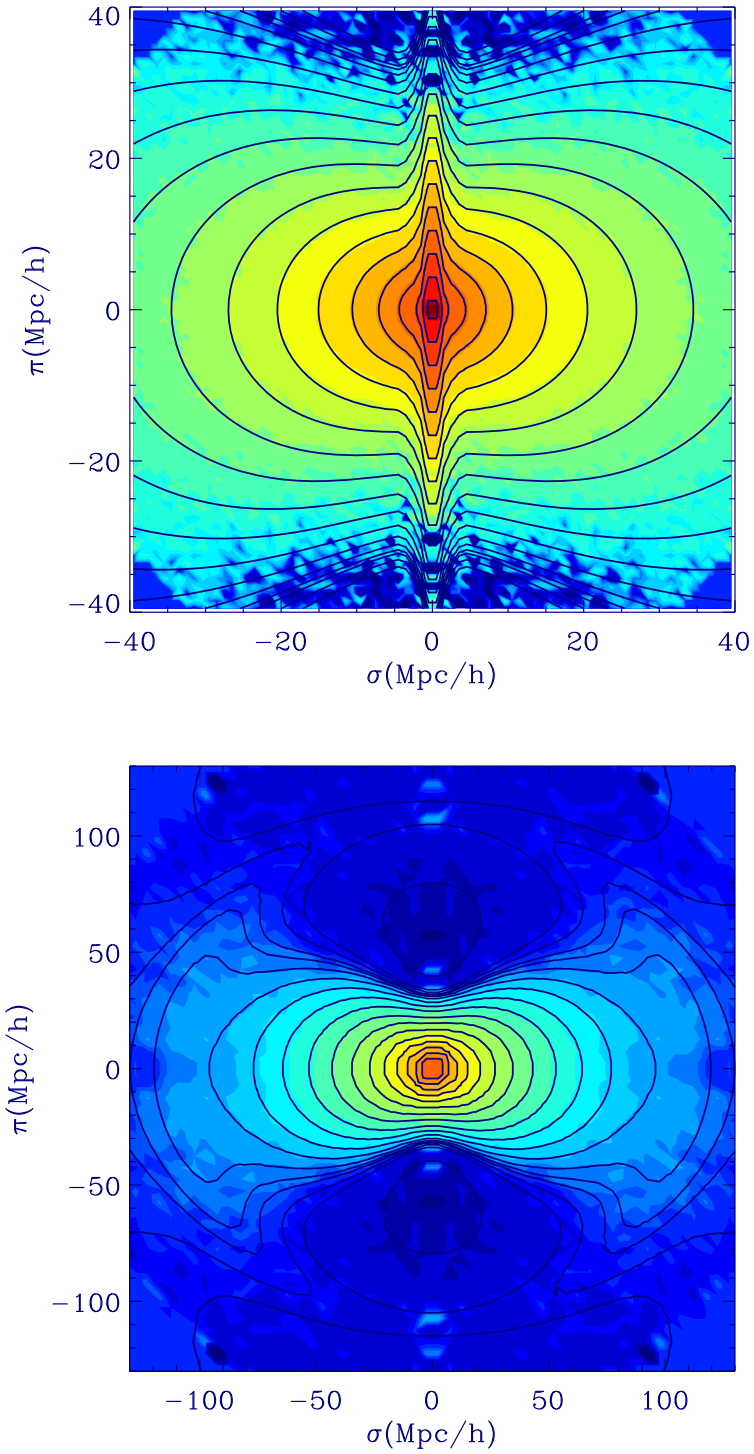

Figure 9.27: $\xi(\pi, \sigma)$ for the MICE simulation. The contour colors are -0.05, -0.01, -0.005, -0.001, 0, and 0.001 to 20 with 20 equally spaced logarithmic bins

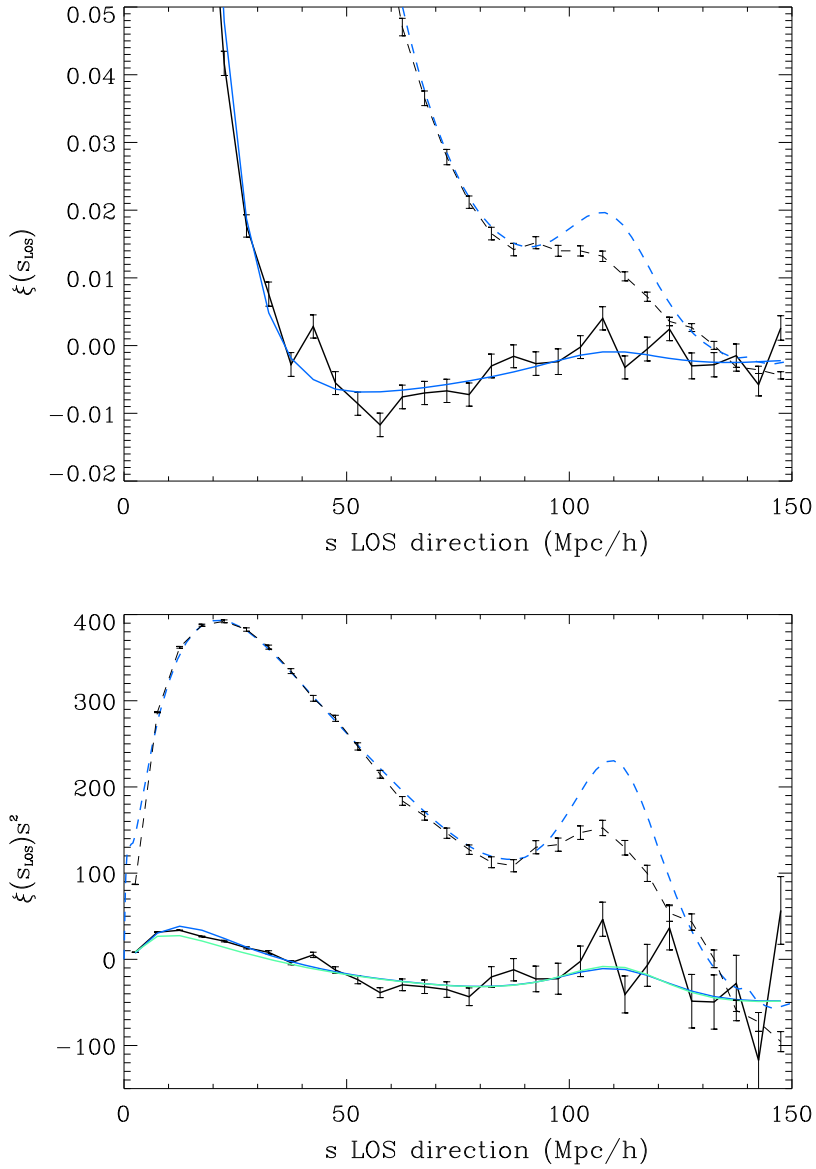

Figure 9.28: Top panel: Mean $\xi(s_{LOS})$ (solid black) for the simulations, with errors ($= err_{MC}/\sqrt{N}$) and over-plotted the linear distorted model in the LOS with $\sigma_v = 600km/s$ (solid blue). We also plot the monopole (dashed black) and the linear model in dashed blue (We have multiplied the monopole for a bias=3 to distinguish clearly the monopole from the LOS correlation) Bottom panel: We plot $\xi(s_{LOS})s^2$ in order to see better the peak. The solid green line corresponds to $\sigma_v = 400km/s$. We also plot $\xi(s)s^2$ with bias=3 (dashed lines)

Chapter 10

Luminous Red Galaxies analysis

The luminous red galaxies (LRGs) are selected by color and magnitude to obtain intrinsically red galaxies in SDSS (Eisenstein et al. 2001). These galaxies trace a big volume, around $1Gpc^3h^{-3}$, which make them perfect to study large scale clustering. LRGs are supposed to be red old elliptical galaxies, which are usually passive galaxies, with relatively low star formation rate. They have steeper slopes in the correlation function than the rest of galaxies, since they reside in the centers of big halos, inducing non-linear bias dependent on scale, for small scales. They are well known galaxies, so they represent a good chance to use it as dark matter clustering tracers.

In this work we use the most recent spectroscopic SDSS data release, DR6 (Adelman-McCarthy et al. 2008), to perform a study combining all the scales of the anisotropic 2-point correlation function, and its derivatives projected correlation function, real-space correlation function, and different order redshift space multipoles; with the subsequent studies of linear bias at large scales to obtain cosmological parameters, and non-linear bias at smaller scales. As we will see, we can break the degeneracy between *bias* and σ_8 present in the correlation function thanks to redshift distortions anisotropies, and look at the growth history and possible modifications of the gravity. We also obtain information from the baryon acoustic peak in the line-of-sight (LOS), which could be enhanced by magnification bias, and only depends on H(z) in the radial direction, obtaining independent information of Ω_m and the dark energy equation of state parameter $w(z)$, through the variations of the peak location. We have cross-correlated LRGs with WMAP in order to investigate the ISW effect again, obtaining a high signal as in the first part of the thesis compared to current theories. We can break the degeneracy $bias - \sigma_8$ and study the growth history using the cross-correlation between temperature of CMB and galaxies w_{TG}, both from another point of view than the used in redshift distortions.

We should point out that the spectroscopic LRG catalog used in this part of the thesis is different from the photometric sample that we used before, not only in the number of galaxies, but also in the selection function in redshift. Photometric LRGs are supposed to be at higher redshifts, around z=0.5, than the spectroscopic redshift (z=0.35).

In this work, we define the parameters we assume during all this work, which are motivated by recent results of WMAP, SNIa and previous LSS analysis: $n_s = 0.98$, $\Omega_b = 0.045$, $h = 0.72$. We will use the power spectrum analytical form for dark matter by Eisenstein & Hu (1998), and the non-linear fit to halo theory by Smith et al. (2003).

10.1 Clustering of LRG

Galaxy clustering allows us to study different phenomena at each scale. On large scales, the density fluctuations are small enough to be linearized, and there we can constrain cosmological parameters, since we can assume that the clustering is described by dark matter. On smaller scales, we can learn about the relation of galaxies to dark matter through the biased clustering of halos. This range of distances can be fitted by a power law, but there are small deviations that can be understood in the theory of the halo occupation distribution. The transition between galaxy pairs of the same halo and galaxy pairs that belong to different halo, occurs around 1Mpc/h. When moving to scales smaller than 1Mpc/h, in the 1-halo term, we can see processes more complex that modify the galaxy clustering, such as dynamical friction, tidal interactions, stellar feedback, and other dissipative processes.

The same LRGs (but with reduced area) have been studied from different points of view. Tegmark et al. (2006) have done an analysis of the power spectrum at large scales to obtain cosmological parameters. Zehavi et al. (2005) study LRGs at intermediate scales (0.3 to 40Mpc/h), where they calculate the projected correlation function, the monopole and real-space correlation function to study mainly the linear high bias, the non-linear bias and the differences between luminosities, remarking that there are differences from a power law for scales smaller than 1Mpc/h. At smaller scales, Eisenstein et al. (2005a) do a cross-correlation between spectroscopic LRG with photometric main sample in order to reduce shot-noise in small scales clustering, obtaining mainly the same conclusion than in the intermediate scales. Finally, Masjedi et al. (2006) deal with very small scale clustering to scales smaller than 55" by cross-correlating the spectroscopic LRG sample and the targeted imaging sample and find that the correlation function from 0.01-8Mpc/h is really close to a power law with slope -2, but there are still some features that diverge from the power law. The small scale slope depends on the interplay between two factors which control how the correlation function of galaxies is related to that of the underlying matter : the number of galaxies within a dark matter halo (HOD) and the range of halo masses which contain more than one galaxy (Benson et al. 2000). LRGs are to be found in halos with the median of the distribution occurring at $3\ 10^{13} M_{\odot}/h$, estimated using weak lensing measurements (Mandelbaum et al. 2006). 25% of LRGs at z = 0.24 are satellite galaxies (Almeida et al. (2008)), which play an important role in the pairwise velocity dispersion, which also provides information about galaxy formation and evolution.

Slosar et al. (2006) show that pairwise velocity distribution in real space is a complicated mixture of host-satellite, satellite-satellite and two-halo pairs. The peak value is reached at around 1Mpc/h and does not reflect the velocity dispersion of a typical halo hosting these galaxies, but is instead dominated by the sat-sat pairs in high-mass clusters. Tinker et al. (2007) use the halo occupation distribution framework to make robust predictions of the pairwise velocity dispersion (PVD). They assume that central galaxies move with the center of mass of the host halo and satellite galaxies move as dark matter. The pairs that involve central galaxies have a lower dispersion, so the fraction of satellites strongly influences both the luminosity and scale dependence of the PVD in their predictions. At r $\backsim$ 2 Mpc/h, the PVD rapidly increases as satellite-satellite pairs from massive halos dominate. At r < 1 Mpc/h, the PVD decreases with smaller separation because central-satellite pairs become more common. Li et al. (2006) conclude that the reddest galaxies move in the strongest gravitational fields.

While working in this part of the thesis, Okumura et al. (2008) published the first application of the anisotropy in the 2-point correlation function including the baryonic features,

to obtain constraints in cosmological parameters. They use the DR3 spectroscopic sample of LRGs to calculate the 2-point correlation function with a different definition than the one used here (Matsubara 2004) and fit for large scales using the linear Kaiser model, from 40Mpc/h to 200Mpc/h, excluding the FOG zone. They claim that it can be obtained a direct measurement of the growth function from Kaiser anisotropy and $D_a(z)$ and $H(z)$ from the baryon acoustic peak anisotropic, with improved LRG data. The constraints are weak by now, but fitting all the anisotropic 2-point correlation function including the baryonic feature enable to divide the effect of the redshift distortions into dynamical and geometrical components. The anisotropy due to geometric distortion contributes to better estimation of the equation of state of the dark energy.

10.2 BAO detection

Eisenstein et al. (2005b) detected the baryon acoustic peak in the 2-point correlation function using LRGs. Hütsi (2006a,b) use LRGs to constrain cosmological parameters in the power spectrum, including the baryonic peak. Percival et al. (2007a) have analyzed also the LRGs using both 2dF and SDSS. Padmanabhan et al. (2007) used the photometric catalog to work with a bigger set of LRGs with photometric redshifts, obtaining also cosmological constraints, the same as Blake et al. (2007), which work with the MegaZ-LRG, a photometric-redshift catalog of luminous red galaxies based on the imaging data of the SDSS DR4.

With large samples, the BAO can be used as a standard ruler to get parameters such as Ω_m, through the comoving distance-redshift relation (Blake & Glazebrook 2003). Percival et al. (2007b) obtain a value for Ω_m from the position of the BAO peak in LRGs. However, non linear effects act to wash out the oscillations at higher k due to mode coupling (Meiksin et al. 1999, Seo & Eisenstein 2005). Many works have been done in this direction in the power spectrum (Jeong & Komatsu 2006, Padmanabhan & White 2008). They all say that non-linearities are important in the baryon acoustic oscillations. Crocce & Scoccimarro (2008) perform a modeling also in the 2-point correlation function. Nonetheless the problem is aggravated by the need to model scale dependent galaxy bias, which may have already become the strongest limitation on the use of large scale structure information to obtain constraints on cosmological parameters (Sánchez & Cole 2008). A recent work, Sanchez et al. (2008), analyze the relation between the acoustic peak in the two-point correlation function and the sound horizon scale, which can be different by few %, and which is the better statistic to use to constrain the dark energy equation of state, the correlation function or the power spectrum, arriving to the conclusion that all the effects applied to the 2-point correlation function only change the shape, and not the location of the peak, while the analysis is more difficult in the power spectrum. In this work, we just use the location of the peak, and not the overall shape.

LRGs have also been analyzed at higher redshifts (z=0.55) with the 2dF-SDSS LRG and QSO Survey (2SLAQ, Cannon et al. 2007). Ross et al. (2007); da Ângela et al. (2008); Wake et al. (2008) analyze the redshift distortions in the LRGs and quasars for this catalog. For part of our analysis we have followed the method explained in Hawkins et al. (2003), an extensive analysis of the redshift distortions in the 2dF catalog.

10.3 Luminous Red Galaxies data

SDSS luminous red galaxies (LRGs) are selected on the basis of color and magnitude to have a sample of luminous intrinsically red galaxies that extends fainter and farther than the SDSS main galaxy sample. Eisenstein et al. (2001) gives an accurate description of the sample.

LRGs are targeted in the photometric catalog, via cuts in the (g-r, r-i, r) color-color-magnitude cube. Note that all colors are measured using model magnitudes, and all quantities are corrected for Galactic extinction following Schlegel et al. (1998).

The galaxy model colors are rotated first to a basis that is aligned with the galaxy locus in the (g-r, r-i) plane according to:

$c_\perp$= (r-i) - (g-r)/4 - 0.18

$c_{||}$= 0.7(g-r) + 1.2[(r-i) - 0.18]

Because the 4000 Angstrom break moves from the g band to the r band at a redshift z $\backsim$ 0.4, two separate sets of selection criteria are needed to target LRGs below and above that redshift:

Cut I for z $<\backsim$ 0.4

rPetro $< 13.1 + c_{||} / 0.3$

rPetro < 19.2

$|c_\perp| < 0.2$

$mu_{50} < 24.2$ mag $arcsec^{-2}$

r_{PSF} - $r_{model} > 0.3$

Cut II for z $>\backsim$ 0.4

$r_{Petro} < 19.5$

$|c_\perp| > 0.45$ - (g-r)/6

g-r $> 1.30 + 0.25$(r-i)

$mu_{50} < 24.2$ mag $arcsec^{-2}$

r_{PSF} - $r_{model} > 0.5$

Cut I selection results in an approximately volume-limited LRG sample to z=0.38, with additional galaxies to z $\backsim$ 0.45. Cut II selection adds yet more luminous red galaxies to z $\backsim$ 0.55. The two cuts together result in about 12 LRG targets per deg^2 that are not already in the main galaxy sample (about 10 in Cut I, 2 in Cut II).

We k-correct the r magnitude using the Blanton program 'kcorrect' [1]. We need to k-correct the magnitudes in order to obtain the absolute magnitudes and eliminate the brightest and dimmest galaxies. We have seen that the previous cuts limit the intrinsic luminosity to a range $-23.2 < M_r < -21.2$, and we only eliminate from the catalog some few galaxies that lay out of the limits. Once we have eliminated these extreme galaxies, we still do not have a volume limited for high redshift galaxies, but we suppose that the variations in luminosity just change the overall shape in the clustering.

In Fig.10.1, we show the distribution of LRGs in redshift. We show the comoving density in Fig.10.3 once we have removed the brightest and dimmest galaxies, which are plotted in Fig.10.2, absolute magnitude and redshift.

[1] http://cosmo.nyu.edu/blanton/kcorrect/kcorrect_help.html

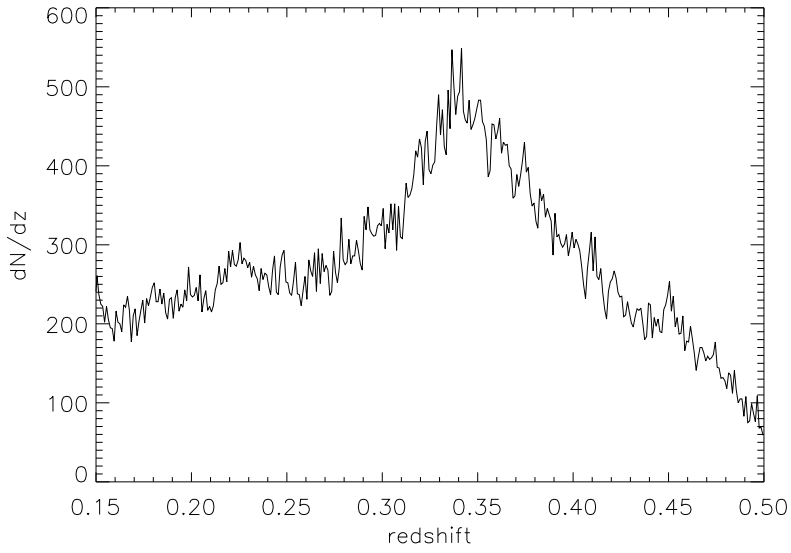

Figure 10.1: dN/dz of LRG galaxies

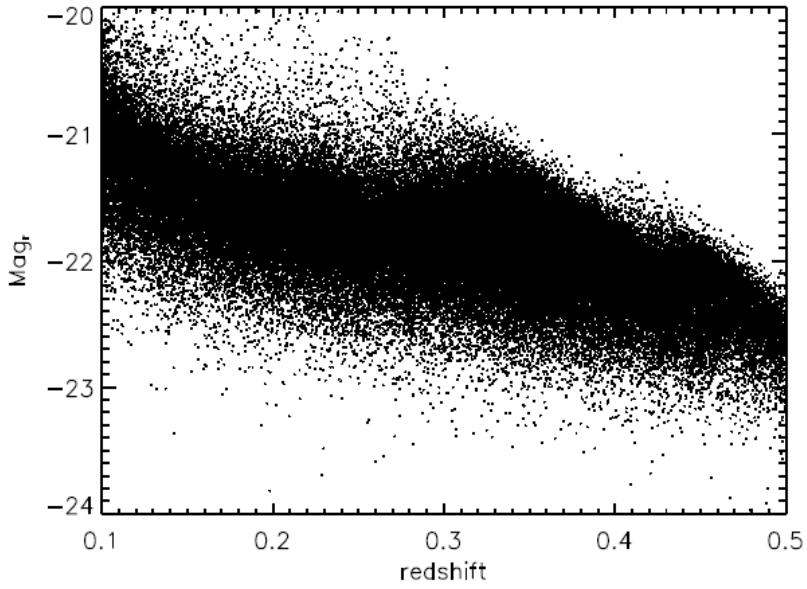

Figure 10.2: Absolute magnitude vs redshift

In Fig.10.4 we can see the distribution of galaxies for the main sample, z=0.15-0.47, and in Fig.10.5 the redshift space clustering in a slice of dec = 32-40 deg. We compare it with the same slice random to see clearly the clustering in the data.

We have masked the catalog using at the first step the photometric DR6 mask, based on the number of galaxies per pixel. In previous works we saw that the mask that we obtain statistically by dropping out the pixels with small number of galaxies gives the same correlation function that the one obtained by extracting the polygons masked by the SDSS team. After that, we compare our masked catalog to the LRG spectroscopic catalog, and we extract manually the zones where there are artificially few galaxies, because the fibers trace a little

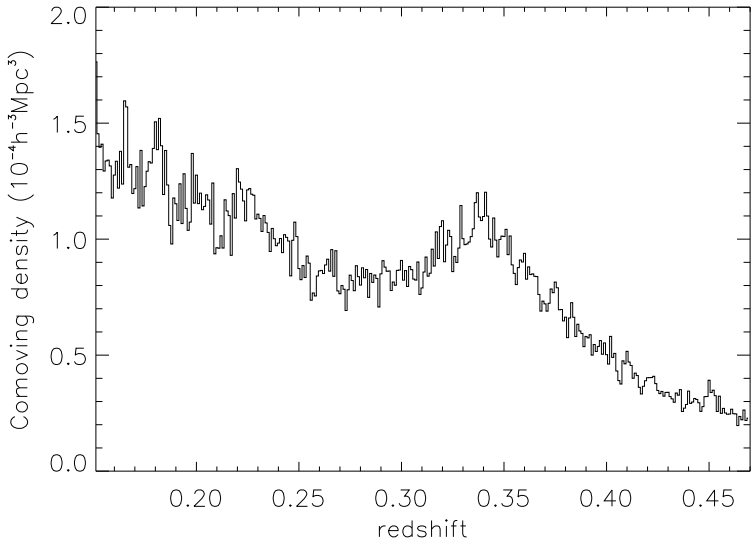

Figure 10.3: Comoving density vs redshift

different mask than the photometric catalog. We are very careful in the mask in order not to extract valuable information.

This rough mask could imprint spurious effects at very small scales, but we are not interested in these scales where fiber collisions in the redshift catalog are limiting our analysis, for distances less than 55arc sec, less than 0.3Mpc/h at the mean redshift of LRG data, z=0.35. We obtain 75,000 galaxies for the final catalog, from z=0.15 to z=0.47.

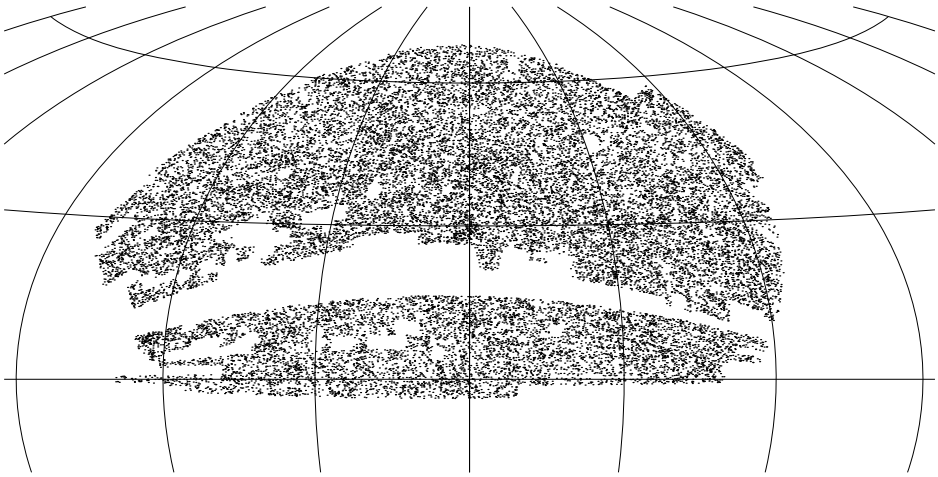

Figure 10.4: Density distribution of galaxies in the main catalog, z=0.15-0.47

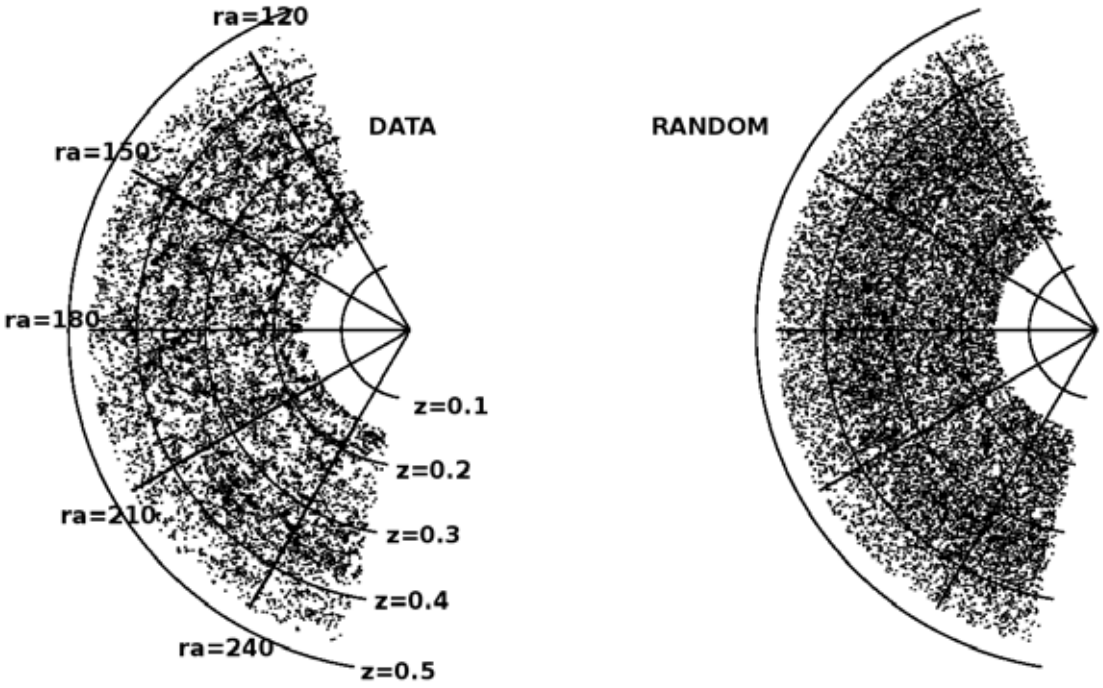

Figure 10.5: Slice in dec = 32-40 deg showing ra vs redshift

10.4 Estimation of the anisotropic 2-point correlation function

We use the ξ estimator of Landy & Szalay (1993),

$$\xi(\sigma,\pi) = \frac{DD - 2DR + RR}{RR} \tag{10.1}$$

to estimate the 2-point correlation function in redshift space, with a random catalog 20 times denser than the SDSS catalog. The random catalog has the same redshift distribution as the data, but smoothed to avoid the elimination of intrinsic correlations in the data, and also the same mask. We count the pairs in bins of separation along the line-of-sight (LOS), π, and across the sky, σ. The LOS distance is just the difference between the comoving distances in the pair. The perpendicular distance between the two particles corresponds approximately to the mean redshift. It is exactly $\sigma = \sqrt{s^2 - \pi^2}$, where s is the distance between the particles. (see Fig.10.6). We use the wide-angle approximation, as we had the catalog at an infinite distance, which is accurate until the angle of separation is 15deg for the quadrupole and below for the $\xi(\pi,\sigma)$, about 10 degrees (see Szapudi 2004 and Matsubara 2000a). This is more than $\sigma = 100Mpc/h$ for our mean catalog. We do not use the information provided by the baryonic scale in σ direction because it could be affected by wide angle corrections. In Fig.10.7 we can see the obtained $\xi(\pi,\sigma)$ for LRG DR6 catalog, and for MICE simulations (with a linear bias=2 to see similarities visually). As expected, simulations have less noise because we have done the mean over 216 simulations. Moreover, the distortion parameter β is higher in the simulations than in data because of the high bias of LRG, as can be seen in the the shape of the 2-point correlation function, more flattened as β increase. In next sections we will analyze all the information hidden in this figure.

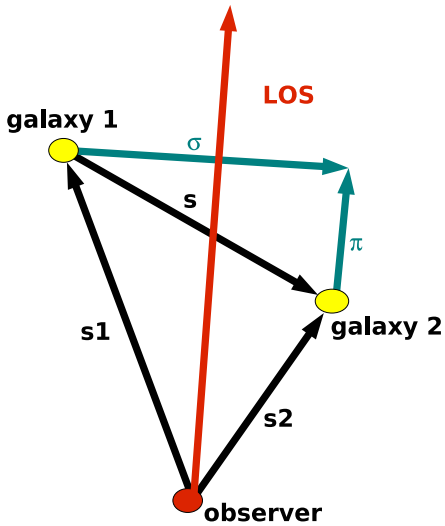

Figure 10.6: Illustration of the parallel and perpendicular separations between two objects

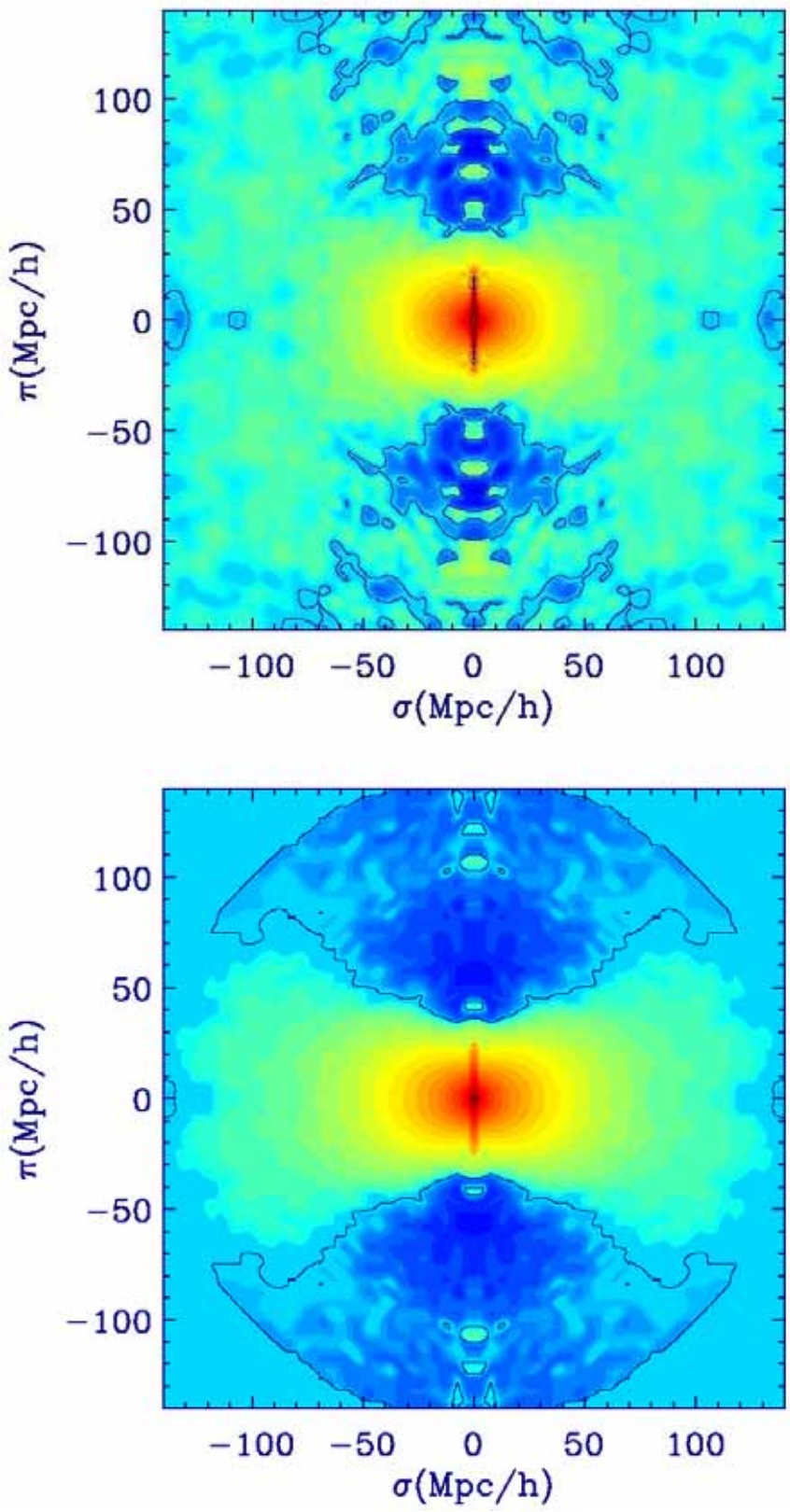

Figure 10.7: 2-point anisotropic redshift correlation function $\xi(\pi, \sigma)$ for LRG galaxies in DR6 catalog and MICE simulations (with a linear bias =2, in order to be similar to LRG). Contours are -0.5 to -0.004 with logarithmic bin of 0.4, 0. (over-plotted), 0.003 to 40. with bin=0.4

10.5 Quadrupole result

We can calculate the multipoles of the 2-point redshift-space correlation function, enhancing different angles of the anisotropy between the LOS and the perpendicular direction. We have tested with models that the monopole $\xi(s)$ and quadrupole $\xi_2(s)$ and even the combination $\xi_2(s)/\xi(s)$ depend strongly not only on β, σ_v, but also on other parameters like the shape of the correlation function (for example, Ω_m), the non-linear bias and the overall amplitude. On the contrary, the quadrupole Q(s), defined in Eq.(8.17) only depends strongly on σ_v and β, but not on the bias. So when using the quadrupole we do not need an expression for the non-linear bias and Ω_m (the shape) to extract information. In §9.4.3 we have shown that JK errors work very well here.

First, we can measure β using the large scales in the quadrupole where there is no dependence in σ_v. In the range $40-80Mpc/h$, $\beta = 0.34 \pm 0.06$; for $50-80Mpc/h$, $\beta = 0.32 \pm 0.08$; and for $40-100Mpc/h$, $\beta = 0.34 \pm 0.05$. In Fig. 10.8 we see the quadrupole with jackknife errors at large scales and the error obtained in β, translated to the quadrupole.

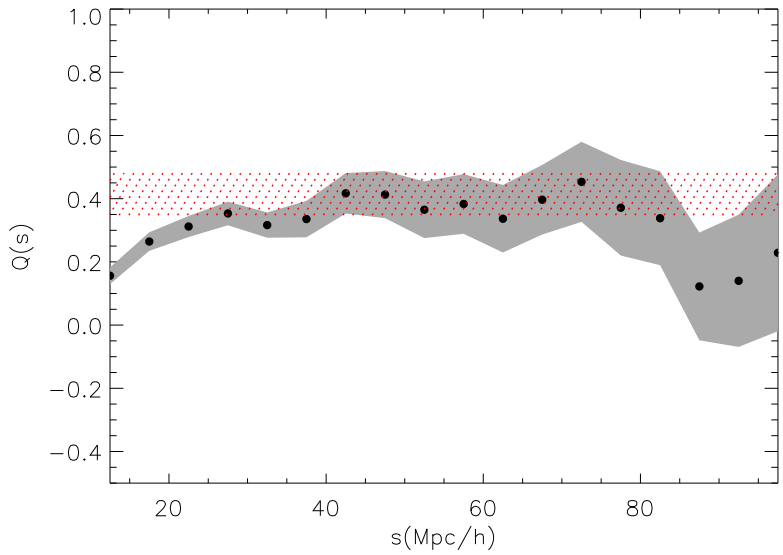

Figure 10.8: Q(s) with errors (points with errors) and best fit for β translated to quadrupole (red dotted)

As mentioned above, the quadrupole only depends strongly on β and σ_v. It does not depend on linear bias because it is canceled, and it does not depend much on the shape of the 2-point correlation function (Ω_m and other parameters) and the non-linear bias for small scales. We have tried to fit β and σ_v using all the scales in the quadrupole, fixing Ω_m (which in our model means fixing the shape of the real-space correlation function) and we use a power law form for the non-linear bias. When we change the shape of the $\xi(r)$ in the model (that is Ω_m for large scales and non-linear bias for small scales) , we obtain the same contours for $\beta - \sigma_v$, so we arrive to the conclusion that the quadrupole is a good estimator to find $\beta - \sigma_v$ separately from the other parameters, which are degenerate with them in $\xi(\pi, \sigma)$.

We fit the quadrupole above 5Mpc, because it is a reliable scale where we do not see differences when fitting from larger scales. Below this minimum scale, σ_v can change, and despite modifying minimally the quadrupole at larger scales, it can bias the measure of β,

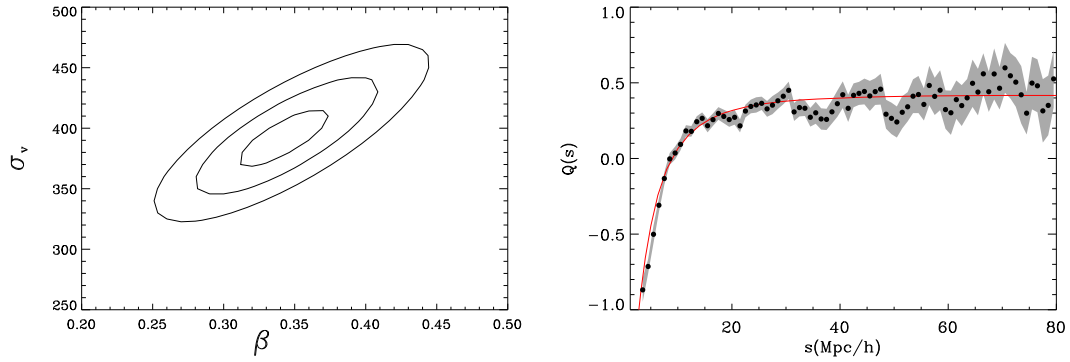

Figure 10.9: z=0.15-0.47, Best fit for σ_v and β for the quadrupole Q(s) distances between 5-60Mpc/h

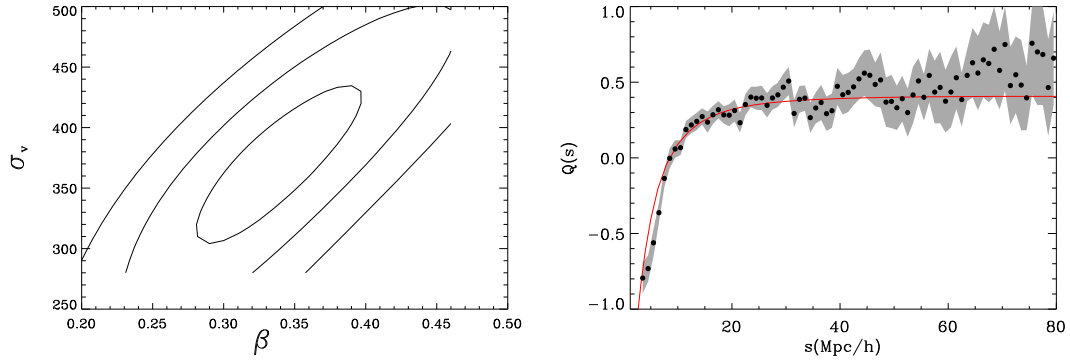

Figure 10.10: z=0.15-0.3, Best fit for σ_v and β for the quadrupole Q(s) distances between 10-60Mpc/h, $\beta = 0.34$, $\sigma_v = 370$.

which constrained with σ_v has better errors.

We have fit $\beta - \sigma_v$ for different slices in redshift. First, we divide the catalog in 3 redshift slices: z=0.15-0.3, z=0.3-0.4, z=0.4-0.47. And then, we divide it in 2 redshift slices: z=0.15-0.34, z=0.34-0.47. The fitted values σ_v and β are similar in all the redshift slices. (see table 10.1)

Sample	$\boldsymbol{\beta}$	$\boldsymbol{\sigma_v}$ **(km/s)**
z=0.15-0.47	0.310-0.375	365-415
z=0.15-0.34	0.280-0.365	320-410
z=0.34-0.47	0.305-0.405	345-420
z=0.15-0.30	0.280-0.395	305-435
z=0.30-0.40	0.285-0.365	335-390
z=0.40-0.47	0.305 -0.395	350-410

Table 10.1: Marginalized values for β and σ_v to 1-σ errors for each sample in redshift

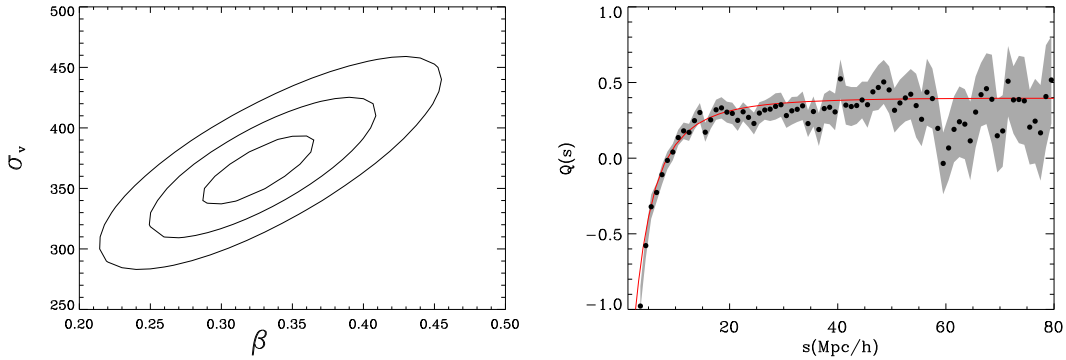

Figure 10.11: z=0.3-0.4, Best fit for σ_v and β for the quadrupole Q(s) distances between 5-60Mpc/h, $\beta = 0.32$, σ_v=360.

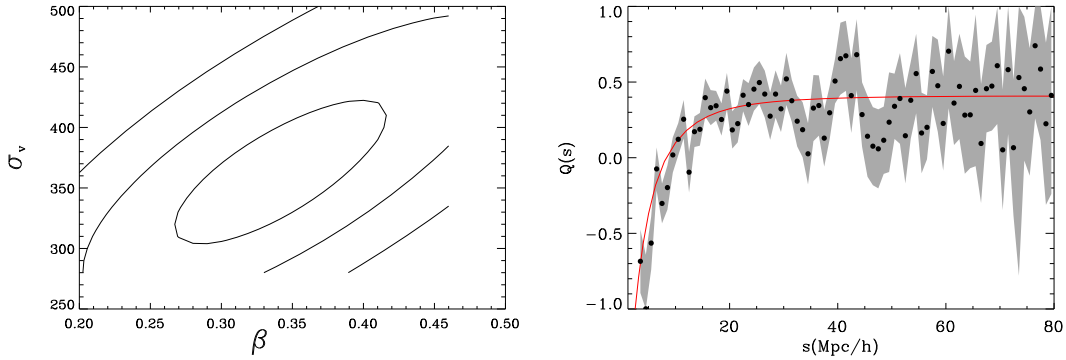

Figure 10.12: z=0.4-0.47, Best fit for σ_v and β for the quadrupole Q(s) distances between 10-60Mpc/h, $\beta = 0.34$, σ_v=380.

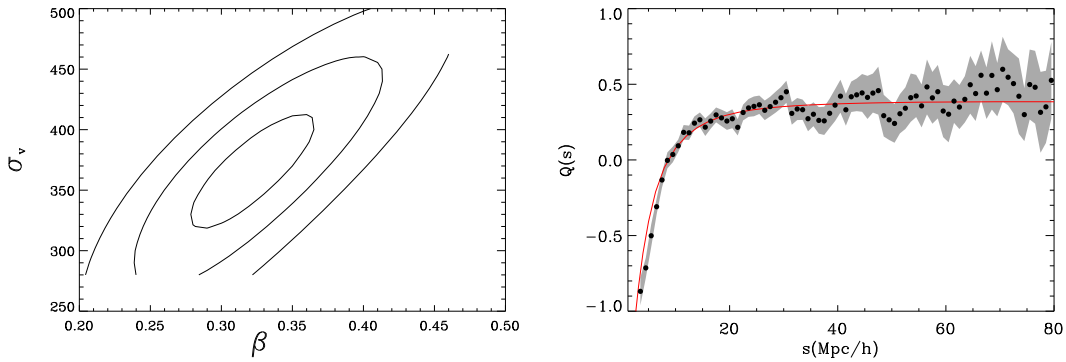

Figure 10.13: z=0.15-0.34, Best fit for σ_v and β for the quadrupole Q(s) distances between 10-60Mpc/h, $\beta = 0.33$, $\sigma_v = 370$.

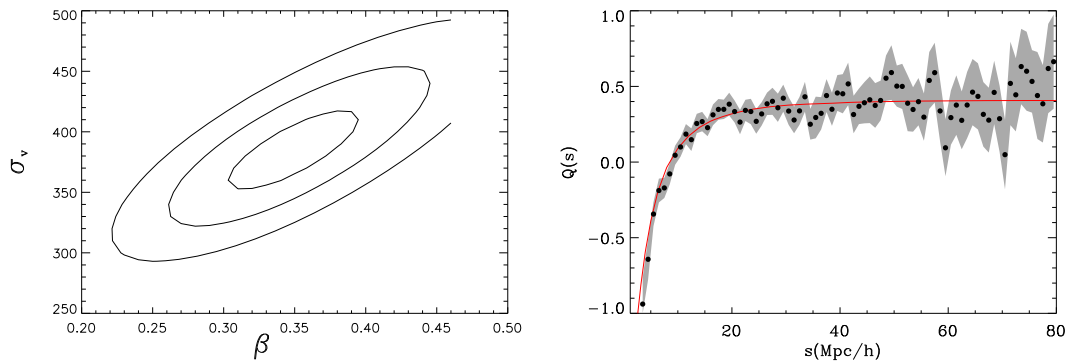

Figure 10.14: z=0.34-0.47, Best fit for σ_v and β for the quadrupole Q(s) distances between 5-60Mpc/h $\beta = 0.34$, $\sigma_v = 370km/s$

10.6 Fitting at large scales

As we have seen in chapter 8 we can not rely on the projected correlation function at large scales, or the recovered real space correlation function, so the only way to extract information about the shape of the real space correlation function using the same data is from $\xi(\pi,\sigma)$. We use models that vary with Ω_m, amplitude, σ_v and β at large scales (from 20 to 60Mpc/h, approximately). The amplitude Amp refers to the factor $b(z)\sigma_8$, where b(z) is the bias at redshift z. $b(z)$ and σ_8 are completely degenerated in the correlation function, also with the growth factor $D(z)$. In fact, what we obtain from observations is $b(z)\sigma_8 D(z)$, but D(z) is known for each cosmology and the median redshift of the slice. We extract the FOG zones, to be safe we eliminate from our analysis an angle of 40 deg from LOS. This way, we have proved using simulations that we can use linear bias and the σ_v and β found using the quadrupole. If we do this fit without $\beta-\sigma_v$ information, we see strong degeneracies. First, between β and σ_v, since β higher can be corrected by also incrementing σ_v, because β tends to flatten the anisotropy while σ_v tends to stretch it when we approach the zone of FOG. Because we have chosen a region which is slightly dependent on the random peculiar velocities, we can not distinguish among β and σ_v. We also see a strong degeneracy between Ω_m and σ_v (directly correlated). The linear amplitude is independent of σ_v, but it is degenerated with β (inversely), and with Ω_m (directly). Finally, β and the amplitude are inversely degenerated. When we fit $\xi(\pi,\sigma)$, we use for each theoretical Ω_m distances calculated using a cosmology with that Ω_m in order to be consistent, although there is not a significant change from using always the same cosmology for the calculation. We do not see any difference when fitting $\xi(\pi,\sigma)$ with models with non-linear bias or linear bias. This is because we are safely located at large scales, although in general in redshift space there is a mixing of scales.

In the plots shown in Fig.10.15 (for the catalog ALL), we have marginalized each contour using the rest of parameters, with subsequent degeneracies explained in the previous paragraph. When we marginalize we suppose that the probability goes like $exp(-\chi^2/2)$. Because σ_v is completely degenerate and we only have fitted for this range of σ_v, the other contours are limited by the chosen σ_v. These figures just want to show the strong degeneracies between parameters, but we are really interested in the contour $\Omega_m - Amp$ once we marginalize using the contour $\beta-\sigma_v$ obtained from $Q(s)$ in §10.5. In Fig.10.15 there are two panels which show contours $\Omega_m - Amp$. The first one when marginalizing among the rest of parameters obtained in the fit at large scales (top right panel). The second one shows the result if we marginalize with $\beta-\sigma_v$ from $Q(s)$.

In the rest of plots, for different redshift slices (see Fig.10.16, 10.17, 10.18, 10.19 and 10.20), we only show the contours obtained for $\Omega_m - Amp$ once we have marginalized σ_v and β with the contours obtained in the quadrupole Q(s) fitting of previous section. In table 10.2 we have annotated the marginalized 1-σ errors for the amplitude Amp and for Ω_m.

If we try to fit to larger scales, we obtain always a biased low Ω_m compared to the one we obtain in the scales before the acoustic peak, probably because the wide-angle approximation but possibly also because non-linear effects on the BAO peak and large sample errors. We have seen this effect in the simulations, where we see that the best part to obtain parameters is at intermediate-large scales. In Okumura et al. (2008) they use all the large scale range including the baryonic peak without non-linear model, and they obtain lower values for Ω_m than the recent results. In order to avoid this problem, as said before, we fit at intermediate scales.

Sample	**Amp**	$\boldsymbol{\Omega_m}$
z=0.15-0.47	1.47-1.65	0.225-0.265
z=0.15-0.34	1.45-1.62	0.230-0.275
z=0.34-0.47	1.55-1.82	0.215-0.285
z=0.15-0.30	1.45 - 1.80	0.240- 0.320
z=0.30-0.40	1.42-1.60	0.210-0.260
z=0.40-0.47	1.60-2.00	0.195-0.305

Table 10.2: Marginalized values for Amp and Ω_m to 1-σ errors for each sample in redshift

Note how the best fit values of Amp seem to change from sample to sample. This could be due to bias. The values of Ω_m agree within $1-\sigma$ for 2 degrees of freedom (dotted lines).

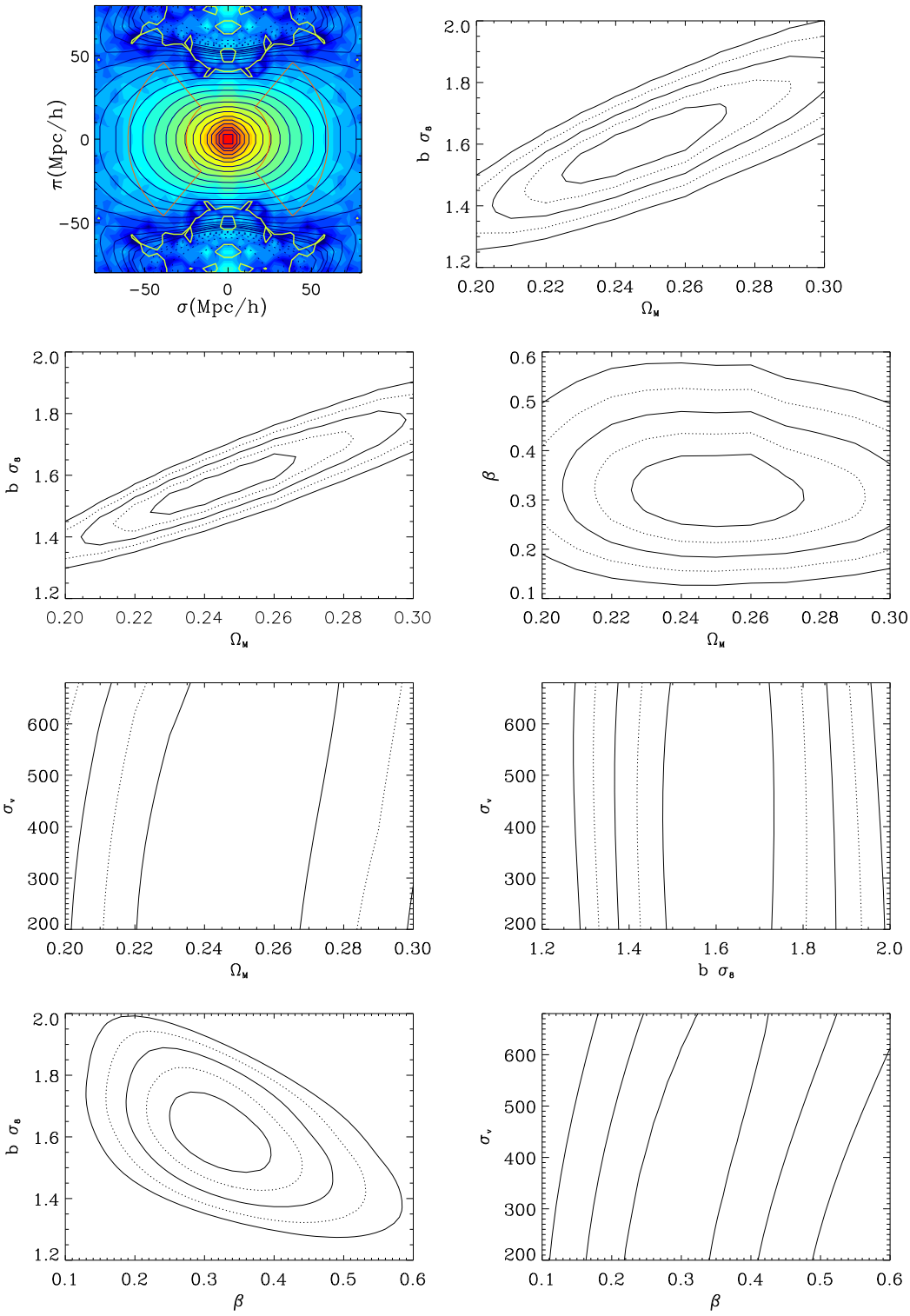

Figure 10.15: Top left panel shows $\xi(\pi, \sigma)$ for the data (as colors) and over-plotted the best fit (solid lines) obtained in the zones delimited by the orange line. Yellow contour show negative zones. We see also the contours for $\Omega_m - Amp$ marginalized for the rest of parameters, or marginalized for $\beta - \sigma_v$ from the quadrupole Q(s), and the degeneracies between the other parameters used in the fitting once we marginalize for the rest of parameters (without using the quadrupole information). Solid lines are $1-\sigma$, $2-\sigma$ and $3-\sigma$ (1 dof), and dotted lines $1-\sigma$ and $2-\sigma$ (2 dof)

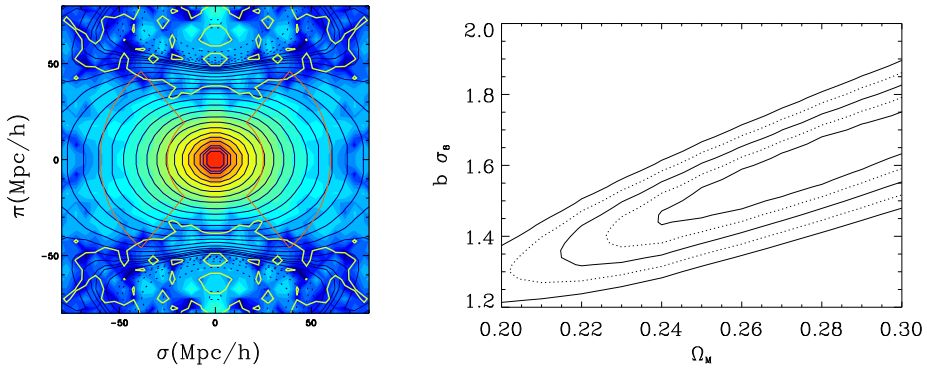

Figure 10.16: z=0.15-0.3. Best fit and contour $\Omega_m - Amp$ once marginalized for $\beta - \sigma_v$ from the quadrupole Q(s)

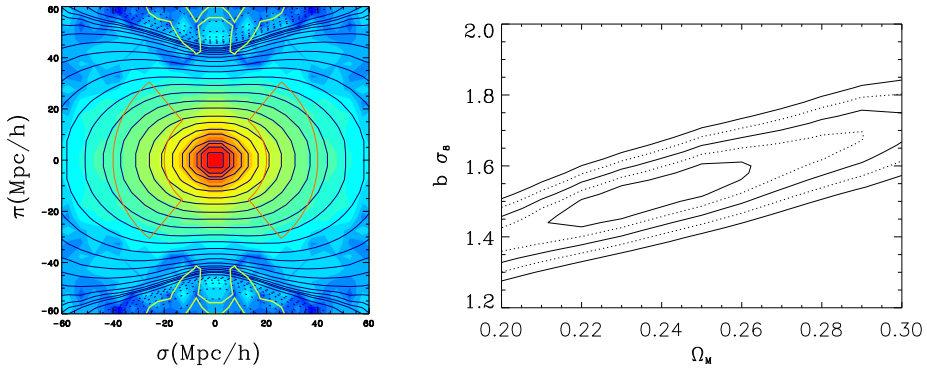

Figure 10.17: z=0.3-0.4. Best fit and contour $\Omega_m - Amp$ once marginalized for $\beta - \sigma_v$ from the quadrupole Q(s)

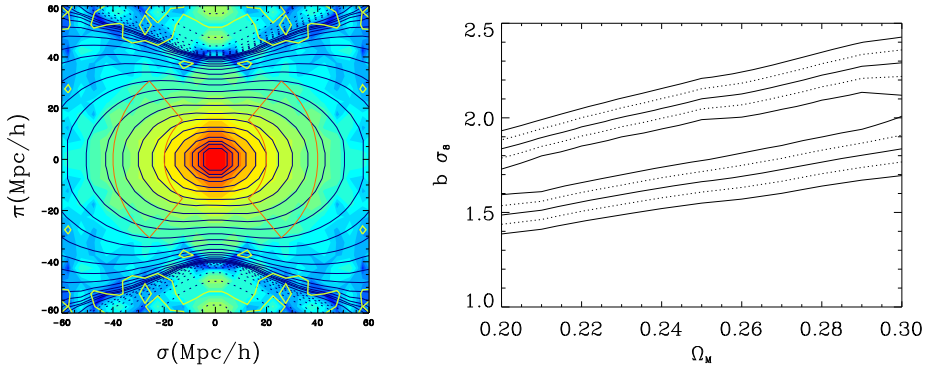

Figure 10.18: z=0.4-0.47. Best fit and contour $\Omega_m - Amp$ once marginalized for $\beta - \sigma_v$ from the quadrupole Q(s)

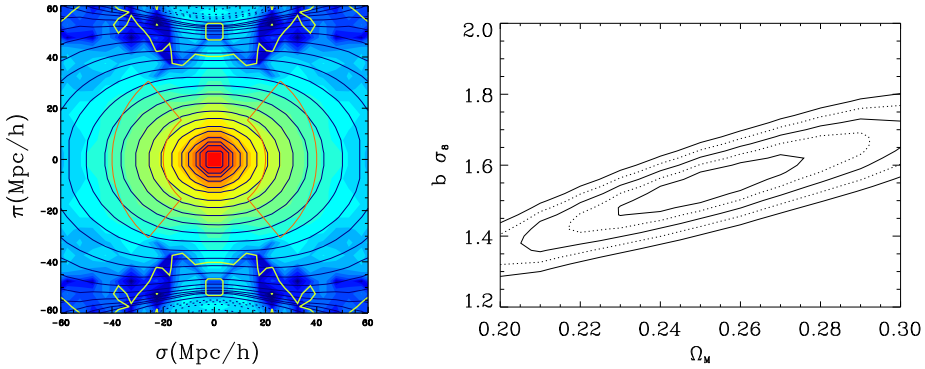

Figure 10.19: z=0.15-0.34. Best fit and contour $\Omega_m - Amp$ once marginalized for $\beta - \sigma_v$ from the quadrupole Q(s)

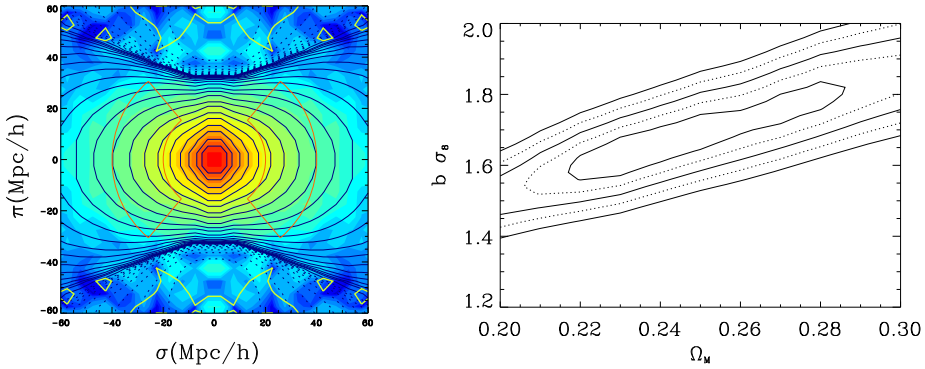

Figure 10.20: z=0.34-0.47. Best fit and contour $\Omega_m - Amp$ once marginalized for $\beta - \sigma_v$ from the quadrupole Q(s)

10.6.1 Fitting σ_8 or the modified gravity growth index γ

First, we try to obtain a fit to the parameter σ_8, which we can separate from the bias $b(z)$ because of redshift distortions, following the equation

$$\beta \equiv \frac{f(z)}{b(z)} = \frac{\Omega_m(z)^\gamma}{b(z)} \tag{10.2}$$

explained in the theoretical section (§8.1). We use the prediction $\Omega_m - Amp$ from large scales and the value of β from Q(s), with $\gamma = 0.55$ for standard gravity with high accuracy. As $Amp = \sigma_8 b(z)$, we obtain σ_8

$$\sigma_8 = \frac{\beta A}{\Omega_m(z)^{0.55}} \tag{10.3}$$

where $\Omega_m(z)$ is described in Eq.(8.28)

Here we assume a flat universe (WMAP results motivated) with a constant dark energy equation of state characterized for $w = -1$.

We marginalize for the errors we have and obtain the 1-sigma errors for σ_8 shown in Fig.10.21, on the bottom, with colors Gray: All the catalog, Red: z=0.15-0.34, z=0.34-0.47, Blue: z=0.15-0.3, z=0.3-0.4, z=0.4-0.47. There is a lower σ_8 deviation for the middle slice, but it is consistent with the others at $2-\sigma$ level. On the top of the same figure, we obtain the bias $b(z)$ from the amplitude and σ_8. The linear bias $b(z)$ is clearly higher as we move to higher redshifts, and it is consistent with previous results found also with LRG.

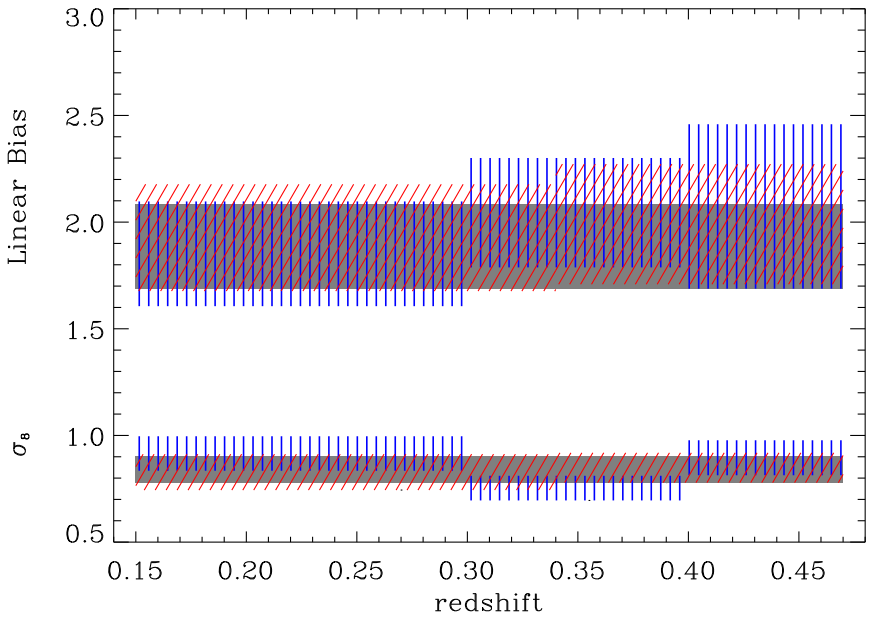

Figure 10.21: b(z) and σ_8 for each slice in redshift, which range is plotted in the figure. Gray: All the catalog, Red: z=0.15-0.34, z=0.34-0.47, Blue: z=0.15-0.3, z=0.3-0.4, z=0.4-0.47

We could also assume a value for σ_8 which is also known from other observations, such as WMAP, and assume that the observations can be explained by changes in the law of gravity at cosmological scales (Linder 2005). This can be represented by the growth index γ. Both

$f(z)$ and the growth factor $D(z)$ changes with γ. We have plotted the change of f and D with γ in Fig.10.22 for z=0.34 (mean redshift in LRG) and $\Omega_m = 0.25$. From observations, we have measured $\sigma_8 b(z)D(z)$, if we now fix σ_8 we can have an estimation of $b(z)D(z)$ as well as our estimation of β. We therefore can use this to calculate the product $f(z)D(z)$ directly from the combination $\beta(b(z)D(z))$, see Eq.(10.2).

We have assumed that the change comes from a different γ and not from a different equation of state for dark energy. This is a good approximation because w only depends slightly on γ (Linder 2007). We show in Fig.10.23 our estimation of $1-\sigma$ errors for the growth index γ once we fix σ_8=0.7, 0.8, 0.9 . As shown in Fig.10.22, the product $f(\gamma)D(\gamma)$, at a given redshift, decreases with γ. If we change the value σ_8 to higher, the factor $\beta\, b(z_{slice})\, D(z_{slice})$ obtained from observations will be lower, and we will arrange the difference by reducing $f\, D$, so increasing γ. In §13.7 we will see as the argument goes in the opposite way when we work with ISW effect. At $2-\sigma$ and for all the redshift slices, γ is consistent with a standard gravity, except for $\sigma_8 = 0.7$ where we need $3-\sigma$ for the last slice, favoring a σ_8 clearly higher than 0.7, which is in agree with recent observations.

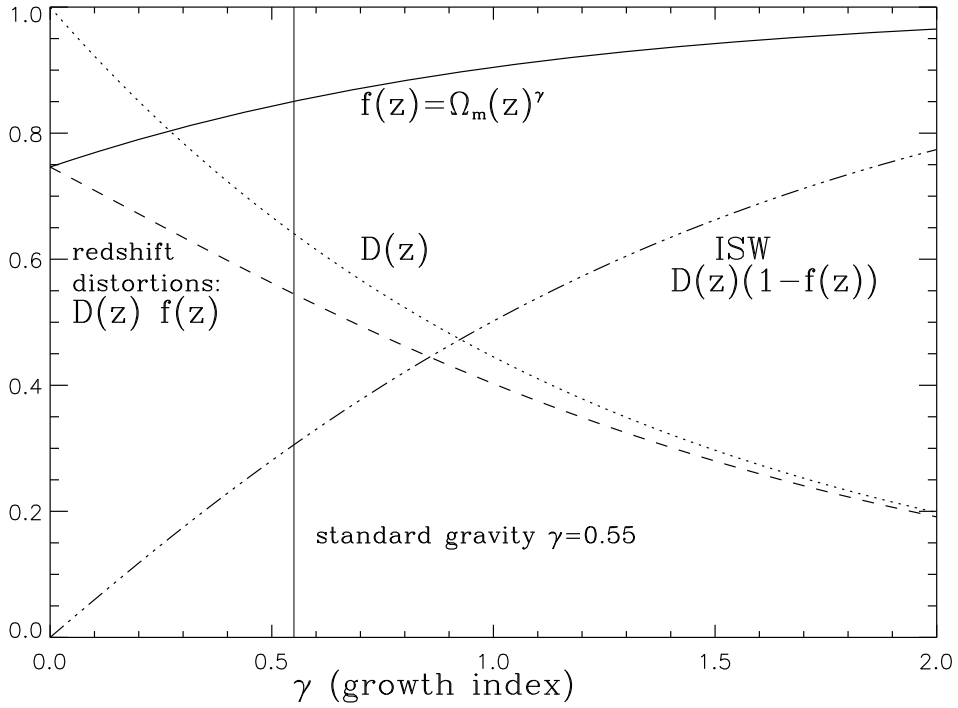

Figure 10.22: We see here the change of f and D with γ and the factors involved in redshift distortions and ISW effect. We have fixed $\Omega_m = 0.25$ and $z = 0.34$

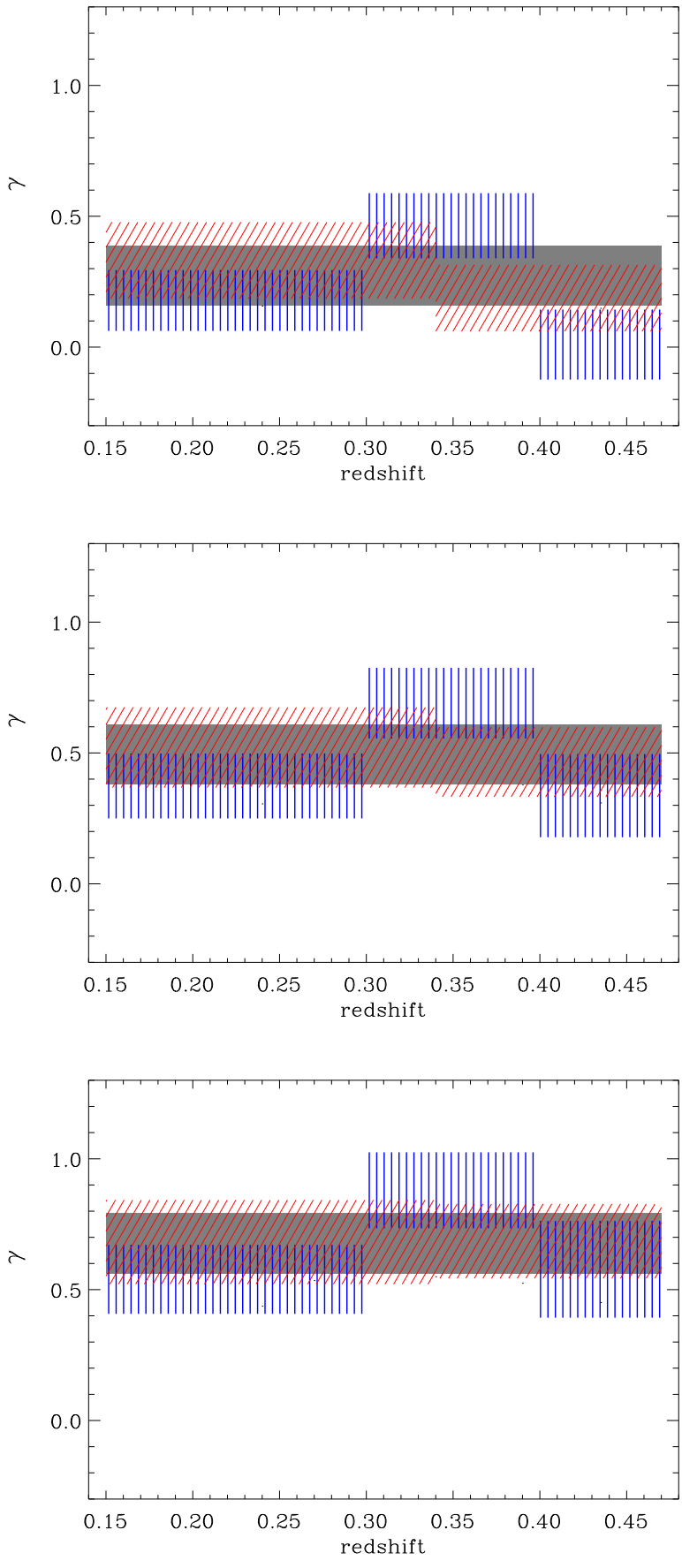

Figure 10.23: Growth index γ for different redshift slices as in Fig.10.21 when we fix $\sigma_8 = 0.7, 0.8, 0.9$

10.7 Fitting to small scales and non-linear bias

When we move to small scales, we find the following problems. First of all, the bias becomes clearly dependent on scale for distances smaller than 10-20Mpc/h, because LRG are galaxies highly biased so they only keep the linear bias constant at large scales. Secondly, the model that we are using is supposing that the pairwise velocity dispersion is independent of scale, which is not a good approximation for small scales as we have seen in the simulations.

In Fig.10.24 we see the projected correlation function $\Xi(\sigma)$ calculated using Eq.(8.19) on the top panel, and at the bottom panel we have plotted $\Xi(\sigma)/\sigma$ which as seen in Eq.(8.21) should be a power law in the case that the real space correlation function is also a power law. In Fig.10.25 we show the resulting real-space correlation function which we have calculated using Eq.(8.23) (in blue) and over-plotted the monopole in redshift space (in orange). At intermediate scales, from 5 to 30 Mpc/h (the top value limited by the method to obtain $\xi(r)$), $\xi(s)$ is equal to $\xi(r)$ but biased by a constant factor, as in Eq.(8.24), due to Kaiser effect. We see this constant bias at intermediate scales in Fig.10.26, where we divide the correlation function in redshift space and real space $\xi(s)/\xi(r)$, and we can associate it to a function of β (solid line shows $\beta = 0.34$, the best value for the redshift slice z=0.15-0.47). The agreement is excellent, which provides a good consistency check for our results. Note that we prefer to obtain β from the quadrupole, which seems to be more stable at large scales. The difference between the real and redshift space correlation function for small scales is primordially due to the random peculiar velocities.

First, we fit the obtained real space correlation function to a power law, $\xi(r) = (r/r_0)^{-\gamma_0}$, from 1Mpc/h to 15Mpc/h. At scales smaller than 1Mpc/h the fit is bad, it is no longer a power law. In Fig.10.27 we see the contour plot for $1-\sigma$, $2-\sigma$ and $3-\sigma$ (for 1 and 2 degrees of freedom, dotted and solid) and in Fig.10.28 we see the real space correlation function, the best model (red) for the power law and the dark matter correlation function obtained from best parameters in §10.6 which is corrected for a linear bias. Large scale and small scale fittings agree as we can see in the plot, and the correlation function does not follow a power law for distances smaller than $\backsim$ 1Mpc/h, where we can see the transition from the one-halo to the two-halo term.

Zehavi et al. 2005 did a similar analysis with a previous SDSS spectroscopic data release (35000 LRGs) at intermediate scales from 0.3 to 40Mpc/h. We have doubled the number of LRGs and our results agree with them for the monopole, the projected correlation function, and the obtained real-space correlation function, with the same main conclusions. Also Eisenstein et al. (2005a), in a study of small scales (0.2-7Mpc/h) using the cross-correlation between spectroscopic LRG with the main photometric sample, remark that $\xi(r)$ can not be explained with a power-law fitting. However, Masjedi et al. (2006) have obtained the correlation function at very small scales (0.01-8Mpc/h) and have found that, although with some features diverging from a power law, all the range is really close to a $\xi(r)^{-2}$.

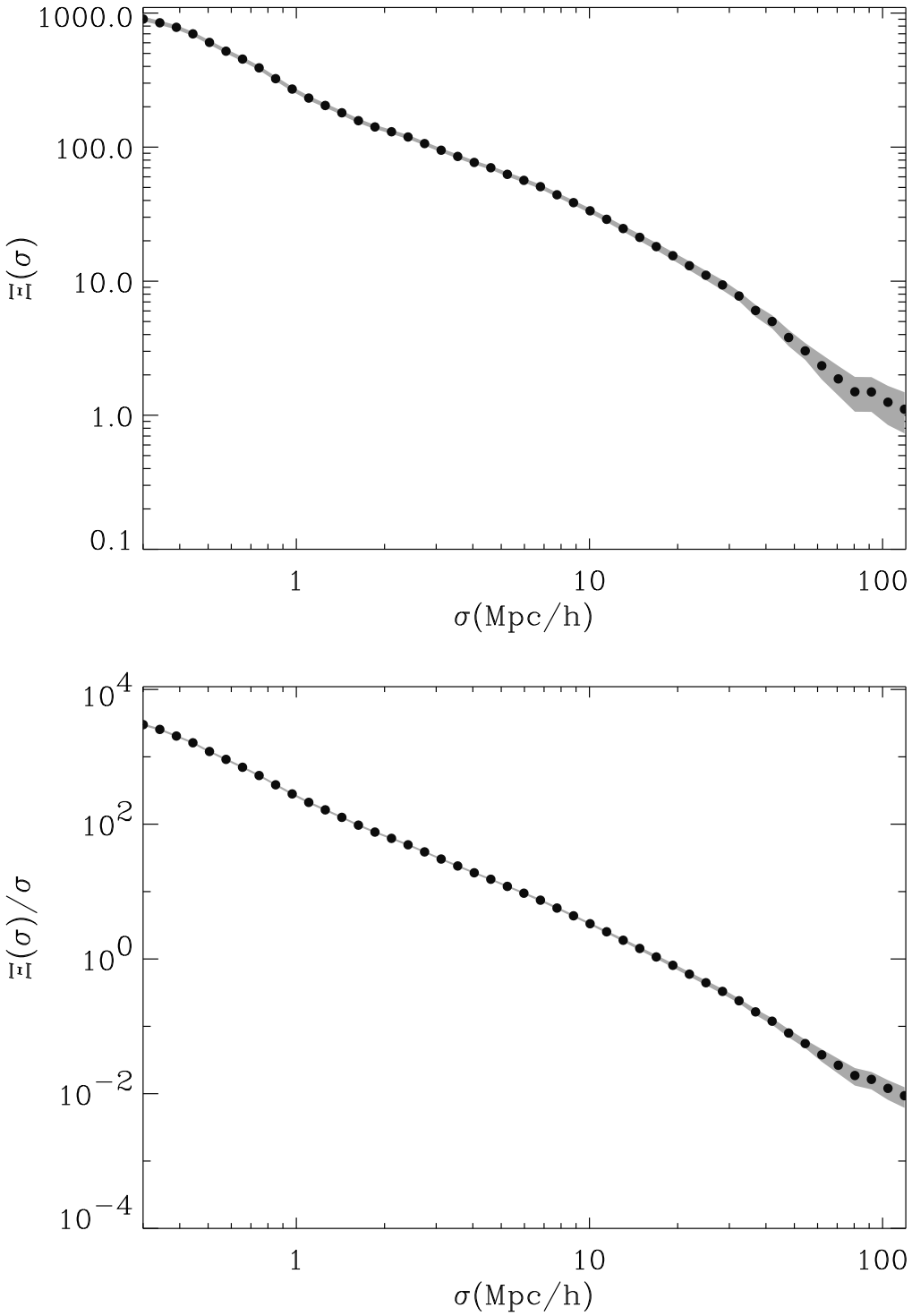

Figure 10.24: $\Xi(r)$, $\Xi(r)/r$

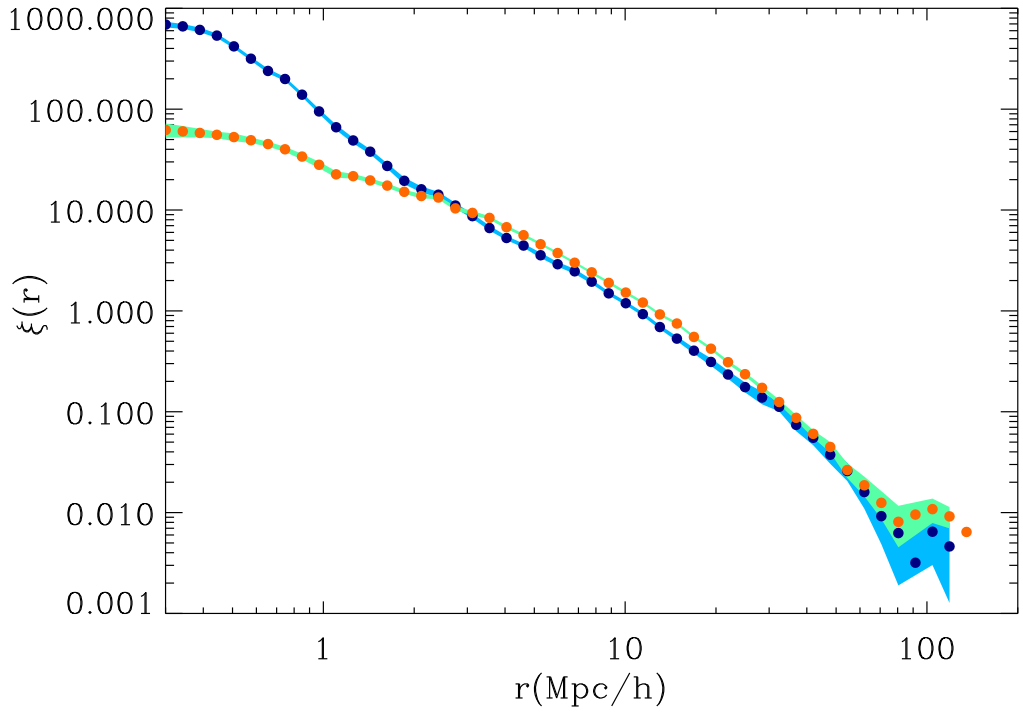

Figure 10.25: $\xi(r)$ (blue dots) and $\xi(s)$ (orange dots)

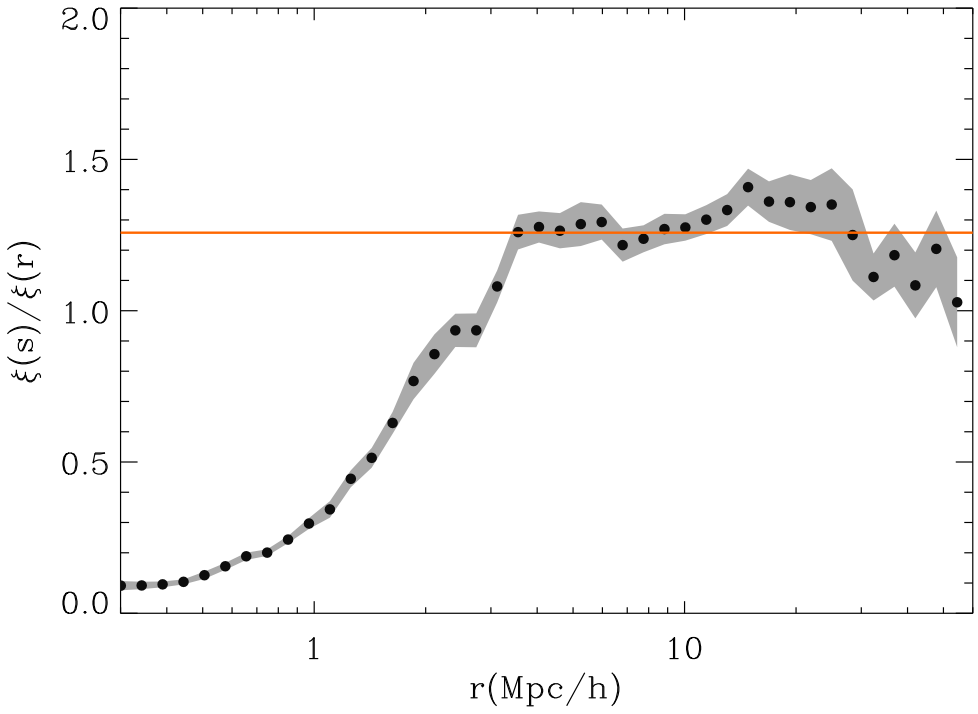

Figure 10.26: $\xi(s)/\xi(r)$

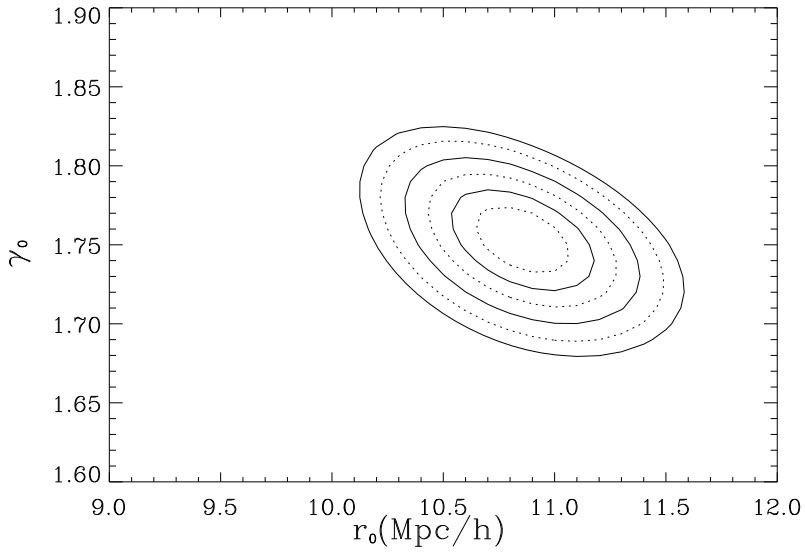

Figure 10.27: Best fit of $\xi(r)$ to a power law model $\xi(r) = (r/r_0)^{-\gamma_0}$, 1-15Mpc/h

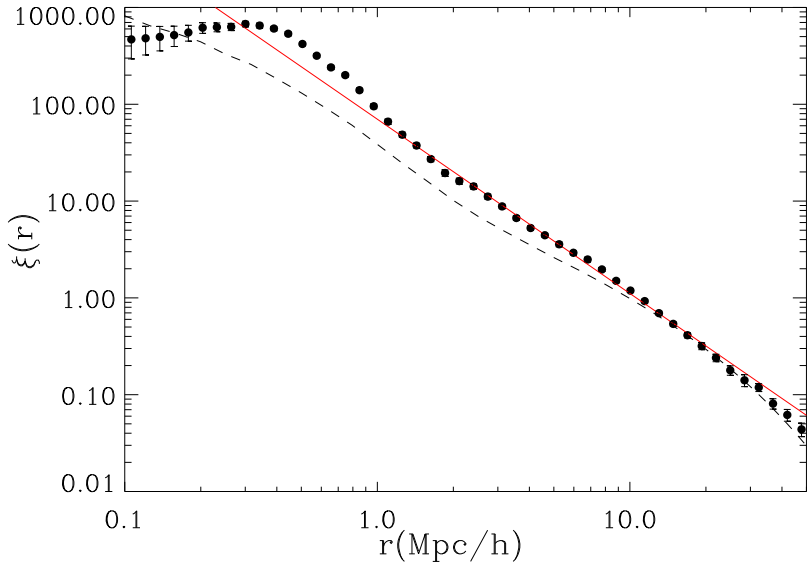

Figure 10.28: Observed $\xi(r)$ (dots), best fit to the power law $\xi(r) = (r/r_0)^{-\gamma_0}$ (red), and dashed over-plotted the best real space correlation function for large scales, assuming a constant bias

We know from simulations with halos that the non-linear bias typically follows a power-law, which has a different slope γ_b depending on the halo mass of the particles studied, and many other parameters concerning galaxy formation. LRG are assumed to be red galaxies that trace halos of $10^{13} M_\odot$, but there is a wide range of halos masses, and the non-linear bias shows us these properties. We define the bias as

$$b(r) = \sqrt{\xi(r)/\xi(r)_{DM}} = b\, b_{nl}(r) \tag{10.4}$$

where the dependence on scale of the bias is represented by $b_{nl}(r)$, and the linear constant

bias as b. $b_{nl}(r)$ shows the relation between the LRG real space correlation function to the dark matter once corrected by just linear bias. When $b_{nl}(r)$ is equal to 1, it means that the bias is linear from there, so we define a parameter r_b for the power law which shows the scale from which non-linearity begins to be important. r_b coincides approximately with the correlation length, where the real space correlation function is 1. To compute the non-linear bias we need the dark matter correlation function and the linear bias, which we have taken from the fitting at large scales. We have calculated the bias for all the Ω_m and amplitudes. Then we marginalize over them. In Fig.10.29 we see the contours for r_b and γ_b (left panel), and the best fit (red in the right panel). This fit to the bias can explain the differences seen previously between the correlation function and a power law for scales smaller than 1Mpc/h. At scales smaller than 0.3Mpc/h, the real space correlation function turns down probably due to fiber collisions. In detail, we see in Fig.10.29 a feature in the bias between 1 and 2 Mpc/h, indicating that LRGs galaxies do not trace the halo model in a scale dependent bias completely smooth. We have tried to change σ_8, fixed for this analysis at $\sigma_8 = 0.8$, and we observe that we could see this feature if the true σ_8, imprinted in the galaxies, is lower than the assumed value 0.8, but the characteristic shape would be located at 1Mpc/h and no higher. Moreover, we have found that σ_8 tends to be slightly higher than σ_8 in the previous section, which goes in the opposite direction. We think that it is difficult to obtain σ_8 in this range, and that this feature is due to the range of halo sizes of our LRGs, which makes it difficult to predict exactly the transition point from the 1-halo to the 2-halo term (see Gaztañaga & Juszkiewicz 2001). If galaxies are residing within dark matter halos then the clustering of the galaxies on scales larger than halos is determined by the clustering of the dark matter halos that host them, plus statistics of the occupation of halos by galaxies. For larger scales than $\backsim$ 2Mpc/h (the biggest halos), the clustering comes entirely from LRGs that reside in different halos, while for smaller scales, the clustering can come from galaxies in different halos or galaxies in the same halo until it is reached a minimum size of halos (see Masjedi et al. (2007) for a more detailed explanation).

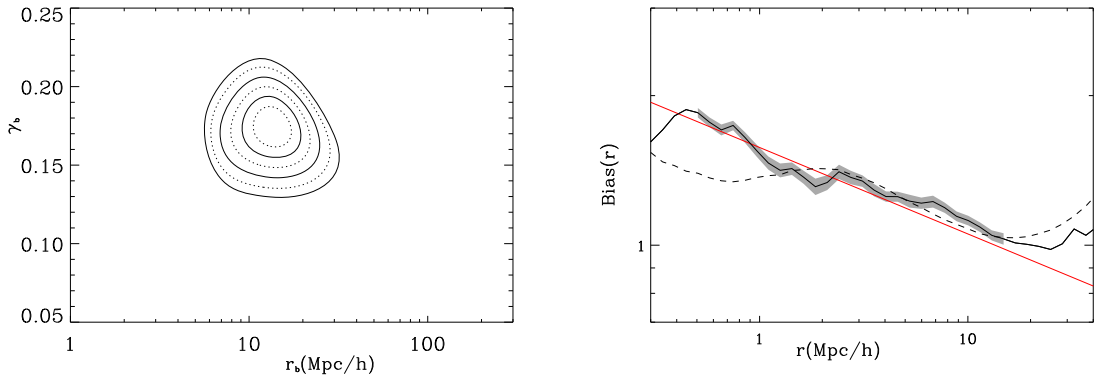

Figure 10.29: Left panel: Best fit to no linear bias $b_{nl}(r)$ (defined in the text) with a power law $b_{nl}(r) = (r/r_b)^{-\gamma_b}$. Right panel: No linear bias $b_{nl}(r)$ (solid line with errors in gray) and best power law fit (red). We have also over-plotted in dashed line the bias obtained if we suppose that the galaxy correlation function is a power law

10.7.1 Measurement of σ_v as a function of scale

Once we have obtained the real space correlation function, we look at the monopole $\xi(s)$, the quadrupole $\xi_2(s)$ and also at $\xi(\pi, \sigma)$ in order to check the result. We see in Fig.10.30 the

monopole $\xi(s)$ (top panel) and quadrupole $\xi_2(s)$ (bottom panel) binning the distance with 0.2Mpc/h, and over-plotted in red the theoretical model, which we have found integrating $\xi(\pi, \sigma)$. We have used the method of Hamilton (Eq.(8.14)) which gives a shape for $\xi(\pi, \sigma)$ given a real-space correlation function and the parameters obtained in the previous sections. The monopole does not coincide with the model for scales smaller than 3Mpc/h, neither does the quadrupole; this difference indicates that σ_v is higher at smaller scales as shown in Fig.9.22 for the simulations.

We use $\xi(s)$ to fit a value for σ_v at each distance and we use the same pairwise velocities to check for consistency the discrepancy found in $\xi_2(s)$ (bottom panel in Fig.10.30).

We have tested this method in the simulations. In Fig.9.22 we can see the dispersion in the LOS pairwise velocity for all the range of distances. We plot in Fig.10.33 the monopole of the simulation (solid) and different models (dotted) with different σ_v, growing down. The idea is that we can not distinguish between different σ_v at large scales, from 5Mpc/h to 10Mpc/h the monopole follows a line of constant σ_v near 400 km/s, and for smaller scales, the monopole cross different lines of constant σ_v. This is the range of σ_v dependent on the scale. The dispersion σ_v at such small scales changes with the real distance, not with the redshift distance s which we are analyzing in the monopole. The result in a fixed distance in redshift space is a convolution of the signal at different real distances, with different σ_v, so we are approximating the result when we obtain the real σ_v from the monopole. Nevertheless, we see in simulations that the change that we observe in the monopole gives an estimation of σ_v for the real scale $r = s$ because we recover the expected values of σ_v.

These errors we have plotted are correlated with the same covariance that we used in the monopole (Fig.10.31). As seen in §10.1, Slosar et al. (2006) show that pairwise velocity distribution in real space is a complicated mixture of host-satellite, satellite-satellite and two-halo pairs. The peak value is reached at around 1Mpc/h and does not reflect the velocity dispersion of a typical halo hosting these galaxies, but is instead dominated by the sat-sat pairs in high-mass clusters. Tinker et al. (2007) uses the HOD model to explain that at r $\backsim$ 2 Mpc/h, the PVD rapidly increases as satellite-satellite pairs from massive halos dominate. At r $<$ 1 Mpc/h, the pairwise velocities dispersion decreases with smaller separation because central-satellite pairs become more common. These predictions agree well with our results.

The effect in the quadrupole Q(s) is not significant at the scales where we obtain the contour $\beta - \sigma_v$, where we assume that σ_v does not change, although it explains the difference we see at small scales.

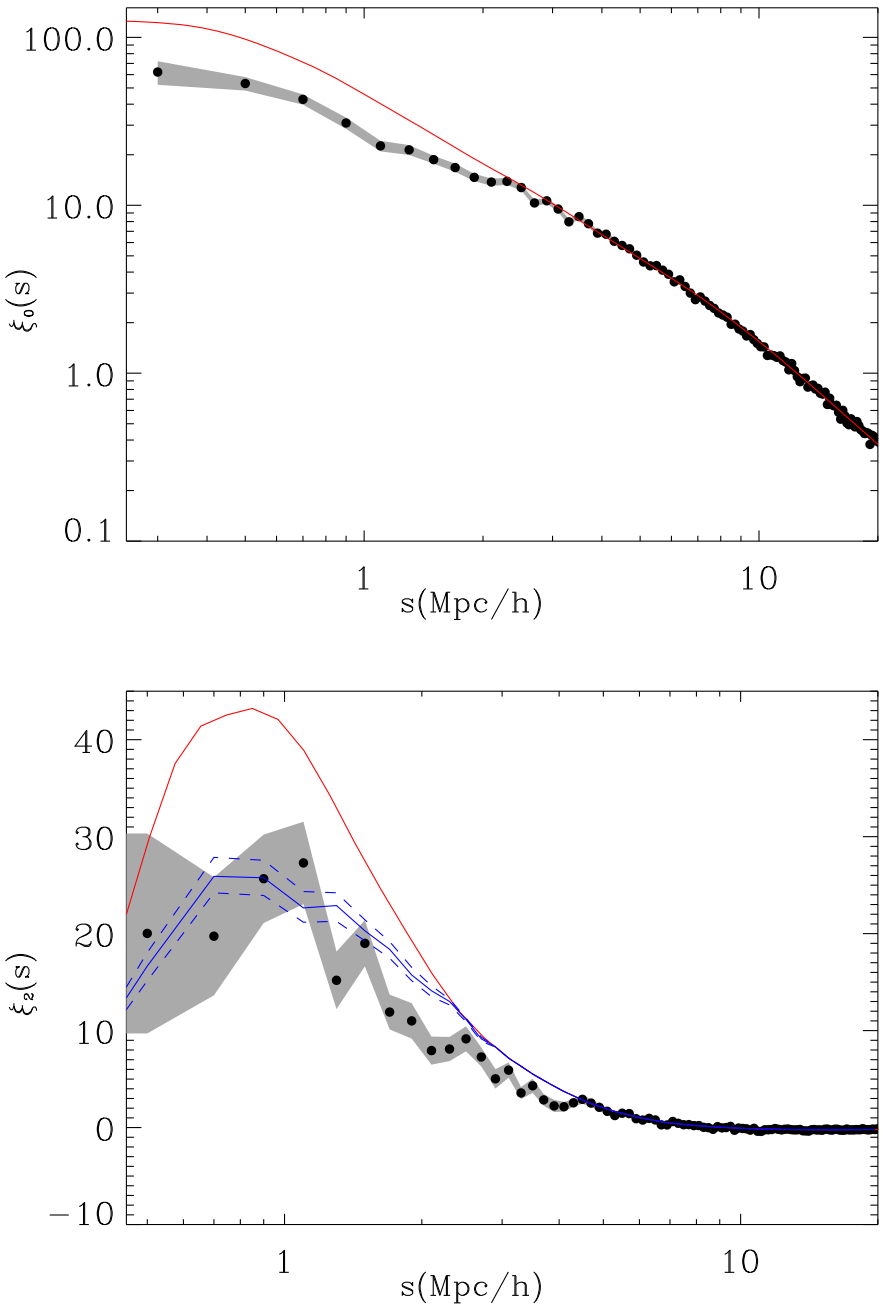

Figure 10.30: Monopole $\xi(s)$ (dots) with errors (gray) and best model assuming a constant σ_v (red). Bottom panel: Quadrupole $\xi_2(s)$ (dots) with errors (gray), best model assuming a constant σ_v (red) and model assuming variation in σ_v with scale (blue) derived from the monopole $\xi(s)$ in the top panel (see Fig.10.31)

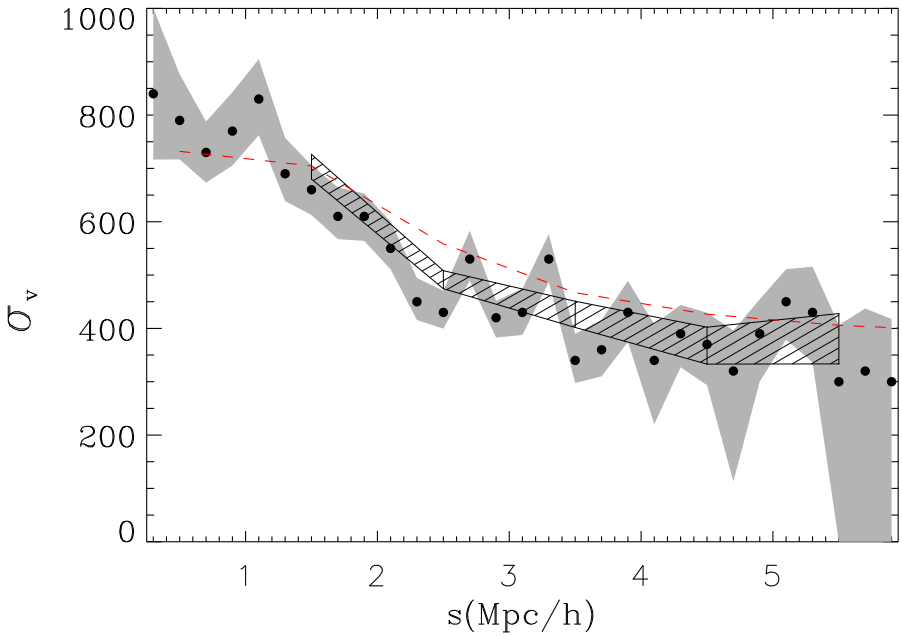

Figure 10.31: σ_v vs distance, calculated directly from the monopole

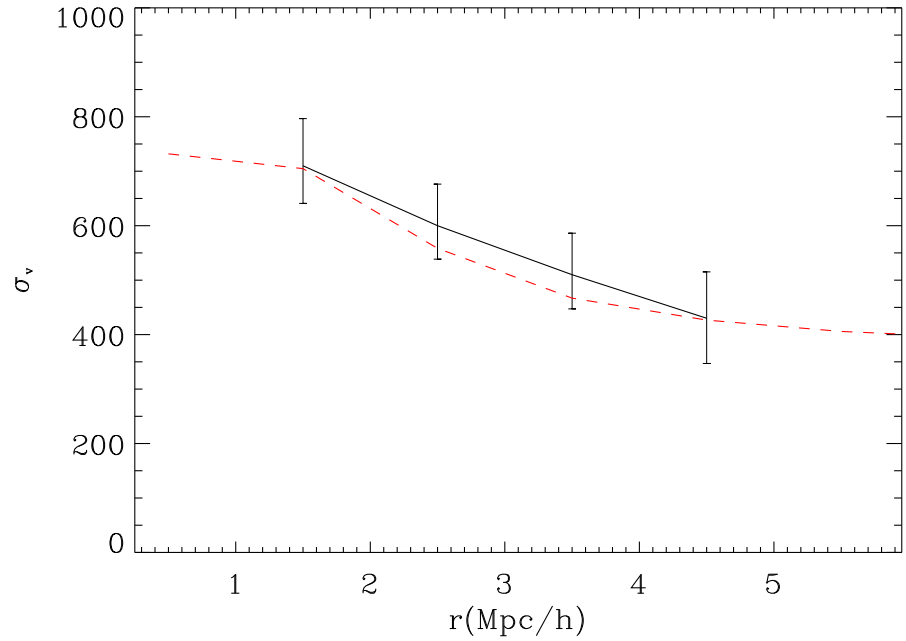

Figure 10.32: Dispersion calculated from monopole in simulations (solid) compared to the calculated directly from velocity field in simulations (dashed)

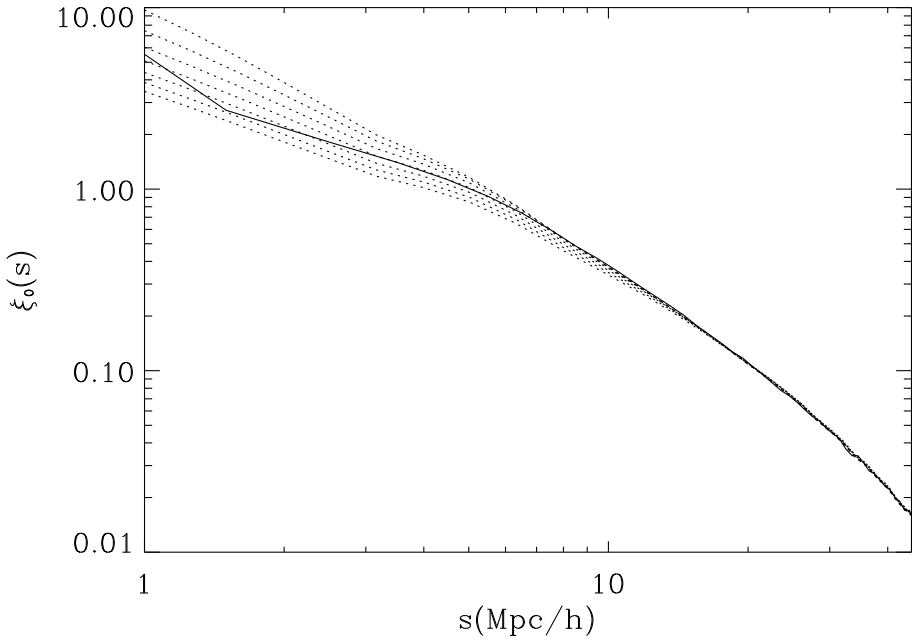

Figure 10.33: Monopole in the simulations (solid) and different models with MICE cosmology changing the random pairwise velocity dispersion σ_v (dotted)

10.7.2 Consistency of $\sigma - \pi$ model with data

Now we look directly at $\xi(\pi, \sigma)$ at small scales once we have all the parameters, to see if the model works when we separate π and σ, for all the angles. We have used a binning of 0.2Mpc/h for these plots, in order to see clearly the fingers of God, which are concentrated at very small σ. First, we can see the detailed plot of $\xi(\pi, \sigma)$ in Fig.10.34.

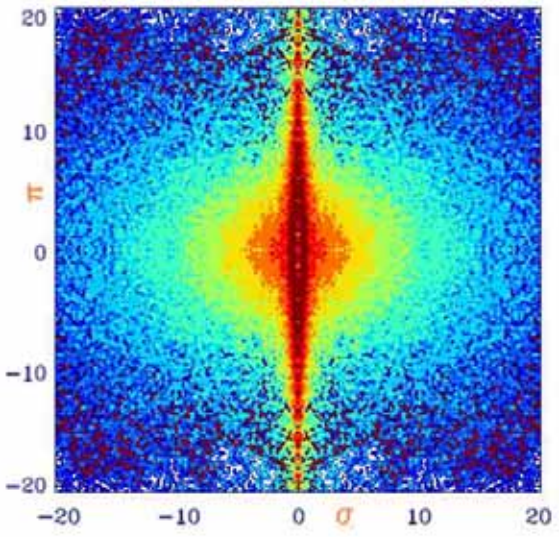

Figure 10.34: $\xi(\pi, \sigma)$ calculated using squares in $\pi - \sigma$ of side=0.2Mpc. Contours are: 0.1-50 with logarithm separation=0.6

In the next three figures 10.35, 10.36 and 10.37, we can see the differences between the data and the model in three cases. Top panels from left to right show: the data as colors; the data and the model over-plotted as solid line; and the model as colors. Bottom panels show: the same as in the top but we have zoomed the σ direction to see clearly the fingers of God. First (Fig.10.35), we compare the data with a model that assumes linear bias (found fitting large scales) and a constant pairwise velocity dispersion of σ_v (obtained from the quadrupole Q(s)). We see clearly that it does not fit, basically because the bias becomes non-linear. Part of the apparent fingers of God are corrected just adding the non-linear bias in the model. In the second model (Fig.10.36), we compare the model that we obtained using the real space correlation function just found, which includes all the non-linear effects. We still need to explain the strong elongation we see in the direction line-of-sight, which we correct with the third model (Fig.10.37). We include the variation in σ_v assuming that σ_v is constant along the line-of-sight for a fixed σ (perpendicular distance). In reality, different real scales, each with its associated σ_v, can affect the same redshift space scale s, but it has been found in previous studies that this is a good approximation, as we see in the figures.

It is difficult to model $\xi(\pi, \sigma)$ if σ_v is dependent on scale, but we have seen that the change in σ_v only affects small s (less than 4Mpc/h) and small perpendicular σ. For the rest of values of π and σ, we can explain the observed $\xi(\pi, \sigma)$ just by a β and an effective σ_v, which in reality does not change a lot on real scales bigger than $4Mpc/h$. Figures 10.38, 10.39, 10.40, 10.41 and 10.42 show the best third model, for different redshift slices. All the cases agree well with observations.

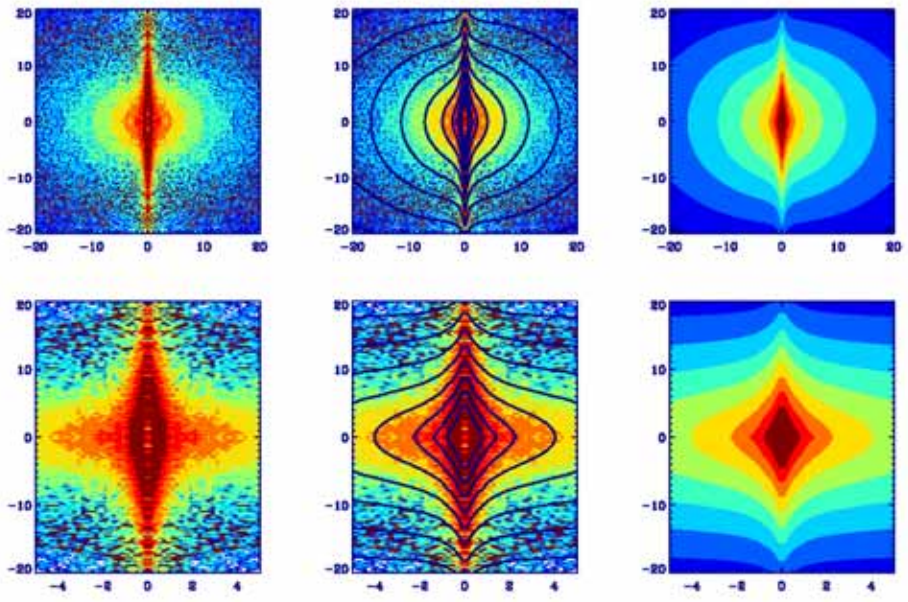

Figure 10.35: $\xi(\pi, \sigma)$ (z=0.15-0.47) modeled with a linear bias in the real-space correlation function. Top:data, data+model, model . Bottom: the same zoomed in σ

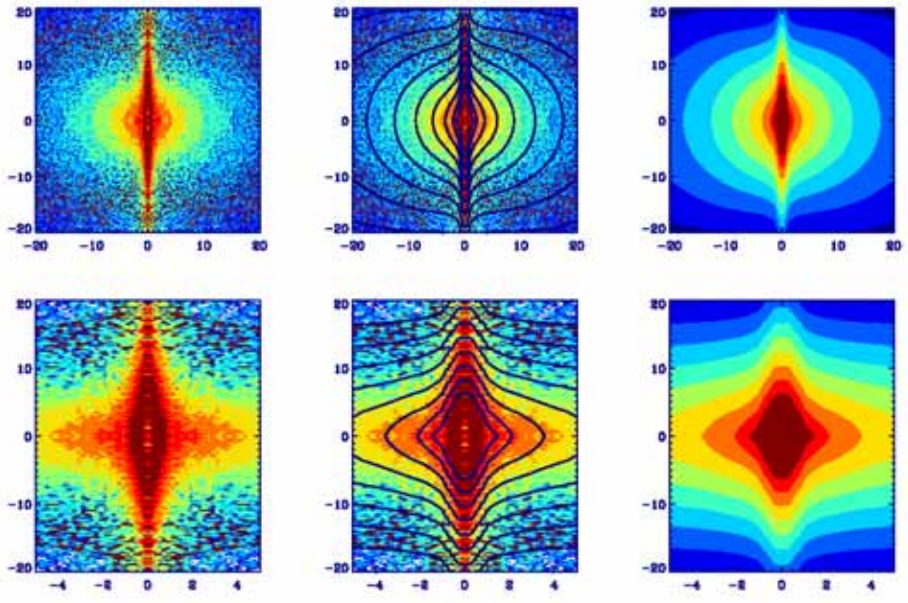

Figure 10.36: $\xi(\pi, \sigma)$ (z=0.15-0.47) modeled with real-space correlation function obtained from deprojection. Top:data, data+model, model . Bottom: the same zoomed

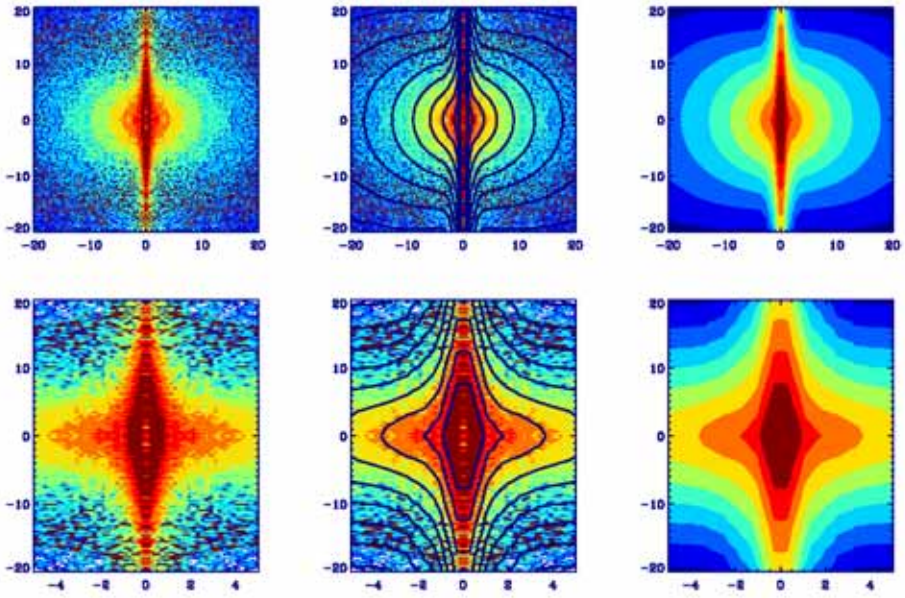

Figure 10.37: $\xi(\pi,\sigma)$ (z=0.15-0.47) modeled with real-space correlation function obtained from deprojection and σ_v dependent on scale. Top:data, data+model, model . Bottom: the same zoomed

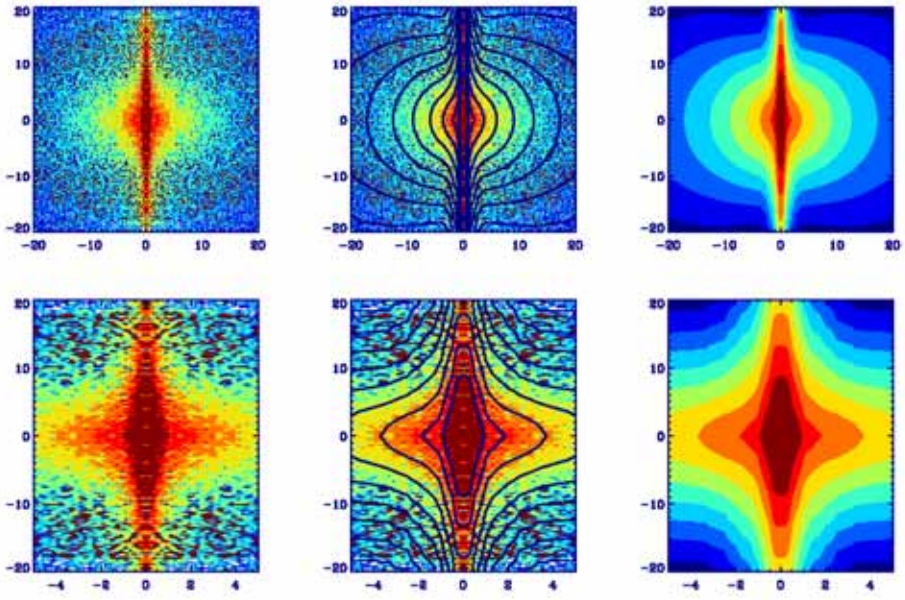

Figure 10.38: $\xi(\pi,\sigma)$ (z=0.15-0.3) modeled with real-space correlation function obtained from deprojection and σ_v dependent on scale. Top:data, data+model, model . Bottom: the same zoomed

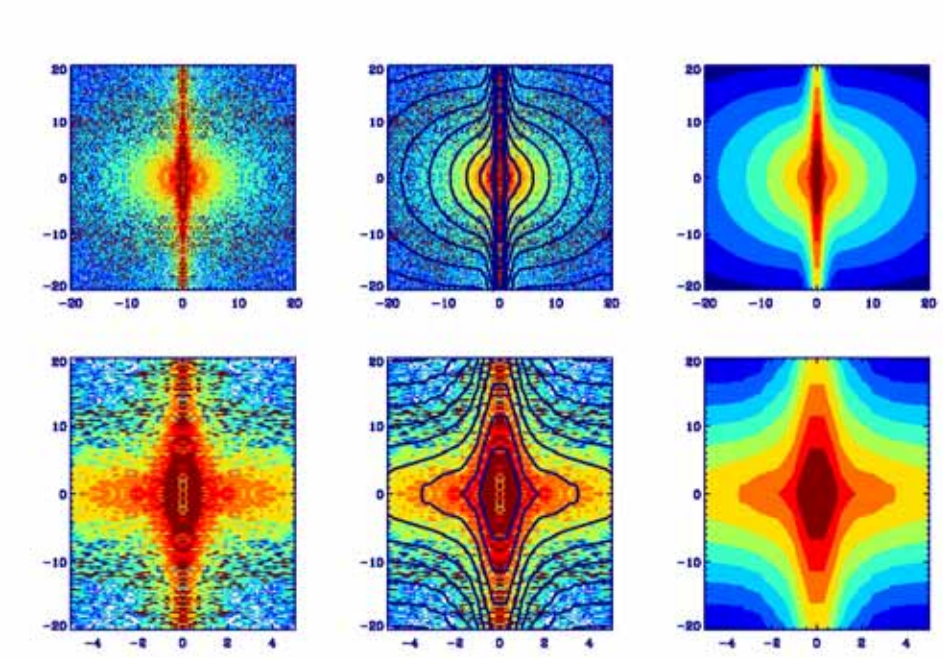

Figure 10.39: $\xi(\pi, \sigma)$ (z=0.3-0.4) modeled with real-space correlation function obtained from deprojection and σ_v dependent on scale. Top:data, data+model, model . Bottom: the same zoomed

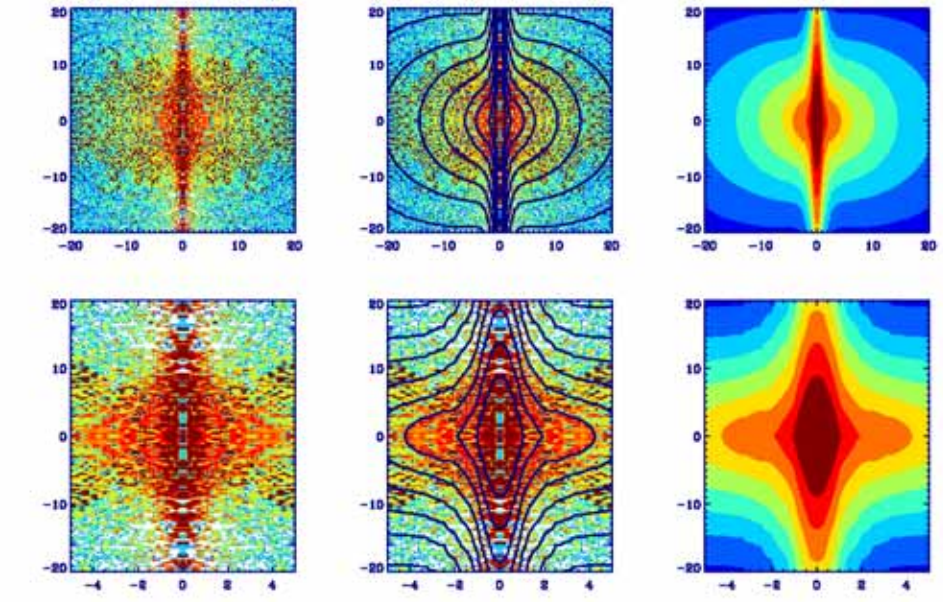

Figure 10.40: $\xi(\pi, \sigma)$ (z=0.4-0.47) modeled with real-space correlation function obtained from deprojection and σ_v dependent on scale. Top:data, data+model, model . Bottom: the same zoomed

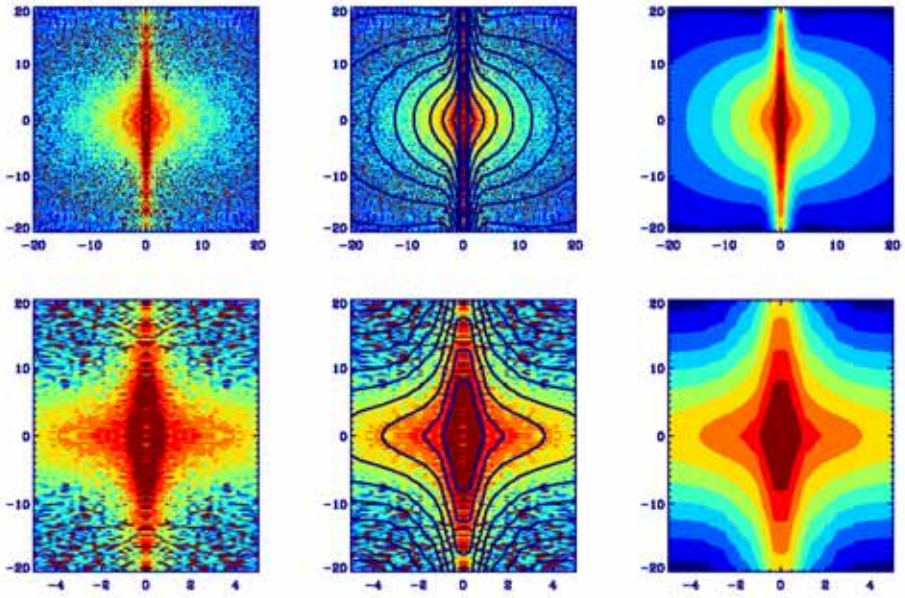

Figure 10.41: $\xi(\pi,\sigma)$ (z=0.15-0.34) modeled with real-space correlation function obtained from deprojection and σ_v dependent on scale. Top:data, data+model, model . Bottom: the same zoomed

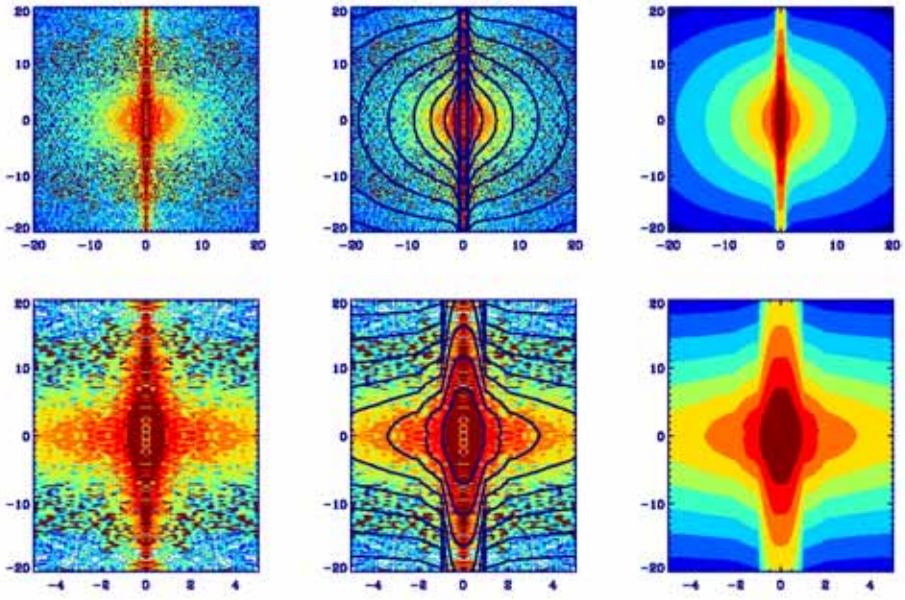

Figure 10.42: $\xi(\pi,\sigma)$ (z=0.34-0.47) modeled with real-space correlation function obtained from deprojection and σ_v dependent on scale. Top:data, data+model, model . Bottom: the same zoomed

10.8 Different redshift slices

We look at the differences between the redshift slices in the monopole (Fig.10.43), in the monopole BAO scale (Fig.10.44), in the projected correlation function $\Xi(\sigma)$ (Fig.10.45), in the real-space correlation function $\xi(r)$ (Fig.10.46) and in the ratio $\xi(s)/\xi(r)$ (Fig.10.48).

As we have seen in section 10.5, β is similar for all the redshift slices, and we can also see that in Fig.10.48, which at large scales also is a function of β (Eq.(8.24)). The turn down at large scales is due to $\xi(r)$ which is dividing and it is not well calculated for scales larger than 30Mpc/h (it is overestimated). Thus, the monopole is approximately a measure of the real-space correlation function for large scales, but biased by a function of β similar for all the slices. Looking at the monopole (Fig.10.43), also at the projected correlation function (Fig.10.45) and at the real-space correlation function (Fig.10.46) we see that all the slices except from the further one (blue dash-dot) lay in the same line, meaning that $D(z)b(z)$ is almost constant with redshift, what is called stable clustering. We see the baryon peak in detail in the monopole $\xi(s)$ (Fig.10.44), which is consistent with the first detection of the same peak in LRG (Eisenstein et al. 2005b). The peak is biased for slices further away. On bottom panel we have over-plotted the best lineal fit (Eisenstein & Hu 1998) which is lower than measurements probably due to sampling variance. We study the peak with more detail in §10.10.

In Fig.10.46 we also see that the change of the slope at small scales moves to larger scales as we explore further slices, we think that it is due to geometry since it is the same angular scale. We have also plotted the bias $b(z)$ for all the slices (Eq.(10.4)). It is clear that $b(z)D(z)$ are nearly constant, thus $b(z)$ grows with redshift as we see in Fig.10.47. The slope in the non-linear bias is nearly the same, so the small scale interaction between galaxies is nearly the same, as expected.

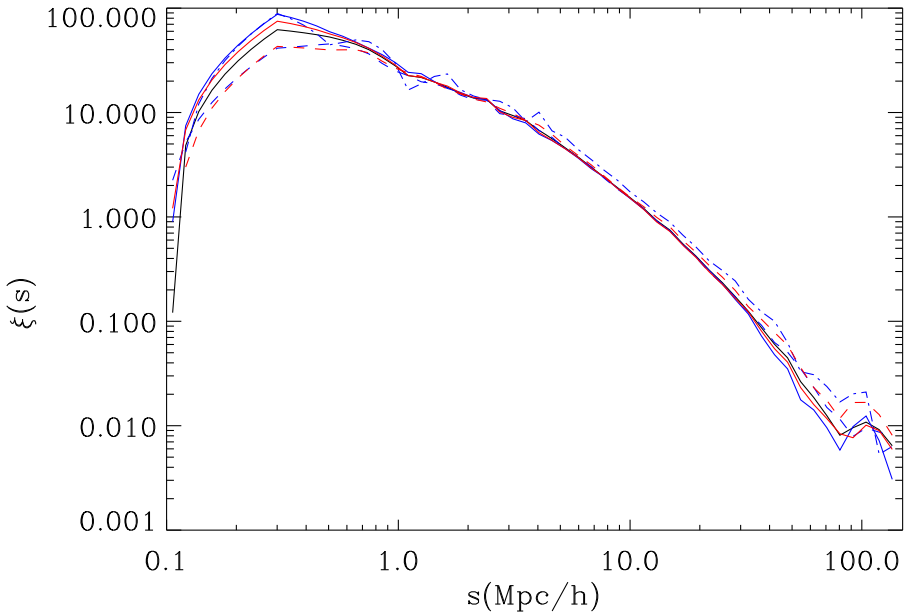

Figure 10.43: Comparison between $\xi(s)$ in redshift space for different slices in redshift. All: black, z=0.15-0.3 (solid blue), z=0.3-0.4 (dashed blue), z=0.4-0.47 (dashed-dotted blue); z=0.15-0.34 (solid red), z=0.34-0.47 (dashed red)

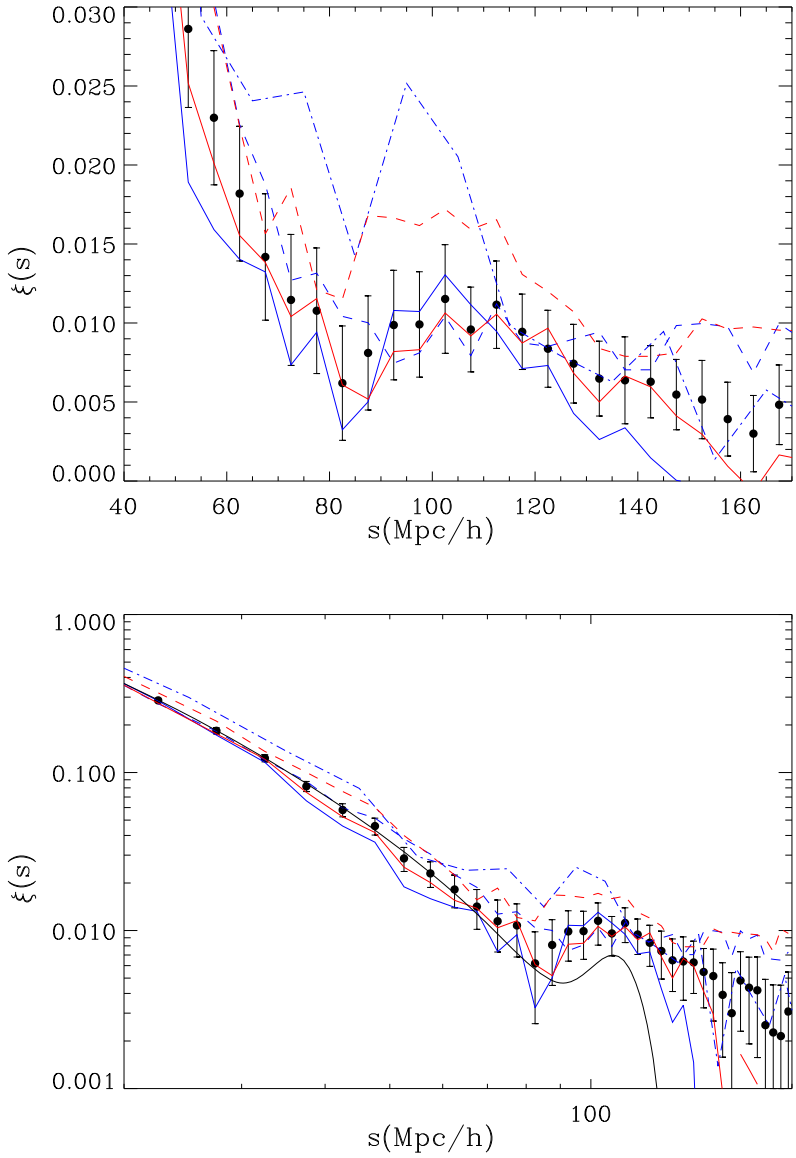

Figure 10.44: Comparison between the BAO peak in $\xi(s)$ for different slices in redshift. All: black dots with errors, z=0.15-0.3 (solid blue), z=0.3-0.4 (dashed blue), z=0.4-0.47 (dashed-dotted blue); z=0.15-0.34 (solid red), z=0.34-0.47 (dashed red). Top: Detail of the BAO peak in $\xi(s)$. Bottom: Large scales for $\xi(s)$ compared to the best fit linear model for the principal redshift slice (solid line)

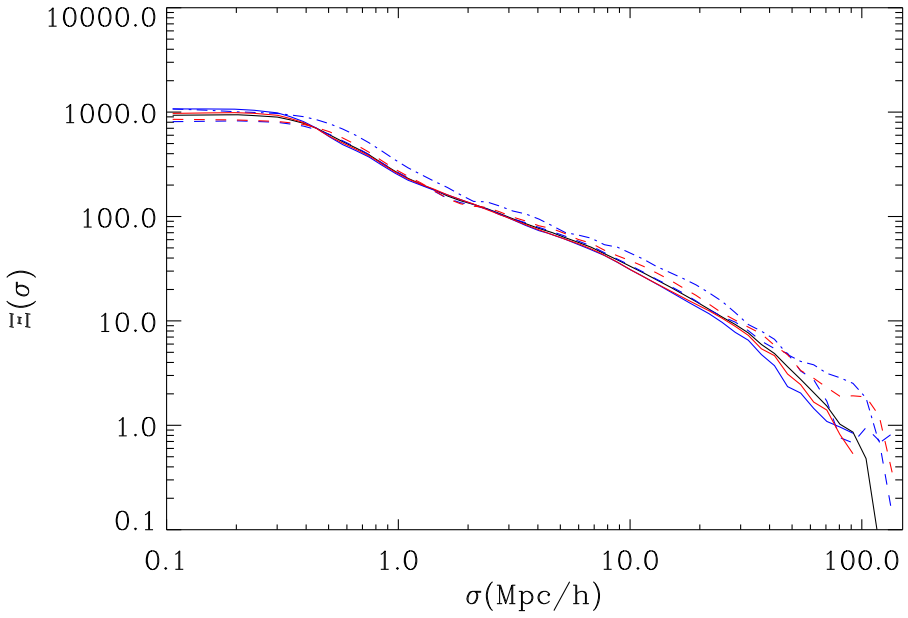

Figure 10.45: Comparison between the projected correlation function $\Xi(\sigma)$ for different slices in redshift. All: black, z=0.15-0.3 (solid blue), z=0.3-0.4 (dashed blue), z=0.4-0.47 (dashed-dotted blue); z=0.15-0.34 (solid red), z=0.34-0.47 (dashed red)

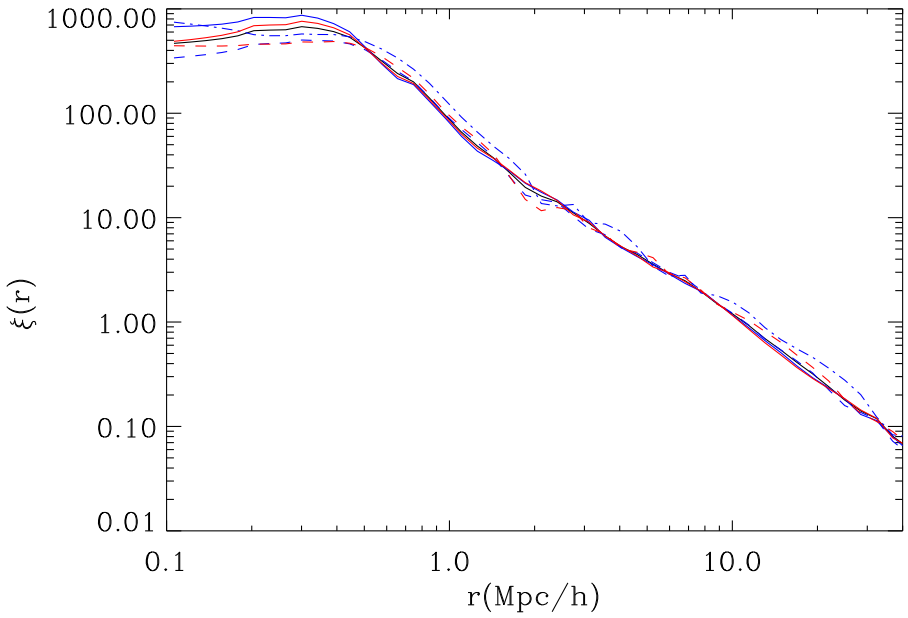

Figure 10.46: Comparison between $\xi(r)$ in real space for different slices in redshift. All: black, z=0.15-0.3 (solid blue), z=0.3-0.4 (dashed blue), z=0.4-0.47 (dashed-dotted blue); z=0.15-0.34 (solid red), z=0.34-0.47 (dashed red)

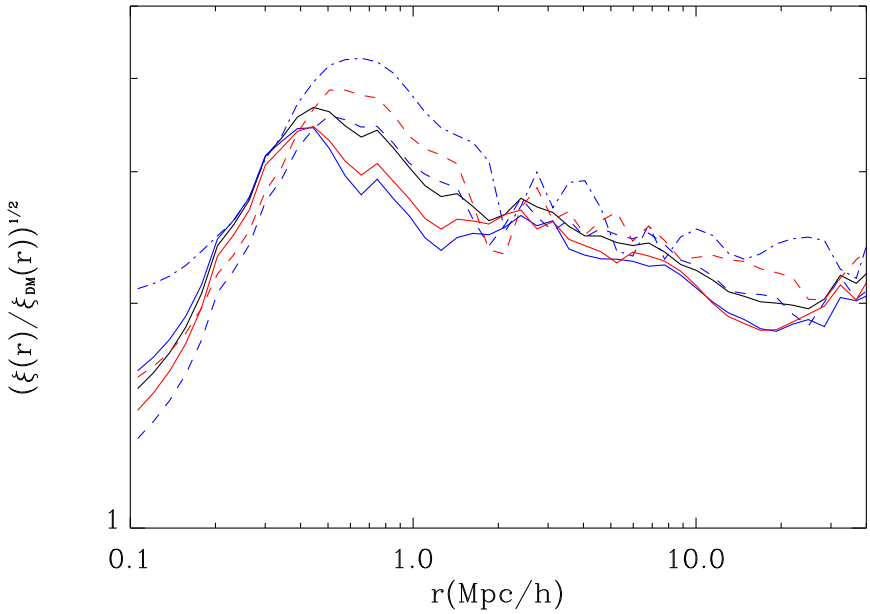

Figure 10.47: Comparison between the bias $b(z) = \sqrt{\xi(r)/\xi(r)_{DM}}$ (as in Eq.10.4) in real space for different slices in redshift. All: black, z=0.15-0.3 (solid blue), z=0.3-0.4 (dashed blue), z=0.4-0.47 (dashed-dotted blue); z=0.15-0.34 (solid red), z=0.34-0.47 (dashed red)

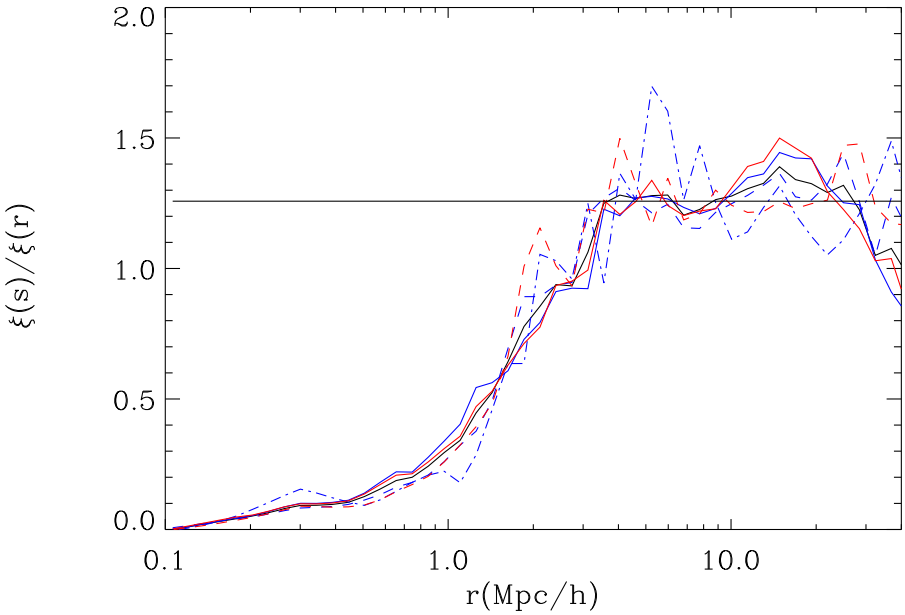

Figure 10.48: Comparison between $\xi(s)/\xi(r)$ for different slices in redshift. All: black, z=0.15-0.3 (solid blue), z=0.3-0.4 (dashed blue), z=0.4-0.47 (dashed-dotted blue); z=0.15-0.34 (solid red), z=0.34-0.47 (dashed red). The constant solid black line shows the Kaiser expression for $\xi(r)/\xi(s)$ at large scales (as a function of β, see Eq.(8.24)) for $\beta = 0.34$

10.9 Angular correlation and cross-correlation with WMAP, ISW effect

In this section we explore the angular correlation function and also the ISW effect through the cross-correlation between galaxies and fluctuations of temperature in WMAP. We point out that the catalog used here is the spectroscopic LRG, while the work done in the first part of the thesis uses the photometrical catalog of LRG, which has a different selection function, centered at a higher redshift (z=0.5). As seen in the theoretical section 8.6, the angular auto-correlation function GG goes like

$$w_{GG} \propto \sigma_8^2 \phi_G(z)^2 b(z)^2 D(z)^2 \tag{10.5}$$

and the cross-correlation function between galaxies and CMB temperature fluctuations w_{TG} is proportional to

$$w_{TG} \propto \sigma_8^2 \phi_G(z) b(z) D(z) \frac{d[D(z)/a]}{dz} \tag{10.6}$$

where

$$\frac{d[D(z)/a]}{dz} = D(z)(1-f) \tag{10.7}$$

Both expressions w_{GG} and w_{TG} are proportional to σ_8^2 because this factor comes from the normalization of the power spectrum, but w_{GG} is proportional to $(\phi_G(z)b(z)D(z))^2$ while w_{TG} is proportional to $(\phi_G(z)b(z)D(z))$ (from the clustering of galaxies) and $\frac{d[D(z)/a]}{dz}$ (from the evolution of gravitational potentials).

We find the signal w_{TG} higher than expected (see Fig.10.49 for the redshift slice z=0.15-0.34), a clear tendency that has been seen before (see Giannantonio et al. 2008 for a compilation of ISW observations). The high signal w_{TG} could be due to: σ_8 higher, Ω_m lower, non-linear effects, bias between matter and galaxies different from the one obtained from galaxies-galaxies, non-linear bias, different form of dark energy as $w > -1$ (see §6 for some hints in this direction), modified gravity at cosmological scales, or non-linear magnification (linear magnification is not expected to affect ISW at low redshifts, Loverde et al. 2007).

The signal to noise is not very high so we can not obtain tight constraints, but we can have an idea of what is creating this high signal. We study two reasons: a change in σ_8 or a change in the growth index γ. We have also studied these two parameters in the section of redshift distortions and we want to see if results are compatible.

We can break the degeneracy between $b(z)$ and σ_8 in the auto-correlation function w_{GG} (proportional to $b^2\sigma_8^2$) by combining the result with w_{TG} which depends differently on these two parameters, as $b\sigma_8^2$. We suppose that the factor $b(z)D(z) = b(z = z_{slice})D(z = z_{slice})$ is constant through all the redshift slice to be consistent with the previous section of redshift distortions.

We start from w_{GG}: we fix the shape ($\Omega_m = 0.25$) and find the factor $b(z = z_{slice})D(z = z_{slice})\sigma_8$ which should be equal to the one found in previous sections when analyzing redshift distortions, since we are working with the same galaxies LRG. Once we prove that it is the same value within the errors, we assume a flat universe, we fix the dark energy equation of

state parameter w to $w = -1$, and fix standard gravity ($\gamma = 0.55$). Now we can explain the w_{TG} observed by changing σ_8, and we can break the degeneracy of σ_8 with bias $b(z)$ in a way completely independent from the one used in the section of redshift distortions. In Fig.10.49, we have plotted at the top left the auto-correlation w_{GG} and over-plotted the best fit obtained from redshift distortions, on the top right w_{TG} and the best fit for σ_8 plotted on the bottom left panel versus χ^2, where we see that σ_8 tends to prefer higher values than the standard ones and also higher than the value σ_8 obtained in previous sections, but it is consistent within $1-\sigma$ errors ($\chi^2 = 1$). We only plot the redshift slice z=0.15-0.34 because the others have a higher noise.

Now we see how we can explain the observed ISW signal if it is due to a modification of gravity.

Once we know $D(z = z_{slice})b(z = z_{slice})$ from the angular auto-correlation function w_{GG} or from redshift distortions, we fix $\sigma_8 = 0.8$ and look for γ. We suppose that $w(z)$ changes slightly with γ and that almost all the variation with γ in ISW comes from the factor $D(1-f)$ (see the theoretical section 8.6 for a detailed explanation). See the bottom right panel in Fig.10.49 for χ^2 vs γ. Both D and $(1-f)$ grow with γ, so also $D(1-f)$ grows with γ (see Fig.10.22). If we want to obtain a higher signal, once fixed the rest of parameters, we can increase σ_8 or increase $D(1-f)$ for a low fixed σ_8, equivalent to increase γ. The conclusion is the following: if we fix σ_8 to a higher value, we need a lower value for γ; while for redshift distortions, if we fix σ_8 to a higher value, we need γ to be also higher. It seems to be a promising tool because both ways to obtain growth histories seem to go in opposite direction, and we will be able to break degeneracies in future surveys with best ISW signal.

From these observations, we conclude a preference for higher σ_8, or equivalently, a higher ISW unexpected in the standard model.

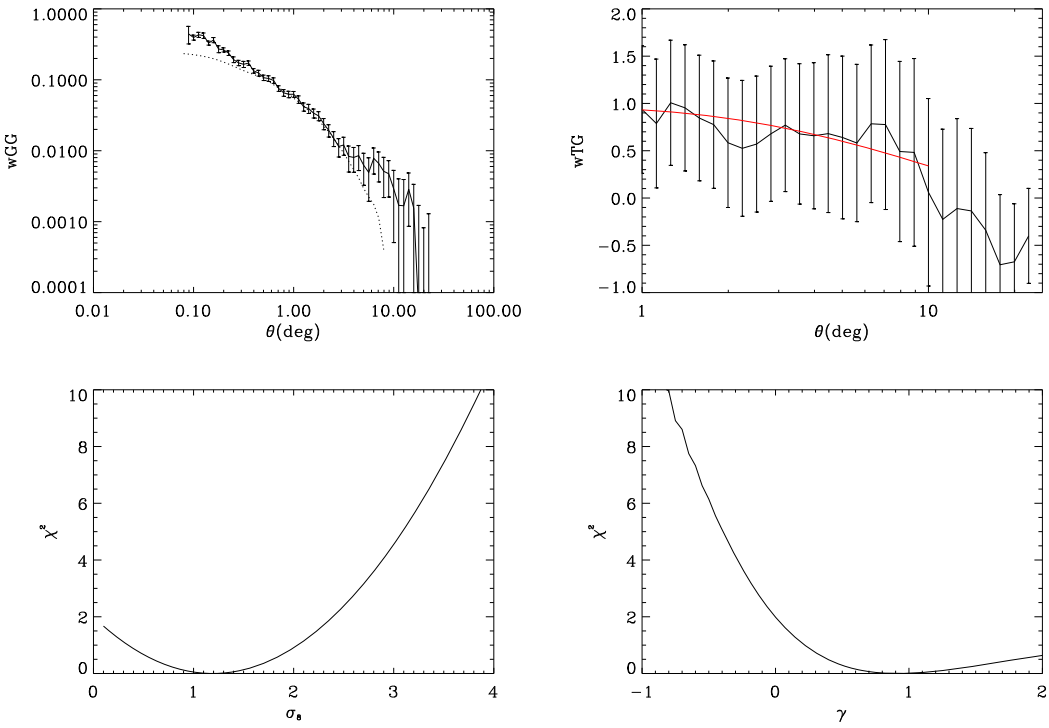

Figure 10.49: z=0.15-0.34. Top left: w_{GG} of LRGs (solid with errors) and best linear model (dotted line). Top right: w_{TG} (solid black with errors) and best model when fitting σ_8, for $\sigma_8 = 1.2$. Bottom left: χ^2 for σ_8 once we assume the rest of parameters fixed. Bottom right: χ^2 for γ once we assume $\sigma_8 = 0.8$

10.10 Evidence of magnification bias in the BAO

We expect a peak around 100Mpc/h in the real-space correlation function, which is also imprinted in the anisotropic redshift space $\xi(\pi, \sigma)$, produced by baryon oscillations (see §8.7). If we measure the peak in the radial direction, we find directly information about $H(z)$, since $dr = dz/H(z)$, while transforming angular separations involves the angular-diameter distance $D_A(z)$. In real data, recent surveys have used the averaged power spectrum or the monopole to do predictions, which position constrains cosmological parameters through a combination of $H(z)$ and $D_A(z)$ (also dependent on $H(z)$) (see Eisenstein et al. 2005b). In $\xi(\pi, \sigma)$, the differences between the perpendicular and parallel positions translate to an almost circular ring at around 100Mpc/h, although the peak is enhanced differently at each angle, because of redshift distortions. The peak is detected with higher signal if the galaxies are more biased and they trace a bigger volume, the reason why LRG are good galaxies to locate the position of the peak. Moreover, in the $\pi - \sigma$ plane, specially in the LOS direction, where we want to detect the peak, the error is dominated by shot noise. This means that the noise does not increase proportionally to signal, so if we increase the signal, we will have more signal to noise.

In the following plots (Fig.10.50, 10.51) we see the redshift-space correlation function $\xi(\pi, \sigma)$ for the complete catalog (z=0.15-0.47, top panel Fig.10.50), and for three different slices in redshift (z=0.15-0.3, bottom panel Fig.10.50; z=0.3-0.4, top panel Fig.10.51 and z=0.4-0.47, bottom panel Fig.10.51). For large scales, in the context of linear theory, we should see less power at the BAO scale when we approach the line-of-sight direction π, as we can see in the left panel of Fig.10.53, where we have plotted the linear model for the anisotropic $\xi(\pi, \sigma)$ using cosmological parameters similar to the ones derived in previous sections. Instead of that tendency, we see a baryon peak ring of equal amplitude (except for the intermediate slice z=0.3-0.4, with low S/N, where we do not see the ring). Moreover, the peak in the line-of-sight direction seems to be higher than in the rest of the ring. In this section we try to explain the reason of such a peak and we use the location to gain information about H(z). We only believe our results for s lower than 130Mpc/h, since we have seen in the monopole that after the baryon peak, there is too much power which could be due to selection effects (see Fig.10.44) and systematic errors could dominate over the statistical errors. On scales smaller than 130 Mpc/h these systematic errors have been shown to be smaller than statistical errors (Eisenstein et al. 2005b). Note that in separating σ from π in the data we have assumed plane-parallel approximation. This introduces a distortion of the BAO scale in the perpendicular direction $\sigma > 100 Mpc/h$ when π is small. This can be clearly seen in the plots, where there is an artificial concentration of signal in the direction of 30 degrees away from $\pi = 0$ at radial scales $r \simeq 100 Mpc/h$, which produces a X shape in our $\sigma - \pi$ plots. In reality this signal is distributed along smaller angles in the same radial bin. Thus, we do not extract information from the perpendicular direction σ at the BAO scale, since it could be affected by wide-angle effects. In §10.11 we show how to correct for this effect by removing some of the pairs in the calculation (see Fig.10.73). This is not the best possible approach, as we do not want to through away information, but shows the origin of the strange X shape features at large σ (see also Fig.9 in Matsubara 2000a). We can also use the monopole measurements which are not affected by these distortions (eg see Fig.10.43, 10.44) to explore the full BAO signal.

We use a fiducial model of $\Omega_m = 0.25$ through all the chapter to convert z into distances.

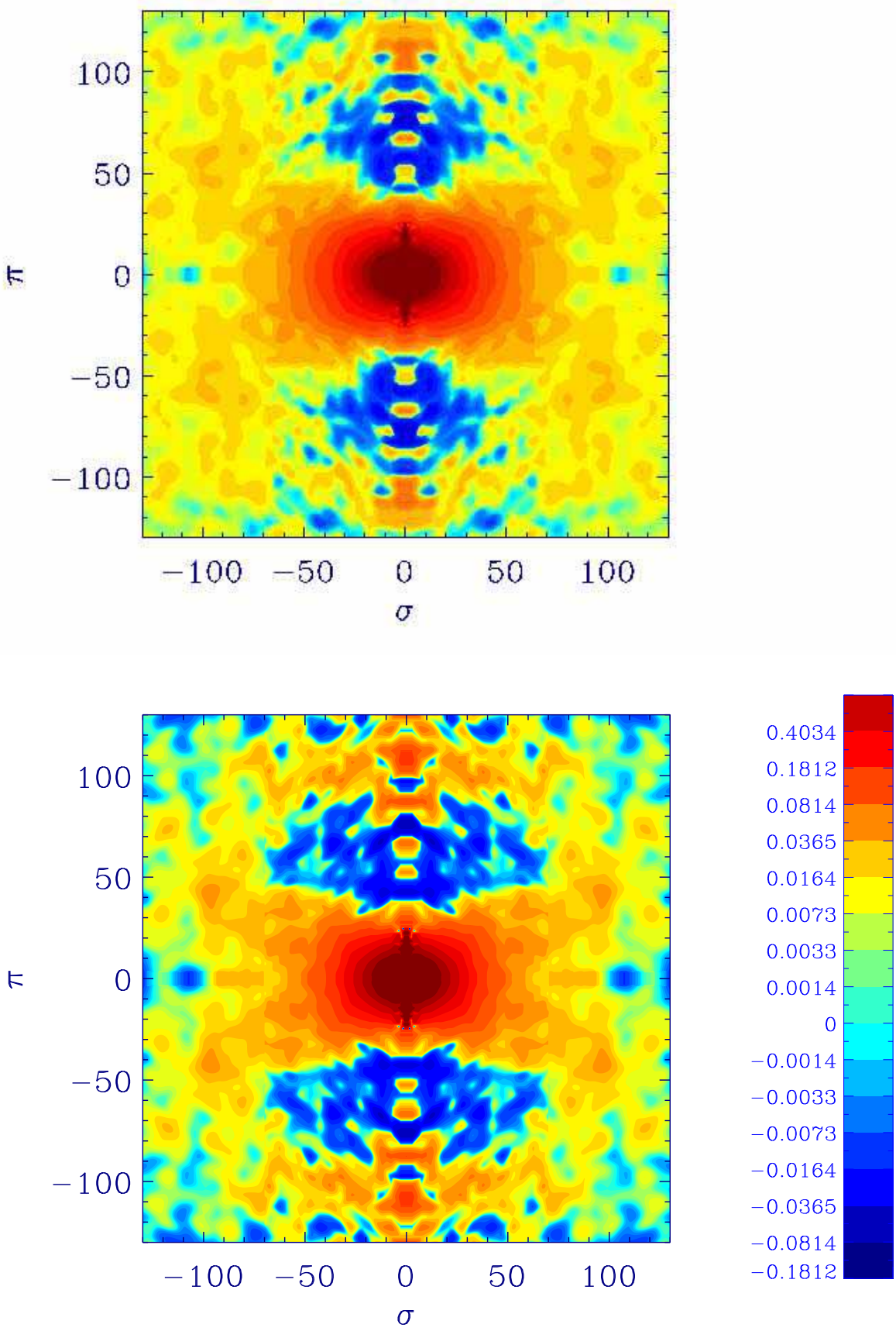

Figure 10.50: $\xi(\pi, \sigma)$ Top panel: z=0.15-0.47 (all). Bottom panel: z=0.15-0.30 . Distances in Mpc/h

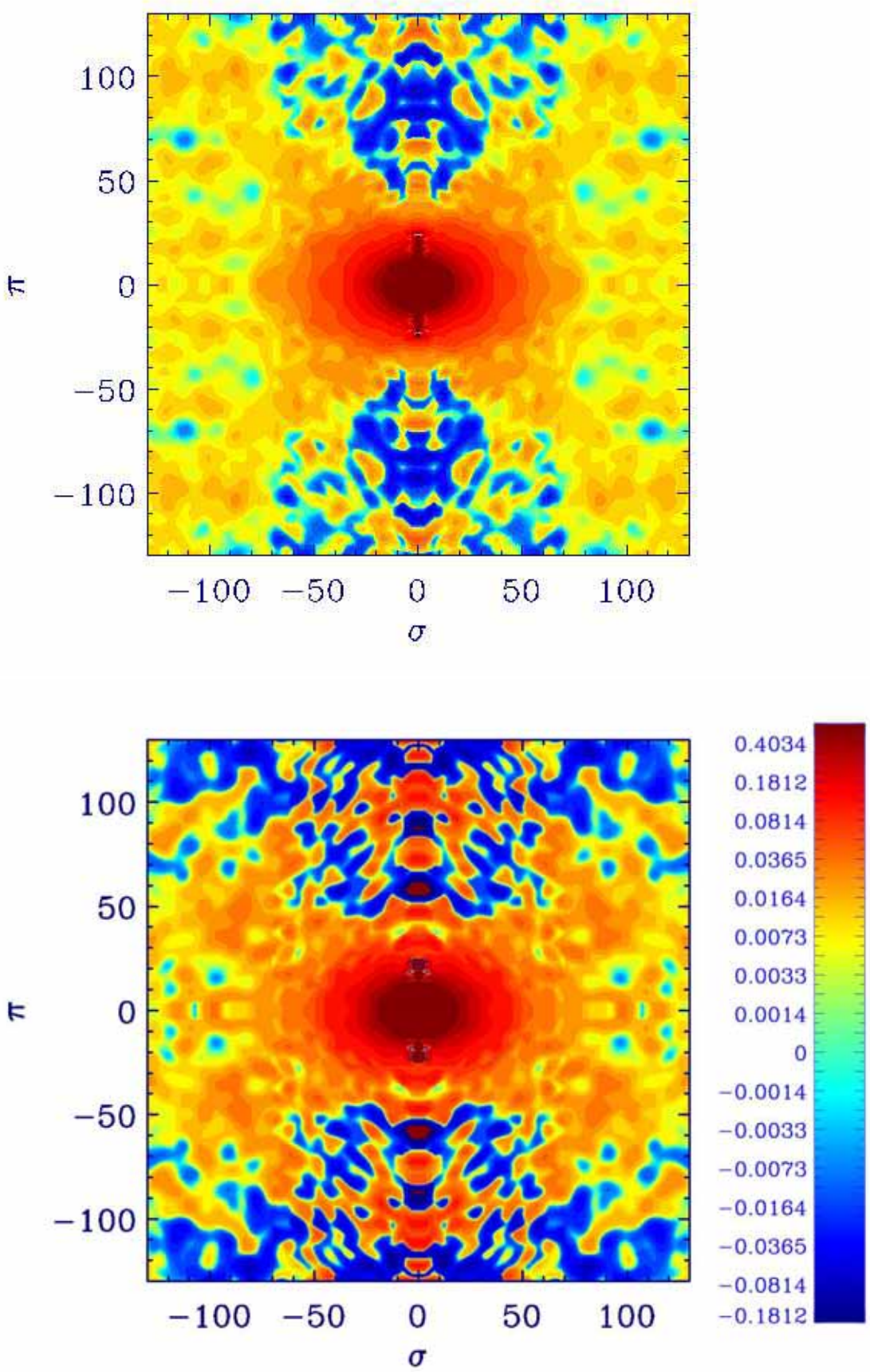

Figure 10.51: $\xi(\pi, \sigma)$ Top panel: z=0.30-0.40. Bottom panel: z=0.40-0.47 . Distances in Mpc/h

We have looked statistically to the significance of this BAO detection, through the null test: the probability that such an event to be different from zero by chance (the null result). We need this probability to be very low in order to have significance in the signal ($3-\sigma$ corresponds to a probability of 1%). We have performed a full covariance matrix analysis around the peak LOS position in a circle of s=10Mpc/h in the plane $\pi-\sigma$. There are 7 pixels in the $\sigma-\pi$ plane in our analysis. We find that the significance of the detection is more than 3-σ for the mean slice in redshift and the slice z=0.4-0.47 (probability of 0.8%). For the slice z=0.15-0.3, the significance is lower, 2-σ if we take all the signal in the circle 10Mpc/h, and increase when we center the study at the peak, as we will see in Fig.10.56. We notice that the peak seen in the LOS is followed by a ring in the plane $\pi-\sigma$ at around 100Mpc/h.

Once we know that the peak is significant, we try to explain the reason of such a big peak. It is not possible to explain this BAO peak in the direction of LOS only through redshift distortions in the linear regime, which predict a lower peak in the LOS than in the perpendicular direction. The peak that has been measured (see Fig.10.44) roughly in agreement with predictions for the monopole, is dominated by modes in the perpendicular direction, and it is 10 times lower ($\backsim$ 0.01) than the one we find in the LOS direction ($\backsim$ 0.1!), just in the contrary direction to expectations. We need to point out that it is precisely at the direction LOS where the errors are bigger, but the signal is even higher, as we have seen in the null test. In reality, even the measured monopole (in Fig.10.44) seems slightly larger than predictions, which could also be due to the LOS contribution to the monopole.

We think that the peak that we find in the LOS is primarily due to magnification bias (see §8.8), the effect caused by the dark matter which acts as a gravitational lens for the light coming from further galaxies. It can create an enhance of number of galaxies per pixel due to the lensing that allows us to see dimmer galaxies, and a suppression of the number of galaxies due to the growth of the area, which excludes some galaxies. The final net lensing is controlled by the slope in the number counts (Eq.(8.40)). This effect is really important at large scales and it is concentrated at the direction LOS, just where we are looking for. We only account for the cross-term, since the auto-magnification term is insignificant for our purpose.

In order to calculate the slope in the spectroscopic catalog LRG, we need information from dimmer galaxies than the limit of our catalog, to obtain the number count slope at exactly the magnitude cut (Eq.(8.40)). We take the photometric catalog, and with a similar selection in colors (adapted to photometry, explained in Chapter 6), we can calculate the slope, since we have dimmer galaxies in this new catalog. Because the photometric catalog is different from the spectroscopic one, we must take care when interpreting the slope. In Fig.10.52, we see the galaxy number counts depending on the apparent magnitude r and the logarithm of this expression, which indicates the slope. Our magnitude cut is around 19.2, where the slope is around 1.5. This is a rude estimation, but gives us an idea about the slope, which is clearly different from zero, thanks to the low magnitude cut (see Matsubara 2000b for more predictions of the slope s).

Fig.10.53 shows a comparison of the theoretical model for $\xi(\pi,\sigma)$ with and without magnification bias (right panel and left panel). We see how the LOS direction is affected by this contribution, enhancing the peak in the LOS over the case with no magnification. When we compared models of linear magnification bias to data, we find a good agreement in the shape but the amplitude can not explain the data with a slope of around 2. We think that it can be arranged with some non-linear contribution (non-linear magnification?), which would affect

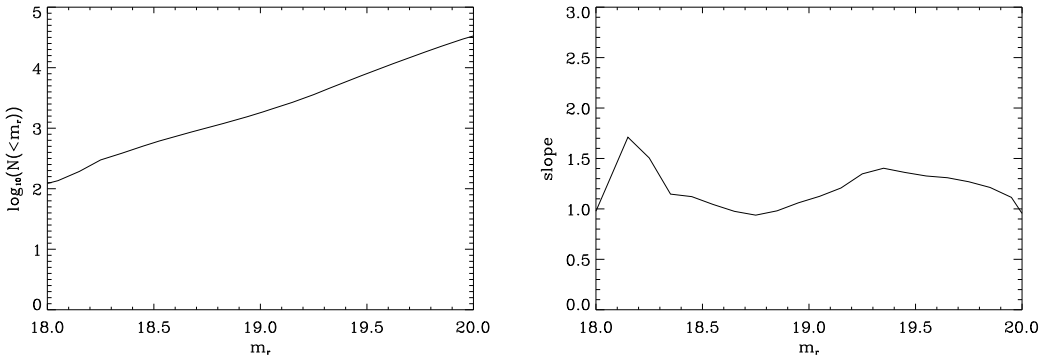

Figure 10.52: Number counts for each apparent magnitude and slope

the signal in a multiplicative way, or just with cosmic variance on top of the magnification signal.

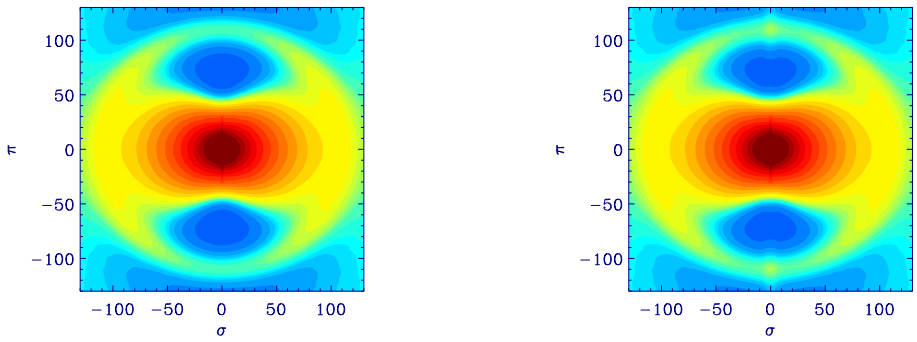

Figure 10.53: Theoretical $\xi(\pi, \sigma)$ Left panel: Linear model with redshift distortions. Right panel: The same with magnification bias (slope=2)

Fig.10.54 shows the correlation in the LOS direction for a squared bin of 5Mpc/h in the $\pi - \sigma$ plane (starting from $\sigma = 0.5 Mpc/h$ to avoid the fiber collision zone), moving the center of the bin 1Mpc/h each time in π (LOS direction) in order to have more precision. The top panel is in logarithmic scale to show a wider range of distances. We have plotted the correlation LOS in black (negative zones are dotted in the top panel), in blue the linear model assuming $\sigma_v = 600 km/s$, although in the top panel we have also plotted extreme models with $\sigma_v = 400 km/s$ (lower) and $\sigma_v = 800 km/s$ (higher) (we see that this range can be explained by a combination of σ_v dependent on scale. Since the bin is 5Mpc/h, FOG are not so evident as in §10.7.2, where we have proved that a change in σ_v dependent on scale, explains the FOG observed). The linear model alone can not explain the peak. When we add the magnification cross-term μg (cyan dashed) with slope of 2 to the linear model (redshift distortions) we obtain a higher peak (orange line). Taking into account the errors (the cosmic variance, dashed orange, bottom panel), the predictions are closer to the data, but we till need some additional multiplicative factor to match observations. If we increase the slope in the prediction of μg, we will have a LOS correlation with progressively less negative zone. We see clearly a negative zone at intermediate scales, so the best option is a multiplicative factor which enhances the positive parts, and the negative parts, this could be due to sampling variance. The peak in the monopole is wider than the one in LOS direction (see Fig.10.44). This is a consequence

of redshift distortions, which flatten the direction LOS and create a negative zone at intermediate scales (40-100Mpc/h). The peak in LOS comes after a negative range, so it is clearly observed since it is positive and the peak is more Gaussian, while in the monopole or the perpendicular direction, the peak is convolved with the typical power law at intermediate scales (positive), and it is no longer Gaussian.

In Fig.10.55 we have plotted the signal with errors for large scales, around the peak ($\backsim$ 110Mpc/h). We see clearly the peak except from the intermediate redshift slice, z=0.3-0.4. Errors are bigger in this slice because we have less volume and less number of pairs (specially in the radial direction, where we are looking). We have over-plotted the linear prediction at the direction LOS, multiplied by a factor of 10, to simulate the magnification effect.

In order to see more clearly the peak and the significance just in LOS direction, we plot $(S/N)^2$ in Fig.10.56, an estimation of χ^2. We have also done the analysis using an angular mask with 10% less galaxies, which are safely inside "good" plates, and with a radial selection function which is smoother (dz=0.05) than our default value of dz=0.02 (see §10.11). This new case allows us to see how solid is the result and look for systematic errors. We have over-plotted in Fig.10.55 and Fig.10.56 the new result (dashed line). We see how for the all sky catalog the systematic effects can suppress the peak. This can be understood easily since it is a mixture of different slices in redshift and we find that the BAO peak position tends to decrease with redshift resulting in a degradation of the mean signal.

Once we have a plausible explanation for the origin of the peak, we can take advantage of the high S/N in LOS to obtain cosmological constraints, through the factor $H(z)$. The idea is to compare the well known measure of the baryonic peak calculated by WMAP5, with the peak that we obtain using a fiducial cosmology (in our case $\Omega_m = 0.25$ and $w = -1$, although we have tried other fiducial models and results are similar). In the LOS direction, the only change in the location is due to H(z), used to estimate the distances from redshifts, $dr = dzc/H(z)$. Following this argument, we can directly calculate H(z) at the redshift of the survey, comparing the comoving distance of the survey peak with the WMAP peak.

$$H(z)_{real} = r_{survey}/r_{WMAP} H(z)_{fiducial} \tag{10.8}$$

where the peak measured by WMAP5 is $r_{WMAP} = 146.8 \pm 1.8 Mpc$ being r the comoving distance, $H(z)_{fiducial}$ is the one used when computing the comoving distance of the peak in the survey (r_{survey}),

$$H(z)/H_0 = \sqrt{\Omega_m (1+z)^3 + (1-\Omega_m)(1+z)^{3(1+w)}} \tag{10.9}$$

if we suppose a flat universe and a dark energy equation of state constant parameter w. The difference between $H(z)_{real}$ and $H(z)_{fiducial}$ will tell us about a different Ω_m than the fiducial in our Universe or a different constant w. In order to obtain the error in the peak, we take the maximum value in $(S/N)^2$ at the BAO scale, and see the range of distances where $\chi^2 = (S/N)^2 > (S/N)^2_{peak} - 1$, which means $1-\sigma$ from the maximum. When we include the covariance, the significance is slightly lower, but the errors are still the same. This is because the covariance with neighboring bins in the direction LOS is $\backsim$ 20% (dotted line in Fig.10.56).

We should take care with the conclusions, because we have not modeled in detail the relation between the peak in the correlation function with the actual BAO sound horizon scale as measured from WMAP, so the position could be slightly biased. This has been recently

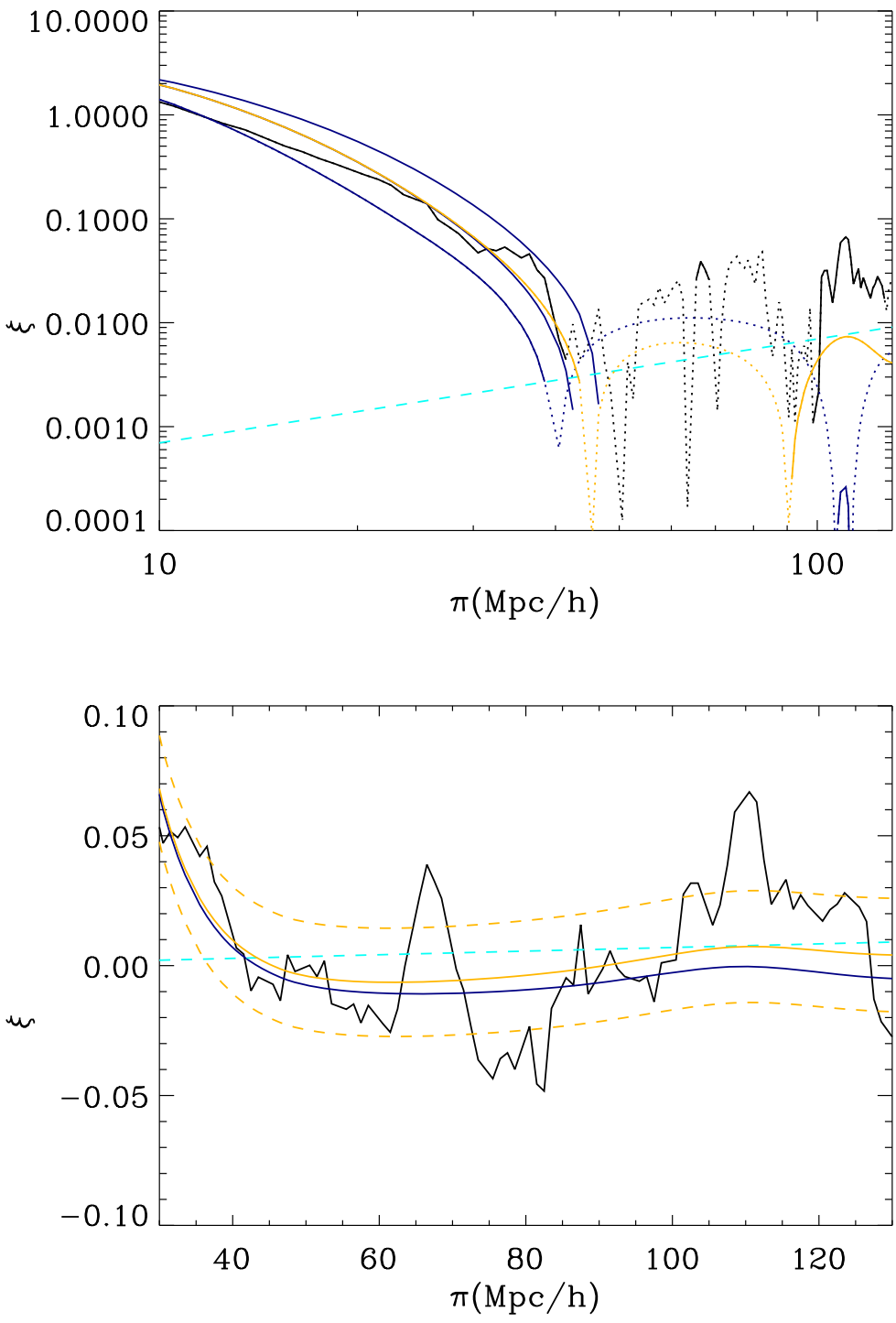

Figure 10.54: correlation $\xi(\pi, \sigma)$ at LOS in black (negative zones are dotted in the top panel), in blue the linear model assuming $\sigma_v = 600$, although in the top panel we have also plotted extreme models with $\sigma_v = 400$ (lower) and $\sigma_v = 800$ (higher). Cross-term μg (cyan dashed) added to the linear model (orange line), and errors over the model (dashed orange in the bottom panel)

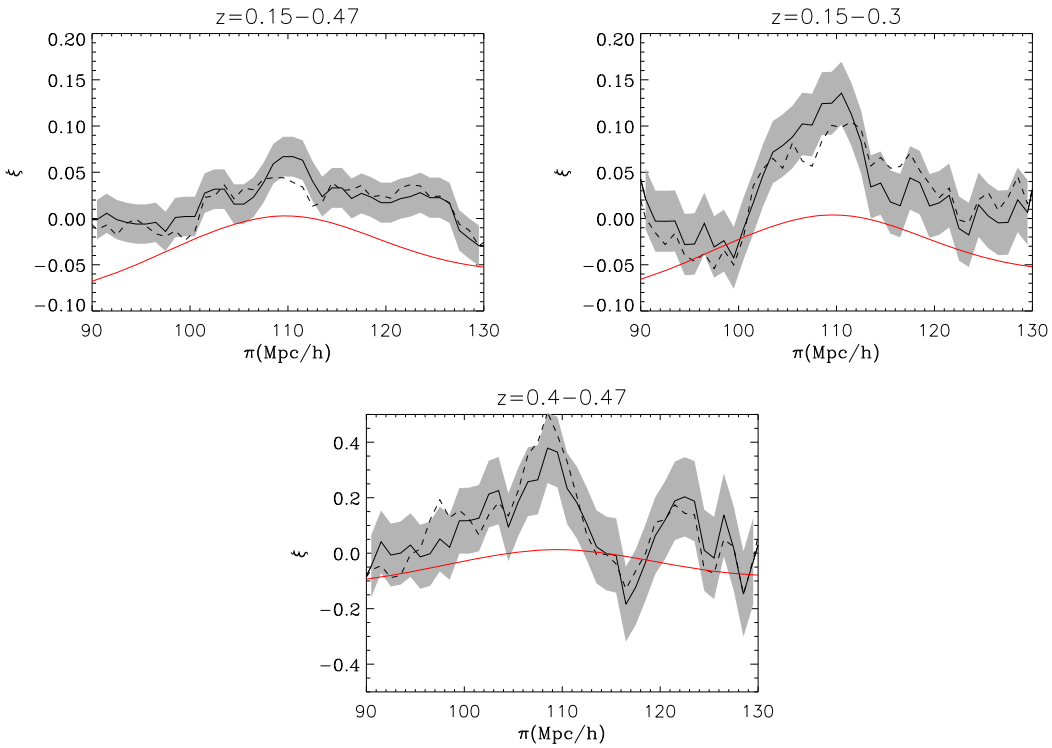

Figure 10.55: Redshift-space correlation function $\xi(\pi, \sigma)$ in the direction LOS (solid black) with linear model multiplied by a factor 10 (solid red), with errors (gray area). We plot also the result for a different mask explained in the text (dashed line). Redshift slice as indicated in the same figure

explored by Sanchez et al. (2008). Their Fig.2 shows that at $\Omega_m = 0.25$ the peak in the correlation function (using CAMB) systematically underestimates the true sound horizon by about 1.5% (this error increases to 2% for $\Omega_m = 0.2$ and reduces to 1% for $\Omega_m = 0.3$). This is a large (but well predictable) systematic effect and we could in principle correct our measurements for this. The problem is that this correction depends on the width of the BAO peak as given by the Silk damping. In the case of the correlation function along the line of sight, the width of the BAO peak is smaller due to the Kaiser effect (see Fig.10.53). If anything, magnification bias would tend to move the peak by a similar amount (less than a percent) in the opposite direction (see Hui et al. 2007). We conclude that it is safer not to apply any correction here and just increase the systematic error by about 1% to account for a possible systematic in this conversion. In Table 10.10 we show the values for the position of the peak for different redshift slices, the mean statistical error, the systematic error and the corresponding H(z). Systematic errors (added linearly) are given by the difference in the results using different mask and different selection functions and also the uncertainty in the conversion between the peak position and the sound horizon scale mentioned above. For illustration purposes, we will use the mean peak value among both masks for the following calculations, the mean statistical error and, added in quadrature, the systematic error.

We obtain $H(z)$ from Eq.(10.8), for each slice. For the errors,

$$\sigma_{H_{real}} = \sqrt{\left(\frac{\sigma_{r_{survey}}}{r_{survey}}\right)^2 + \left(\frac{\sigma_{r_{WMAP}}}{r_{WMAP}}\right)^2}\, H_{real}. \tag{10.10}$$

In Fig.10.57 we see the H calculated from the well located peaks. We over-plot the best

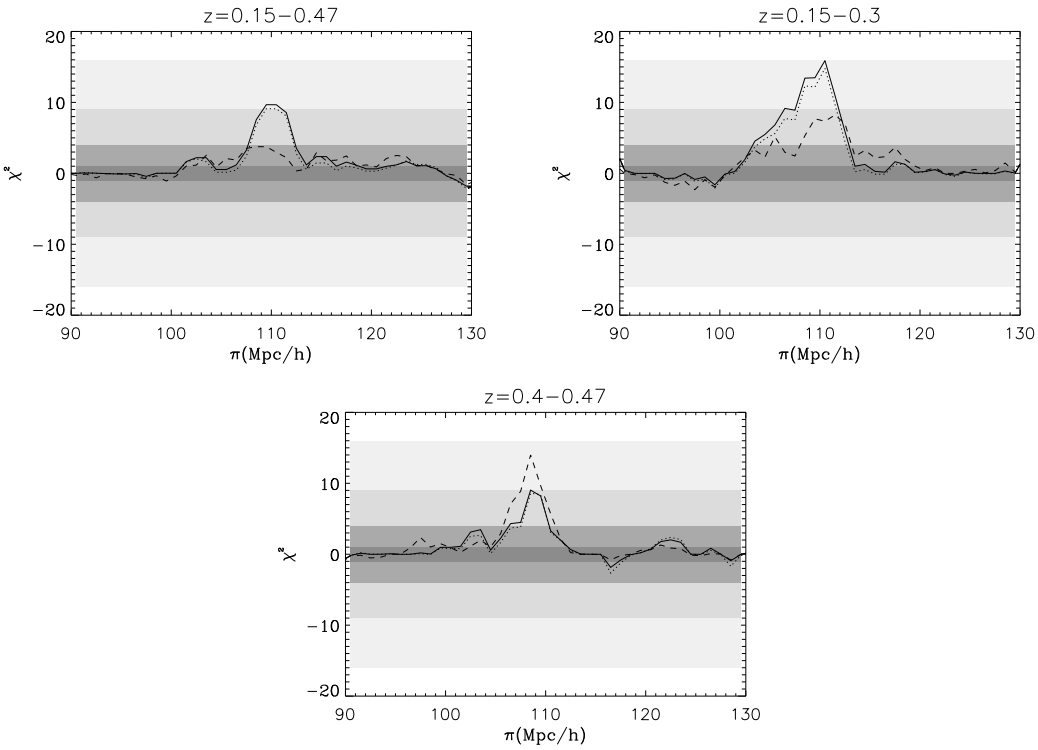

Figure 10.56: In this figure we plot the significance of the detection as $\chi^2 = (S/N)^2$ (solid line) and χ^2 when including the covariance (dotted line). We plot also the results for a slightly different mask as explained in the text (dashed line). Redshift slice as indicated in the same figure. The gray zones indicate a 1-σ, 2-σ, 3-σ or 4-σ detection

Sample	$r_{\Omega_m=0.25}$ Mpc/h	σ_{st}	σ_{sys}	H(z) km/s/Mpc	σ_{st}	σ_{sys}
z=0.15-0.47 ($z_m = 0.34$)	109.6	1.6	1.7	86.8	1.7	1.2
z=0.15-0.3 ($z_m = 0.24$)	110.5	0.75	1.35	83.4	1.2	1.0
z=0.4-0.47 ($z_m = 0.43$)	108.6	0.4	1.22	90.0	1.2	1.1

Table 10.3: Mean position of the BAO peak in the LOS direction calculated with a fiducial $\Omega_m = 0.25$ and statistical and systematic error , and also the derived H(z) with its associated errors for each redshift slice

flat ΛCDM model (w=-1) with WMAP5 parameters $\Omega_m = 0.258 \pm 0.03$, $h = 0.72 \pm 0.026$ and errors (red line and orange shaded area). We see that our estimation of H(z) lays within the errors, but with a tendency of higher Hubble constant h (or higher Ω_m for h=0.72) and different slope, indicating that w could be a function of redshift. This reflects the tendency of the BAO scale to decrease with redshifts (see Table 10.10).

We see what happens when we fix Ω_m to a fixed value, and fit a constant w for each redshift slice. In Fig.10.58, we see the constraints in $w(z)$ once we fix Ω_m to 0.2 (red), 0.25 (black) or 0.3 (blue), and h=0.72. There is a tendency of w to depend on the scale (higher w when we approach z=0).

We can see the same effect by fixing again h=0.72, assuming a flat universe ($\Omega_m + \Omega_\Lambda = 1$)

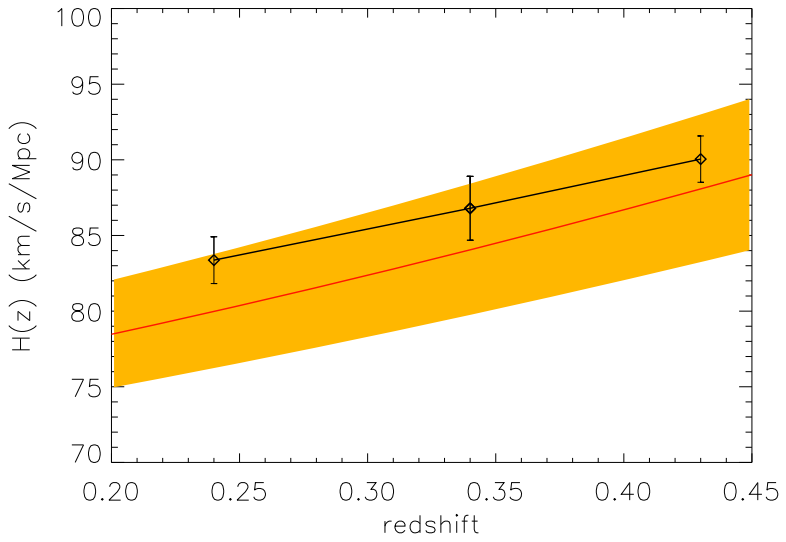

Figure 10.57: $H(z)$ obtained from different redshift slices (points with errors), the red line shows the best value for H(z) from WMAP5, and errors (orange)

and supposing a constant value for w. We obtain a degenerated relation between Ω_m and w (Eq.(10.9)). We can see the result in Fig.10.59 for different redshifts. Again, we only can explain this plot by assuming different w for a given realistic Ω_m. We point out that Eisenstein et al. (2005b) also obtain a high value for Ω_m (the one that better explain a w near -1) and their result for w is also higher than the standard $w = -1$, although the method they follow is based in an analysis of intermediate and large scales (including the baryon peak) in the monopole, which constrains the same parameters in another way.

We think that the use of redshift anisotropies in the BAO peak can constrain better the parameters H_0, Ω_m and $w(z)$ in future surveys. We let to future work the complete modelization of the BAO peak at all the directions of the plane $\pi - \sigma$.

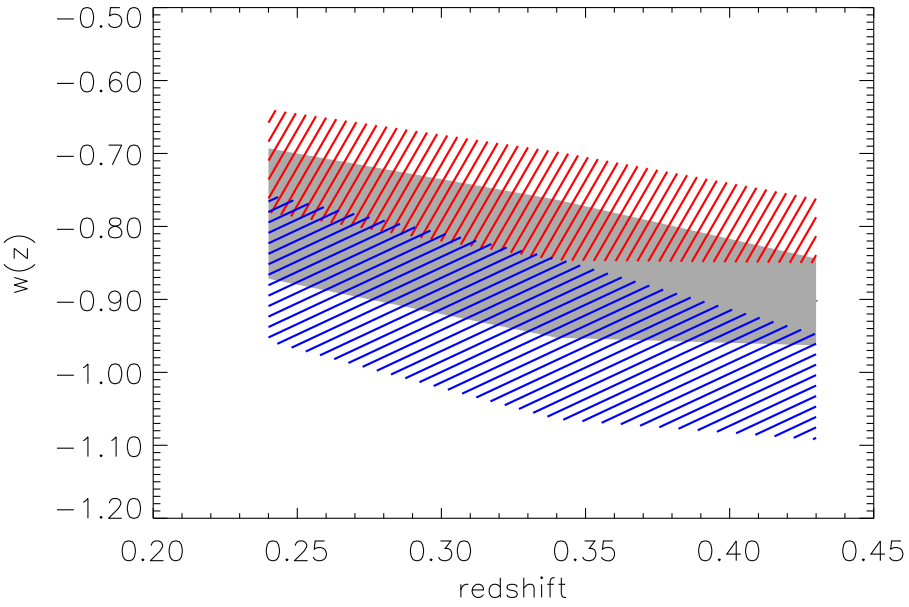

Figure 10.58: We fix Ω_m to 0.20 (red), 0.25 (black) or 0.30 (blue) and explain the H(z) given in Fig.10.57 by a constant w at each redshift

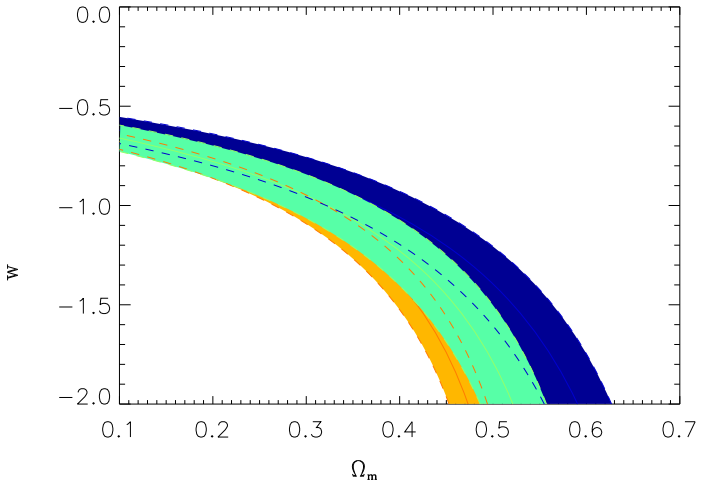

Figure 10.59: Contour $\Omega_m - w$ obtained from the position of the BAO peak, z=0.15-0.47 (green), z=0.15-0.3 (blue), z=0.4-0.47 (orange)

10.11 Systematic errors

In this section we look for possible systematic errors that could be imprinted by the radial mask through the line-of-sight, the angular mask, or the selection in LRG galaxies. In Fig.10.44 we show that for some slices there is extra power in $\xi(s)$ at scales $s > 130 Mpc/h$, something which is not expected in the models. This is particularly evident for the slice in redshift z=0.3-0.4. This extra power could be due to sampling variance but could also be caused by some systematic errors in the data or the way we analyze it. The extra power seems to be important at scales larger than the baryonic peak, but we test here if it could also have some effect over the peak location.

First, we test the radial selection function that we use for the random catalog. If we use exactly the same selection function of the data, we suppress the radial modes, the π direction. In Fig.10.60 we can see the differences between different smoothing windows in the data selection function, and in Fig.10.61 the redshift-space correlation function for these three smoothing bins. We do not see any significant difference between the three cases.

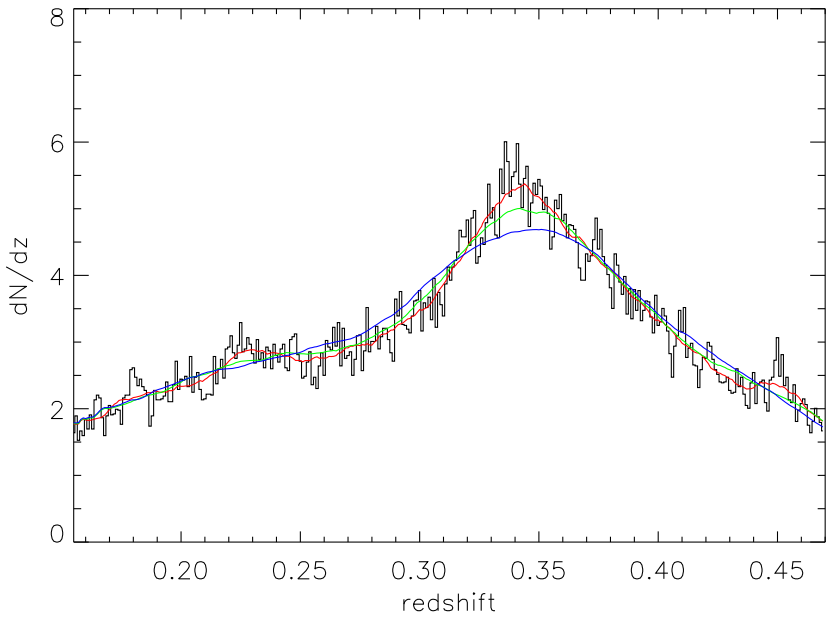

Figure 10.60: Selection function for data (black histogram) and random smoothing for a bin in redshift of z=0.02 (red), z=0.05 (green) and z=0.08 (blue)

In Fig.10.62 we look at the difference between the results of Eisenstein et al. (2005b) (in black) and our results (in red). Our result is consistent with their work despite our larger area and the difference in the selection. However, at larger scales than the baryonic peak, we observe some extra-power. We wonder if the difference is just due to sampling, selection or to the way we estimate the correlation function (we do not include weighting).

We have also calculated the correlation function using a weighting scheme, as the one explained in Eisenstein et al. (2005b). We weight the sample using a scale-independent weighting that depends on redshift. When computing the correlation function, each galaxy and random point is weighted by 1/(1 + n(z)Pw) (Feldman et al. 1994) where n(z) is the comoving

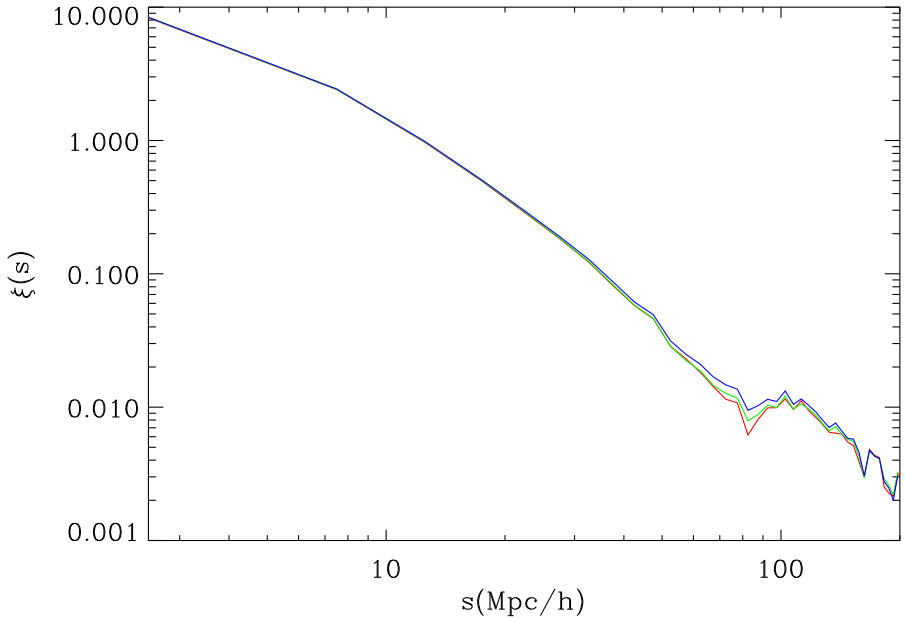

Figure 10.61: Redshift-space correlation using a redshift smoothing in the random selection function of 0.02 (red), 0.05 (green) and 0.08 (blue)

number density and $Pw = 40,000h^{-3}Mpc^3$. We do not allow Pw to change with scale so as to avoid scale-dependent changes in the effective bias caused by differential changes in the sample redshift. We choose Pw at $k \backsim 0.05hMpc^{-1}$ as in Eisenstein et al. (2005b). At z $<$ 0.36, nPw is about 4, while $nPw \backsim 1$ at z = 0.47. In Fig.10.63 we can see the comparison between the correlation function estimated without weighting (solid line) and with weighting (dashed line). It seems that contrary of what we were looking for, the extra power is higher in the weighting scheme, which is logical, since we are now giving more importance to the far pairs, which have a higher bias. In Fig.10.64 we have plotted the anisotropic correlation function $\xi(\pi, \sigma)$ for both cases, showing slight differences.

We have also looked at the angular selection function, the mask. First, we construct a different mask than the original by using a Healpix map, with nside=64 (with pixels of area$\backsim$0.8 sq deg). In Fig.10.65 we plot the distribution function for the number of galaxies per pixel. The pixel is large enough to distinguish between real empty pixels and artificial ones. We only include pixels that have more than n galaxies (where n=2,6,10). As we can see in the distribution plot, if we include more than 2 galaxies, we are probably including artificially void zones, which will create extra power and pencil beams at the direction line-of-sight, while when we include only the pixels with more than 10 galaxies, we are probably excluding some real voids. In this second case, the density is higher than the real one, so the density contrast is lower. We can see these effects in Fig.10.66 for the correlation function in redshift space. We see that the correlation is lower when we increase the minimum number of galaxies (from red to blue), but we can always see the baryonic peak and the three lines have the same shape approximately. Our results are similar to the case n $>$ 6, which does not include artificial voids and does not eliminate real voids. In Fig.10.67 we see the correlation in $\pi - \sigma$, which is lower when we increase the minimum number of galaxies, and we observe clearly the pencil beams for the case n=2 through the direction π, when we include artificially voids.

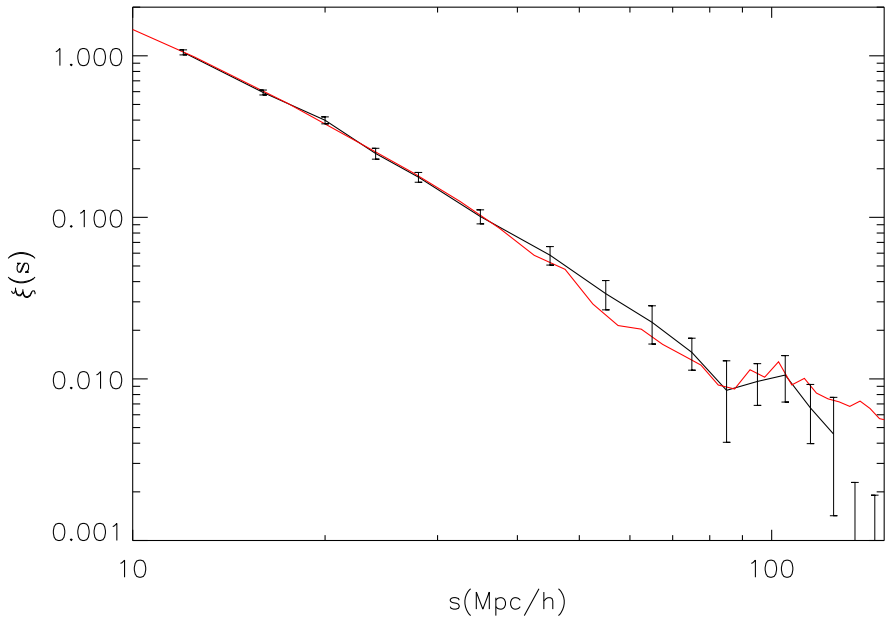

Figure 10.62: Estimation of the redshift-space correlation function for LRG. In black with JK errors the result by Eisenstein et al. (2005b), and over-plotted in red our result

The spectroscopic survey of SDSS is observed using circular plates, which contain about 600 fibers each to take spectra. Targets are selected from the photometric survey, although the spectroscopic survey is not exactly the same as the photometric one. There are some plates that have not been observed properly due to known problems, which are explained in the web (http://www.sdss.org). We have extracted from our previously calculated mask all the galaxies that are not laying inside "good" plates (maskplate1). In Fig.10.68 we can see the plates (black circles) and the galaxies (red). Moreover, we can also eliminate all the galaxies that lay inside a bad plate to ensure that we are taking only the really good ones (maskplate2). This second mask reduces the number of galaxies significantly, and the correlation is then a lot noisier, but we show here the results. In Fig.10.69 we have plotted the redshift-space averaged correlation function for the new mask based on spectroscopic plates. Results are very similar to our previous result, in black. Moreover, we over-plot the result for the north stripe of SDSS, which contains the most significant part of the survey, in blue. The anisotropic redshift-space correlation function is really similar in all these cases, so that we do not find it useful to plot it.

We have also tried to extract all the plates that have a large number of galaxies, which have big clusters, since it is known that big clusters can bias the correlation function. The result is not significantly modified.

In volume limited surveys, we can estimate the correlation function with a pixelization scheme. As explained in the first part of the thesis, the correlation function can be estimated as:

$$\xi(s) = \sum_{ij} \delta_G(s_i)\delta_G(s_j)/N_{pairs}(s) \tag{10.11}$$

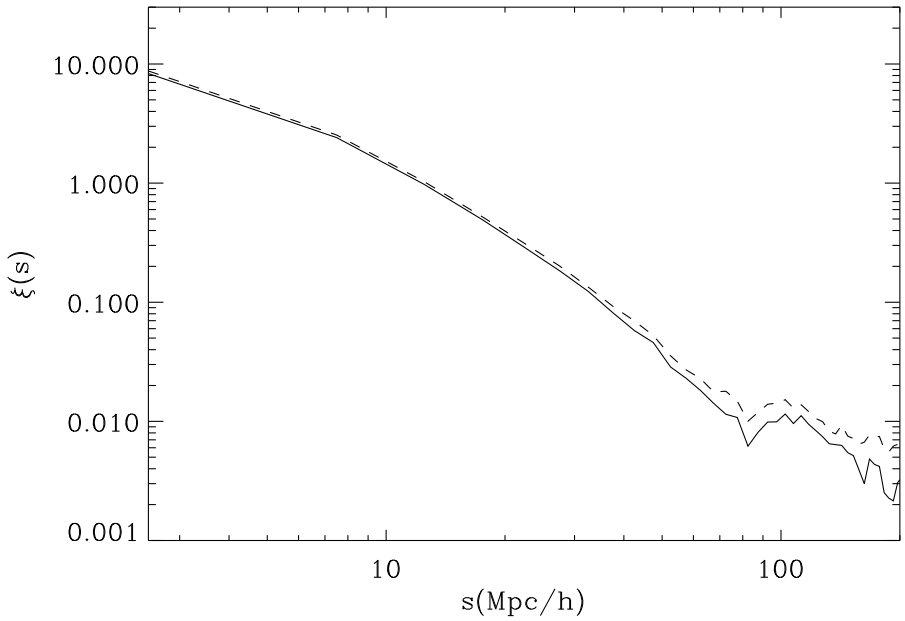

Figure 10.63: Our previous estimation of the redshift-space correlation function for LRG (solid) compared to estimation using a weighting as explained in the text (dotted)

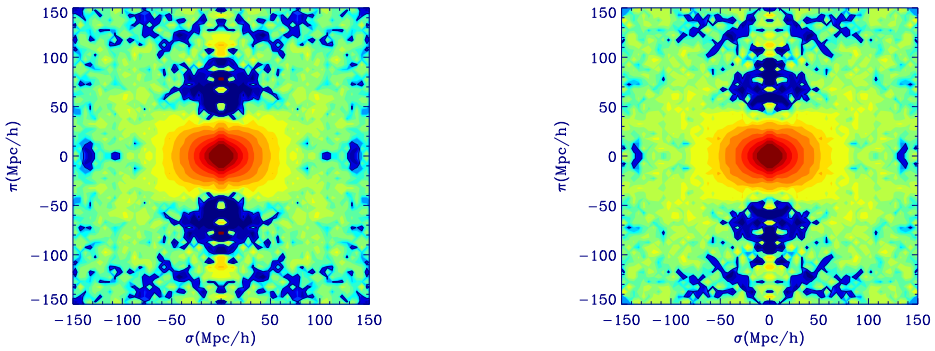

Figure 10.64: Our previous estimation of the redshift-space correlation function $\xi(\pi, \sigma)$ for LRG (left panel) compared to estimation using a weighting as explained in the text (right panel)

where $\delta_G = N_G / < N_G > -1$ and the sum extends to all pairs i,j separated by a distance $s \pm \Delta s$. We have taken a volume limited part of the selected galaxies, with redshift z=[0.15,0.38] and absolute magnitude M_r=[-22.5,-21.5] and have calculated the correlation using this method. We have also calculated a similar selection by using the traditional method with a random catalog. Results are plotted in Fig.10.70, dotted for the pixel method and solid for the randoms. This is a good test to validate our results, since both methods are quite different. As we can seen in the figure, the two estimations are very similar. The slight shift of amplitude at small scales is due to the pixel smoothing, 10 Mpc/h on the side for this case. There is a very good match for smaller pixel size. Also note how these estimations, based on a volume limited sample with about half of the LRG galaxies, agree quite well with previous results (ie in Fig.10.69) which includes all galaxies at a price of a more complicated selection function.

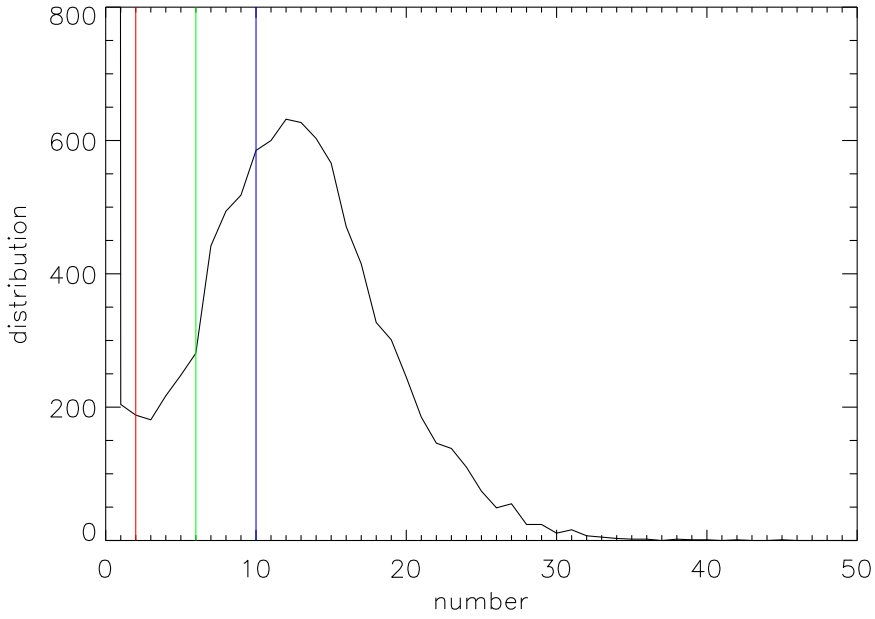

Figure 10.65: Distribution function of number of galaxies per pixel (nside=64 using the package Healpix)

Table 10.4: Slices in the plane $M_r - z$

Sample	M-range	Mean M	mean z	z-range
S22.50	-22.50 -23.00	-22.75	0.43	0.35-0.50
S22.25	-22.25 -22.75	-22.50	0.40	0.33-0.48
S22.00	-22.00 -22.50	-22.25	0.38	0.31-0.46
S21.75h	-21.75 -22.25	-22.00	0.35	0.27-0.42
S21.75	-21.75 -22.25	-22.00	0.20	0.12-0.27
S21.50h	-21.50 -22.00	-21.75	0.32	0.25-0.40
S21.50	-21.50 -22.00	-21.75	0.18	0.10-0.25
S21.25	-21.25 -21.75	-21.50	0.18	0.10-0.25

Finally we have also divided the catalog in many different volume limited slices as indicated in table 10.11 plotted in Fig.10.71. The most and less luminous slices (in the bottom right and top left) contain fewer galaxies and do not trace properly the baryonic peak, but we see that the red and pink slices, at intermediate redshifts and magnitudes, are the origin of the extra-power that we see at large scales (Fig.10.72 with the same colors as Fig.10.71). We have not plotted large scales for the other slices because they are quite noisy. However, at intermediate scales, we can see clearly the bias due to different intrinsic luminosity, more biased when more luminous, although bias seems to be independent on scale, in the scales used for our analysis.

Finally, we have calculated the correlation function limiting the angle between galaxies to see if wide angle effects disappear. In Fig.10.73, we see the anisotropic $\xi(\pi, \sigma)$ without limits

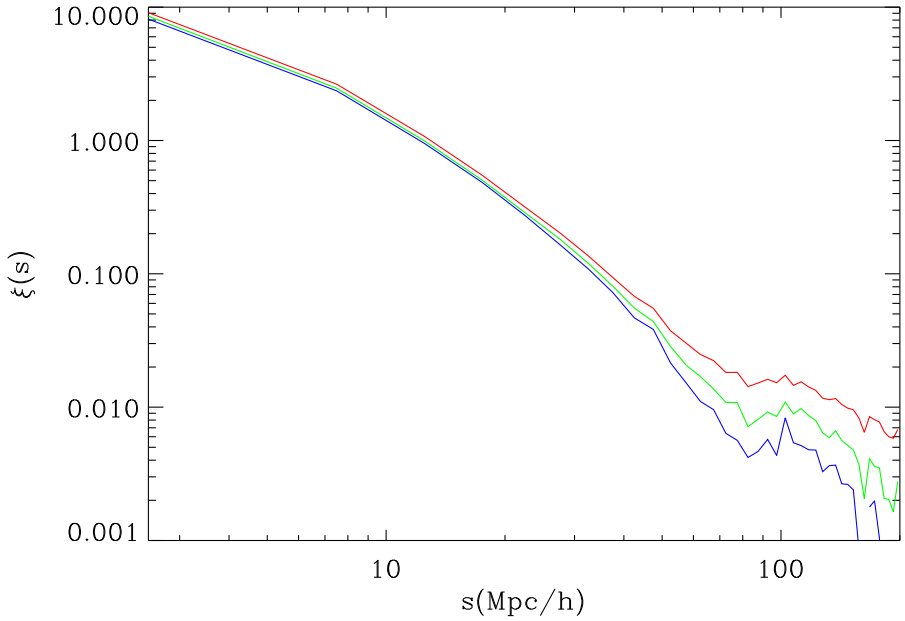

Figure 10.66: We now define our catalog by including all the pixels that have more than n galaxies in the Fig.10.65 (n>2 red, n>6 green, n>10 blue) and plot the redshift-space correlation function

in the angle (top panel), accepting galaxies with $\theta < 15deg$ (middle panel) and $\theta < 10deg$ (bottom panel). As we increase the restriction, we see how the σ direction recovers power, which explains the lack of power we see at σ direction when angles are too big to apply the distant observer approximation. The angle between galaxies explain part of the distortions due to wide angle effects, specially the ones that are concentrated at small π and large σ, which affect the first slice considered, from z=0.15-0.3. The angle γ_z, between the direction LOS (at $\theta/2$) and the vector which goes from galaxy 1 to galaxy 2 (following the notation used in Matsubara 2000a), is also important and can also imprint some modifications at larger π and large σ.

We conclude that the measurements on the BAO scale are quite robust and the extra power at the largest scales is probably the result of sampling fluctuations.

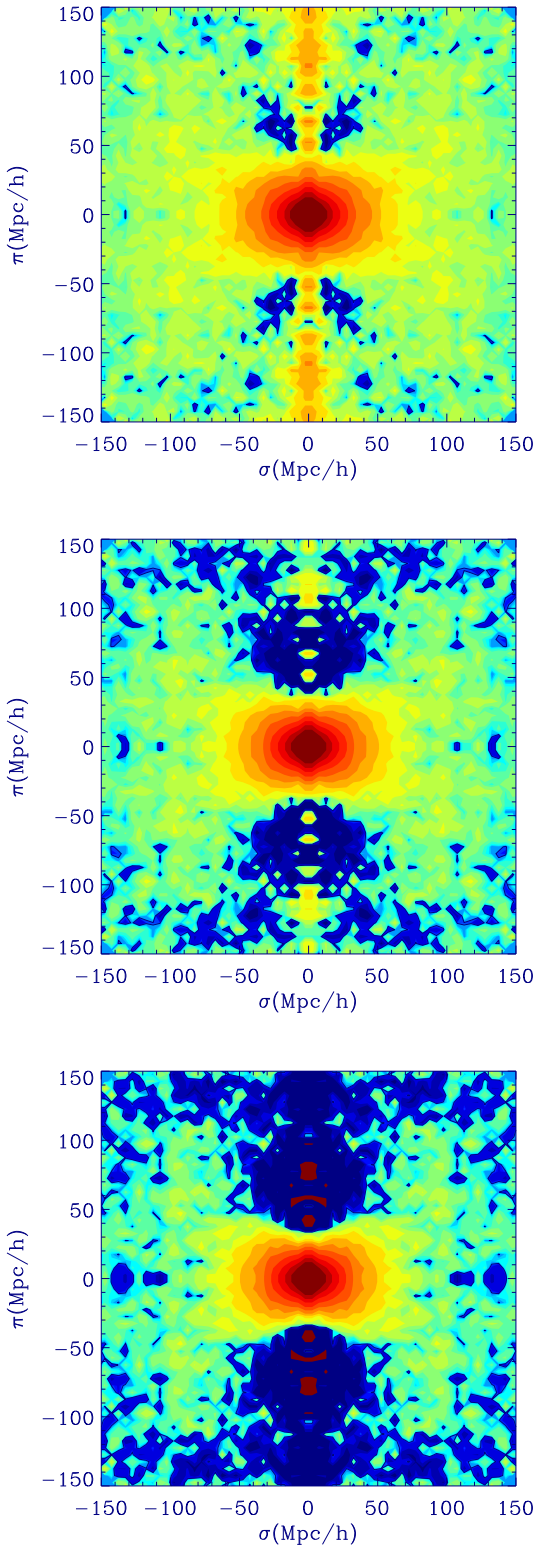

Figure 10.67: Redshift-space correlation function $\xi(\pi, \sigma)$ for n>2 (top panel), n>6 (middle panel), n>10 (bottom panel), as in Fig.10.65

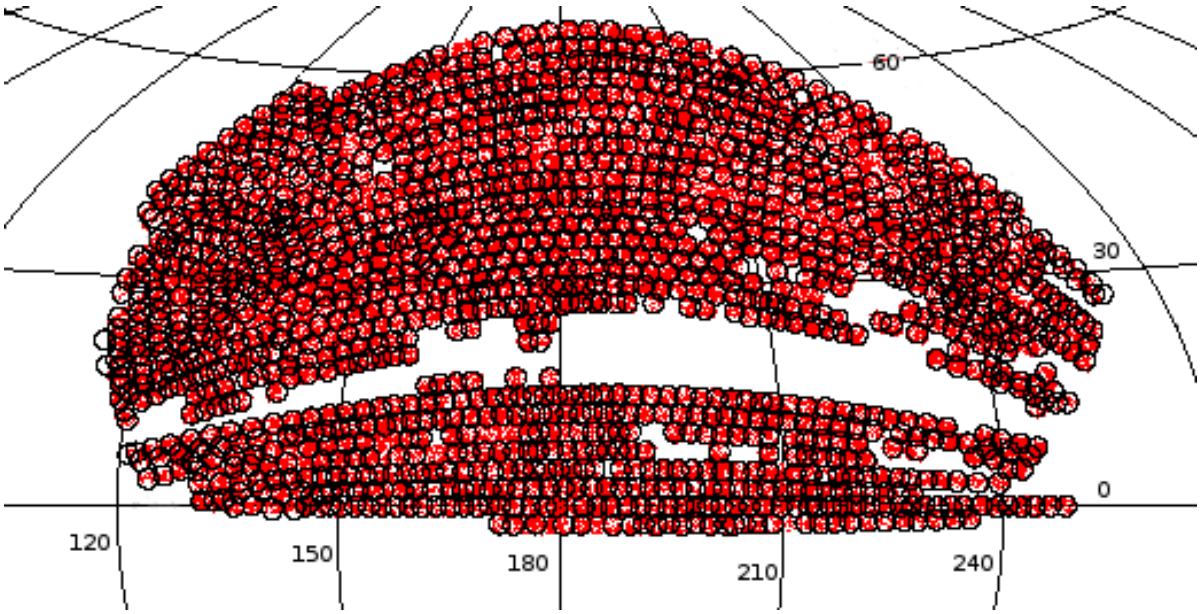

Figure 10.68: SDSS DR6 survey with our selection of LRG galaxies as red points and the spectroscopic "good" plates as black circles

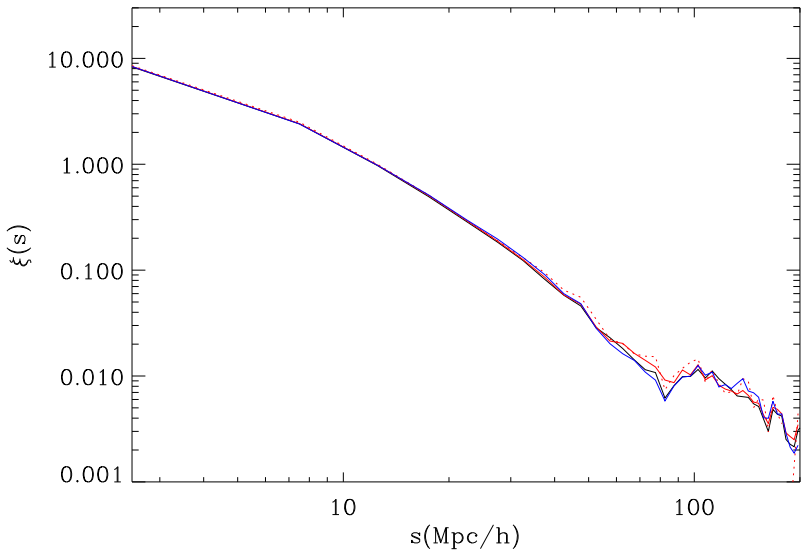

Figure 10.69: Redshift-space correlation function for our mask (black), maskplate1 as indicated in the text (red), maskplate2 (dotted red) and north stripe (blue)

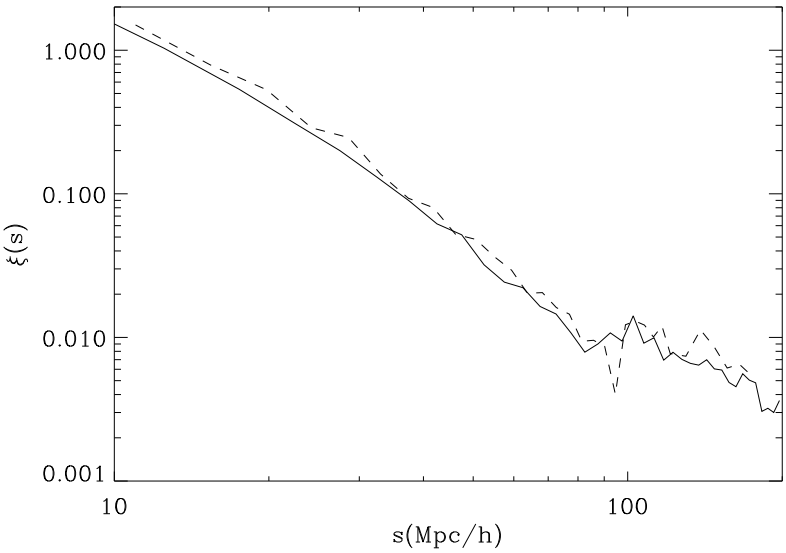

Figure 10.70: Redshift-space correlation function for a volume limited slice selection of LRG galaxies with z=[0.15,0.38] and M_r=[-22.5,-21.5]. Solid line shows the result when using a random catalog. Dotted line shows a new method based on pixelization which validated the previous results

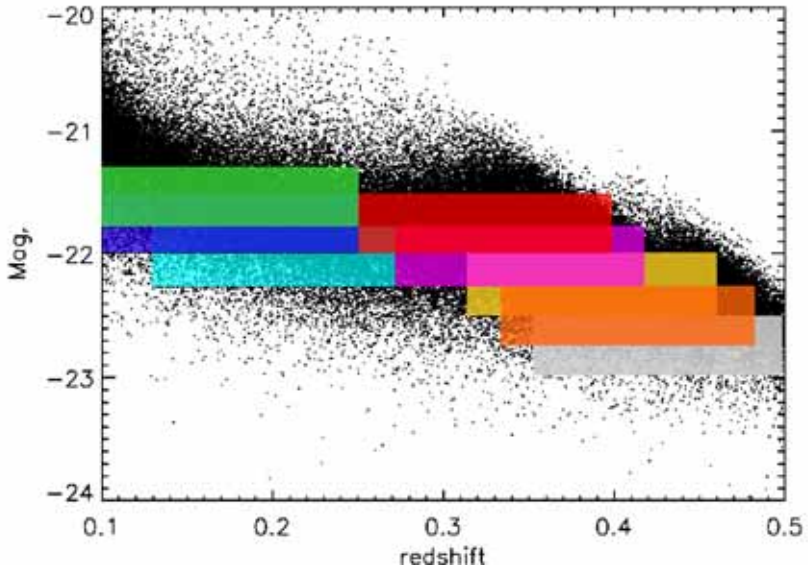

Figure 10.71: We have divided the catalog in different approximately volume limited slices as indicated in table 10.11. Here we over-plot the slices in the plane $M_r - z$

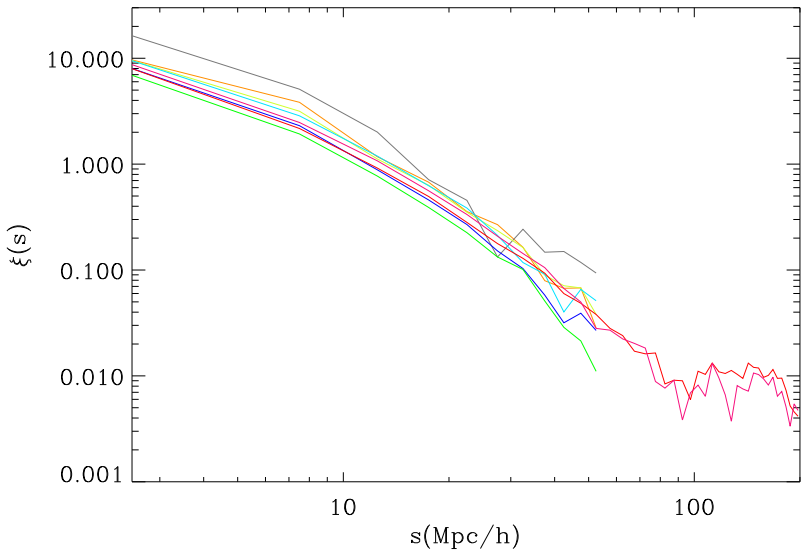

Figure 10.72: Redshift-space correlation function for the different slices plotted in Fig.10.71

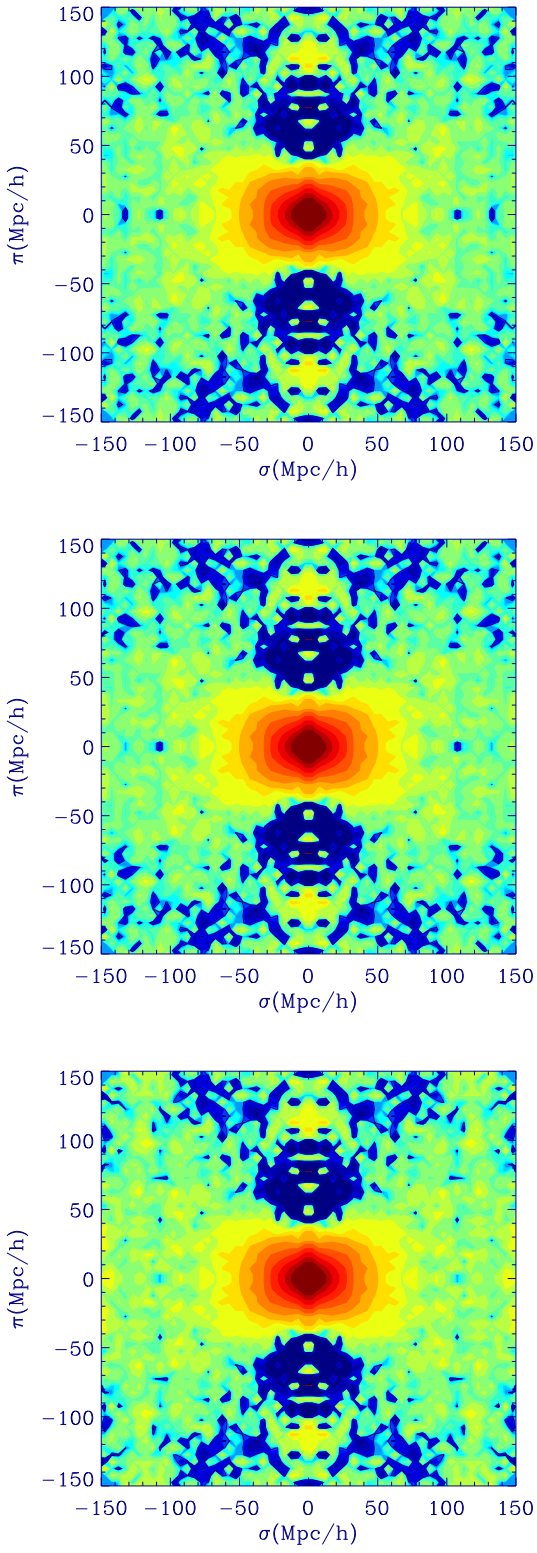

Figure 10.73: Redshift-space correlation function $\xi(\pi, \sigma)$ including all the galaxy pairs (top panel), limiting the angle between galaxies to $\theta < 15deg$ (middle panel) and $\theta < 10deg$ (bottom panel)

Chapter 11

Conclusions for Part II

a) We have shown with realistic simulations that the normalized quadrupole Q(s) provides an estimation for the distortion parameter β, and the effective dispersion of pairwise velocities σ_v, at large real scales ($>$ 1 Mpc/h) and that this measurement is fairly independent of other parameters, such as matter density, amplitude or biasing.

b) We show that one can only recuperate the exact real space correlation function for $r < 30Mpc/h$ through the integration of the redshift distortions along the line-of-sight direction, with actual data. At scales larger than about 30 Mpc/h the recovered correlation is systematically biased. The amplitude of the bias increases with scale and is close to a factor of 2 on BAO scales.

c) We have found an analytical approximation for the error at $\xi(\pi, \sigma)$ (see §9.4.1), ideal for large perpendicular σ. This approximation have been tested and calibrated with a set of very large numerical simulations. The JK error is shown to work well only for small $\sigma < 20Mpc/h$. For larger σ, JK overestimates the true error.

d) We have proved with realistic simulated mocks (with the selection function of LRG, an area 1/8 of the sky and 60 JK zones) that JK works well at all the scales for: $Q(s)$, monopole $\xi_0(s)$, projected correlation function $\Xi(\sigma)$ and real space correlation function $\xi(r)$ (see §8). We also test in detailed in §9.7 the range of validity of the tools and analysis that we will apply to real galaxy samples.

e) Peculiar velocities at large scales are traced by the interaction halo-halo. If we look at the peculiar velocities in halos, we have approximately the same peculiar velocities. For small scales, the dispersion of pairwise velocities σ_v changes with scale (see §9.6).

f) In §10 we study the new SDSS DR6 LRG galaxy sample to find similar conclusions than in previous results with smaller samples.

g) In §10.5, we use the measured quadrupole $Q(s)$ to estimate the redshift distortion parameter β.

h) In §10.6 we estimate Ω_m-Amp for large scales (linear regime) in $\xi(\pi, \sigma)$, where Amp=$b(z)\sigma_8$, as tested with simulations.

i) We have an estimation of σ_8 due to redshift distortions, that allows us to break the degeneracy between bias and σ_8 in the real-space correlation function. We find $\sigma_8 = 0.8 - 0.9$. We also measure the bias as a function of redshift.

j) We have also presented new constraints on the growth index of perturbations γ (which indicates modified gravity) through the redshift distortions.

k) We obtain a power law form for the non-linear bias at small scales, which is in concordance with previous results.

l) In §10.7.1 we recover the pairwise velocity dispersion σ_v as a function of scale at small scales through the distorted monopole. This method is shown to work in realistic simulations.

m) We show in §10.7.2 that a simple Kaiser model convolved with exponential distribution of pairwise velocities, can explain the complicate shape of $\xi(\pi, \sigma)$ at small scales, once we add the scale dependent bias and the scale dependent σ_v (constant along the line-of-sight).

n) When comparing redshift slices, we see that all them have similar distortion parameters β, consistent values of Ω_m and similar $D(z)b(z)$ as in the stable clustering.

o) We cross-correlate LRG with CMB to study the ISW effect again with spectroscopic samples. We find a high signal that can be explained by a combination of a high σ_8 and maybe a high γ, although $1 - 2\sigma$ errors are compatible with the standard model.

p) The baryon acoustic peak helps to constrain the dark energy equation of state parameter w, which is more difficult to obtain from redshift distortions or ISW. We use the position of the BAO in the direction LOS, where it is enhanced by magnification bias, to obtain constraints for $H(z)$. The values are compatible with WMAP5 results, but we find better errors for $H(z)$, which show a tendency to higher value for w which shows some evidence for an increase with cosmic time. We have shown that the anisotropy of the peak in redshift distortions provides a good opportunity to obtain tight constraints on Ω_m and w.